HYDRONAUTICS, incorporated research in hydrodynamics

Research, consulting, and advanced engineering in the fields of NAVAL and INDUSTRIAL HYRODYNAMICS. Offices and Laboratory in the Washington, D. C., area: Pindell School Road, Howard County, Laurel, Md.

HYDRONAUTICS, Incorporated

TECHNICAL REPORT 703-4

AN INVESTIGATION OF TANDEM ROW HIGH HEAD PUMP INDUCERS

Interim Report (Phase I)

By

D. N. Contractor
and
R. J. Etter

May 1969

Prepared Under

National Aeronautics and Space Administration
George C. Marshall Space Flight Center
Huntsville, Alabama
Contract No. NAS 8-20625

TABLE OF CONTENTS

Page

LIST OF FIGURES

Figure 43 - System to Measure Pressure Fluctuations. (Natural Frequency of System > 10 kcps)

Figure 44 - Unsteady Pressure Fluctuations for Stage 1, Inducer No. 2 (3 Blades at 63.5° Pitch) at Two Values of Suction Specific Speed
(a) N_{ss} = 13,900, $\ell/c \approx 1.0$
(b) N_{ss} = 21,000, $\ell/c \approx 1.5$

Figure 45 - Effect of Suction Specific Speed on Total Pressure Fluctuation Level For Isolated and Tandem Inducer Tests

LIST OF TABLES

cps	cycles per second
dB	decibel
g	acceleration due to gravity
k	thermal conductivity, speed of distortion propagation, coefficient in cavity length analysis
ℓ	cavity length
ℓ/c	cavity length/chord ratio
log	base 10 logarithm
m	exponent
mv	millivolt
n	rotational speed; rpm; exponent
p	pressure
psi	pounds per square inch
r	radius
rpm	revolutions per minute
t	spacing of foils in cascade
w	velocity
x	cascade axis parallel to U_o
y	cascade axis normal to U_o
z	axial coordinate
α	angle of attack
β	flow angle
Δ	change in ...
η	efficiency
θ	tangential coordinate
ξ	non-dimensional axial distance
π	3.14159

NOTATION

C_L	lift coefficient
C_s	specific heat
C_θ	non-dimensional tangential velocity = $\frac{V_u r_t}{\Gamma}$
D	diameter, diffusion factor
H	head
H_2	hydrogen
K	coefficient
L	Lift, heat required for vaporization
Lox	liquid oxygen
M	loading parameter = $\frac{1}{2} \Delta w_1 / \beta_1$
N	turning parameter = $\Delta \tan \beta_1 / \Delta \tan \beta_2$
N_s	specific speed = $n\sqrt{Q}/H^{3/4}$
N_{ss}	suction specific speed = $n\sqrt{Q}/NPSH^{3/4}$
NPSH	net positive suction head
Q	discharge, gpm
SPL	sound pressure level (dB)
U	velocity
V	velocity
V_u	swirl velocity
W	velocity
c	chord length
c/t	solidity of a cascade
cm	centimeter

ρ	density, stress, leading edge radius
σ	cavitation number
φ	flow coefficient = V_f/U_t
ψ	head coefficient = gH/U_t^2
ω	rotational speed, head loss coefficient
Γ	circulation

Subscripts

o	based on station 0, reference, ambient
1	based on station 1, upstream
2	based on station 2, downstream
e	effective
f	axial direction
h	hub
i	inlet
ℓ	local
L	liquid, lift
m	model
p	prototype
s	static
t	tip, trailing edge
v	vapor

ABSTRACT

A theoretical and experimental investigation of tandem row high head pump inducers for rocket fuel pump applications was conducted. Stage I of the tandem set was designed to be supercavitating and used theoretical results for constant pressure cambered supercavitating cascades. The head distribution between stages was determined from a stability analysis predicting the conditions for incipient rotating stall. Stage 2 was designed using a technique which represented the blades of the inducer stage by radial line vortices, calculated the interference streamlines and used NACA thickness and camber distributions. The stages were empirically modified to improve performance. The best first and second stage were combined in tandem and tested at two overlaps. The tandem model produced more than the design head coefficient (.29/.25) at slightly less than the design flow coefficient (.083/.100) and less than the design suction specific speed (22,000/30,000). While not quite reaching the design goals, the experimental performance did indicate that the tandem inducer using a supercavitating first stage has definite potential as a high suction specific speed design concept.

1.0 INTRODUCTION

The inlet operating conditions of a pump including inlet head, rotative speed, and total discharge may be combined to form the parameter, suction specific speed defined by Equation [1]

$$\frac{n\sqrt{Q}}{NPSH^{3/4}} \qquad [1]$$

Although not dimensionless, this parameter, in common use throughout pumping literature, may be shown by dimensional considerations (1) to indicate the combination of inlet operating conditions which will give similar flow and cavitation patterns in machines which are geometrically similar. For a given discharge, high suction specific speed pumps result when either rotational speed is increased or inlet NPSH is decreased. Both changes result in significant system weight reductions when the pumps under consideration are being used as fuel or oxidizer pumps in liquid-fueled rocket engine systems. Figure 1 shows the effect of suction specific speed on total power plant weight for a typical rocket engine. Reductions in the propulsion systems weight can be utilized for higher payload weight which is normally only a small percentage of total vehicle weight. As an example, consider the Saturn V launch vehicle used for manned lunar missions in the NASA Apollo program. The total launch weight of the Saturn V is 6,262,500 pounds with an escape payload of only 100,000 pounds. In this case, a decrease of only 1/2% in total vehicle weight could result in a 30% increase in payload.

The three stage Saturn V uses liquid fuels and oxidizers with lox/hydrocarbon fuel in the first stage and lox/H_2 in the second and third stages. By far the largest physical components of such a system are the propellant tanks whose wall thickness is determined primarily by tank pressure (3). Lower propellant tank pressures allow lower vehicle weight. With higher rotative speeds, the size and weight of the fuel pumps are also reduced and the possible need for speed reduction components between turbines and pumps eliminated.

These weight reductions through the use of lower pressures and higher speeds are not, however, achieved without accompanying technical problems. Forcing the fuel/oxidizer* pumps to operate at high values of suction specific speed results in cavitation of the pump impellers. In ordinary pump experience, an N_{ss} value of 8000 or more results in cavitation causing vibration, noise, impeller damage, and a decrease in discharge and efficiency. The problem of pumping at high N_{ss} has however, been largely alleviated through the use of pre-pumping stages called "inducers" which operate rather satisfactorily even with extensive cavitation. A typical inducer consists of a high solidity, axial flow impeller with a small number of blades. The blade form usually approximates a simple helix. Inducers are generally located immediately upstream of the main fuel pump and operate at the same rpm on the same shaft as the main pump rotor. The problems of low efficiency and cavitation damage to the impeller

* Hereafter referred to only as fuel pumps.

blades are not restrictive in the application of inducers to rocket fuel pumps since the inducer produces only a small percentage of the total head rise of the fuel pump and the operating lifetime of the unit is short enough that little damage can occur. The problem of flow instabilities, however, is very significant as a limiting condition for acceptable inducer operation. Model tests and operating experience (4,5,6,7) have shown that under certain operating conditions the discharge and head rise across an inducer may fluctuate violently resulting in corresponding engine thrust fluctuations contributing to the so-called "Pogo" effect. The unsteady motions and accelerations caused by the thrust fluctuations provide an unacceptable environment for delicate equipment and human pilots.

One method suggested for reducing or eliminating the instabilities and fluctuating output of the inducer is the use of a tandem row inducer whose first stage operates at the design suction specific speed but delivers only a fraction of the total inducer head rise, thus operating with greater stability. The second stage of the inducer consequently operates at a lower suction specific speed and should also deliver the remaining head rise with greater stability. This concept has been used by other investigators (8).

In the present study, the nominal prototype fuel pumps following the inducers are centrifugal and the liquid being pumped is liquid oxygen. The properties of cavitating flows in cryogenic fluids are such that modelling the flows in water is a conservative

procedure, that is flows in liquid oxygen are more likely to be stable than similar flows in water. One factor which contributes to the stability of cryogenic cavity flows is local cooling at the cavity boundary (2). This local cooling results in a liquid film at the vapor cavity with a lower vapor pressure than that of the bulk fluid. Reference 2 presents the following equation for this local vapor pressure drop.

$$\Delta P_v = K \left(\frac{\rho_v}{\rho_L} \frac{L}{C_s} \frac{dp}{dT} \right) \left(\frac{\rho_L C_L}{k} \right)^m U^n \qquad [2]$$

where

K	depends on the hydrodynamics of the flow
$\frac{dp}{dT}$	is the slope of the vapor pressure temperature curve at the bulk liquid temperature of interest
U	= a characteristic velocity
ρ_v and ρ_L	are the vapor and liquid densities
k	= the thermal conductivity of the liquid
L	= heat required for vaporization
C_s	= specific heat of the fluid

The last two terms are heat transfer factors. The exponents m and n are dependent on the heat transfer process accompanying cavitation. Venturi experiments (2) have established the validity of this relationship. The vapor pressure drop for water at ordinary room temperatures is negligible, the drop for most

cryogenic fluids however is significant. If water, however, were superheated to 450°F its local vapor pressure drop would be similar to that of liquid H_2 at -423°F. Lower vapor pressure at the cavity surface means that the local cavitation number of the flow defined as:

$$\sigma_\ell = \frac{P_{s\ell} - P_{v\ell}}{\frac{1}{2}\rho U_\ell^2} \qquad [3]$$

is actually higher than one would calculate based on the bulk fluid vapor pressure. Higher cavitation numbers mean lower N_{ss} values and nominally more stable flows. Tests using helical inducers (2,9) have further verified the fact that flow breakdown in liquid H_2 is much delayed over that of water at similar inlet conditions.

The operating conditions chosen to govern the design and testing of the present tandem row inducer were as follows:

φ_o , flow coefficient = 0.10

ψ , total head coefficient = 0.25

N_{ss}, suction specific speed = 30,000

An innovation of the present tandem row design is the use a supercavitating (29) first stage. The supercavitating stage is one whose blade form is deliberately designed to produce large stable suction side vapor cavities springing from the blade leading edge and collapsing beyond the trailing edge. The

second stage is designed as a high solidity high head axial flow rotor operating with minimum cavitation. The design head rise produced by the first stage is the maximum allowable within the limits of certain stability requirements. A generalized theory for the prediction of instabilities caused by self-induced circumferential distortion or rotating stall (10) was used to determine the maximum stable head rise. The application of this theory required a knowledge of the performance of supercavitating cascades under various inflow conditions. The performance of supercavitating cascades with constant pressure cambered blades and finite cavity lengths was, therefore, studied theoretically. The results have been published in previous reports (11, 12).

The second stage of the tandem row inducer was designed using the theory for axial flow pump design presented in Reference 13. This method accounts for induced interference effects at an impeller blade as influenced by the other blades and the total downstream vorticity along the pump centerline. Optimization of the cavitation performance of the second stage is also accounted for in the procedure.

Details of the theory, design, and testing of the inducers are described in subsequent sections of this report.

2.0 DESIGN OF INDUCER NUMBER 1

2.1 First Stage of Inducer Number 1

2.1.1 Design Criteria

As mentioned previously, the first stage was designed for a flow coefficient of 0.1 and a suction specific speed of 30,000. These values were chosen as being typical values capable of being achieved by current inducer designs. The first stage design head coefficient was determined from the stability of the flow through the impeller. An initial percentage of the total desired head rise was assigned to the first stage and the design and stability analysis computed. If the flow was unstable the head coefficient was decreased in steps until the flow through the first stage impeller was shown to be stable according to the method of Reference 10.

2.1.2 Design Procedure

The procedure used in the design of the supercavitating first stage was the familiar free-vortex, blade element theory described in References 14 and 15. Appendix A presents the most important equations of the theory. This design method allows the design to be based on the performance of two-dimensional supercavitating cascades. The theory for determining the stability of the flow through a blade row (10) also requires a knowledge of the behavior of these cascades. Hence, information regarding supercavitating cascade performance was essential. Experimental data on such cascades is limited and does not cover

a wide enough range of cascade parameters to be useful. It was therefore decided to use theoretical predictions of the performance of supercavitating cascades for the design. Since the stability of the flow through the impeller was a controlling factor in the design, supercavitating cascades of flat plate foils were not used. Flat plate foils develop all of their lift from angle of attack and are thus more likely to develop unstable flow conditions. Cambered foils develop a portion of the total lift through camber and have higher lift-drag ratios. They are, therefore, likely to develop more stable flows than flat plate foils with the same loading. A theoretical study of the performance of supercavitating cascades with constant pressure cambered blades was undertaken. The results of this study are presented in References 11 and 12 and are summarized in the following section.

2.1.3 Performance of Constant Pressure Cambered Supercavitating Cascades

The performance of constant pressure cambered supercavitating cascades was obtained for a wide range of cascade parameters. Figure 2a presents a definition sketch of a typical supercavitating cascade. Figure 2b relates the cascade parameters to the velocity triangles for a tandem inducer. The cascade parameters that varied were the stagger angle, solidity, cavity length to chord ratio and leading edge radius of the foils. The performance of each cascade was obtained in terms of the lift and drag coefficients, of an individual foil in cascade, the exit flow angle and the operating cavitation number.

In addition, the shape of the lower surface of the foil and the cavity shape were calculated. From the numerical results obtained, the following general remarks can be made regarding the performance of these supercavitating cascades.

The performance of typical cascades is shown in Figures 3 and 4. It can be seen that as the cavity length to chord ratio (ℓ/c) increases the drag coefficient increases slowly for low solidities and sharply for the higher solidities. Hence, it can be surmised that supercavitating impellers with high solidities will have a narrow range of operating cavitation number and are likely to become unstable at the lower cavitation numbers. Experimental tests on single foils have shown that the cavity becomes unsteady as the (ℓ/c) ratio approaches unity. Long cavities are not desirable because of the higher drags associated with them and the possibility of the cavity from the first inducer stage interfering with the performance of the second. It appeared that a favorable compromise value of the ℓ/c ratio for design purposes was approximately 1.50.

It can be seen by comparing Figures 3 and 4 that as the stagger angle increases lower values of σ/C_L can be used for a given solidity and ℓ/c ratio. This fact implies that impellers capable of operating at lower cavitation numbers can be designed with higher stagger angles.

To facilitate the design of supercavitating impellers, the cascade performance was plotted in the form shown in Figure 5. The value of $\frac{C_L}{\sigma}\frac{c}{t}$ could be calculated from Equation [A-1] of

Appendix A for given inducer operating conditions. The solidity required for a given cavity length to chord ratio and leading edge radius could then be obtained from graphs similar to Figure 5. It can be seen from this figure, that larger values of $\frac{C_L}{\sigma}\frac{c}{t}$ are obtained by using higher solidities. However, the higher solidities also have higher drag coefficients and the acceptable upper limit for solidity has to be determined from stability considerations.

The effect of leading edge radius on the performance of constant pressure cambered supercavitating cascades is shown in Figure 6. The larger the leading edge radius, the larger the drag for a given σ/C_L and hence the larger the solidity required for a given $\frac{C_L}{\sigma}\frac{c}{t}$. The use of zero leading edge radius would entail very high structural stresses near the blade leading edge with consequent leading edge flutter or structural failure. Hence some finite leading edge radius has to be used to keep the stress below the acceptable design stress for the blade material.

An important characteristic of constant pressure cambered supercavitating cascades should be noted. The actual camber of these foils is a function of C_L, c/t, stagger angle, etc. The camber is not strongly dependent on either cavity length or cavitation number for uniform pressure distribution on the foil and the camber decreases as the solidity increases for a given angle of attack. Hence for high solidity the lift coefficient of constant pressure foils is nearly as low as that of flat

plates. Figure 7 compares the performance of constant pressure cambered foils and flat plate foils in cascade. It can be seen that the most efficient use of constant pressure cambered foils can be made only at low solidities.

Thus we are faced with conflicting requirements. On one hand, high solidities for high lift parameter values $\left(\frac{C_L}{\sigma}\frac{c}{t}\right)$ and on the other, low solidities for high lift-drag ratios.

2.1.4 Stability Analysis

There are numerous possible sources of the observed instabilities in cavitating inducers. Among the primary possibilities are: (1) unstable interaction of tip cavities with adjacent blades, (2) unsteady location of the cavity separation point near the leading edge of the blade, (3) interaction of the inducer with the hydrodynamic and hydro-elastic properties of the load, (4) leading edge flutter, and (5) travelling circumferential distortion or rotating stall. Some detailed discussion of these is given in Reference 30. Of these causes, the last was selected as the most significant and the one most amenable to analytic study. Rotating stall in axial-flow compressor operation occurs at low flows and consequent high angles of flow incidence. This phenomenon has been studied experimentally and analytically by several investigators and has been summarized in Reference 16. A brief description is as follows. As blade rows approach stall, the flow separates in some groups of blades. The stalled blade restricts the flow through the channel adjacent to its upper surface and in consequence the fluid is deflected

around the blocked channel, increasing the angle of incidence on the blade above and decreasing the angle of incidence on the blade below so that these patterns of stalled and unstalled flow do not remain fixed but are propagated along the cascade. The result is that the blade rows are subjected to violent periodic dynamic loads, since they find themselves alternately in stalled and unstalled flow.

Various theories concerning the problem of rotating stall have been proposed, the majority of which use a small perturbation approach, and therefore, apply strictly only to an incipient stall which is identified as a self-induced distortion. The most recent and lucid analysis seems to be that due to Yeh (3) who treated the problem on the basis of classical actuator disc theory. It was found by Yeh that, in general, both a traveling circumferential distortion and a spanwise type self-induced distortion are possible. It has been further shown that the purely traveling circumferential type would in all probability occur first. Restricting the analysis to this type simplifies the problem enormously. The conditions required for the purely circumferential type self-induced distortion to occur are shown to be

$$M = [1 + \tan^2\beta_2 + N(1 - \tan\beta_1 \tan\beta_2)]/\tan\beta_1 \qquad [4]$$

$$k = [1 + \tan^2\beta_2 + N(1 + \tan^2\beta_1)]/(2\tan\beta_1) \qquad [5]$$

where:

M is defined as $\frac{1}{2}\frac{\Delta\omega_1}{\Delta\beta_1}$

N is defined as $\frac{\Delta \tan\beta_2}{\Delta \tan\beta_1}$

β_1, β_2 are the relative flow angles, upstream and downstream of cascade

k is the ratio of the speed of distortion propagation to the axial component of inlet velocity

ω_1 is the head loss coefficient $\frac{2gH_L}{U_o^2}$

In order to find the cascade geometry which meets the design conditions and is also best able to delay the onset of rotating stall, one must consider two problems:

(a) how to increase the value of M necessary for distortion propagation, M_{limit}

(b) how to decrease the actual operating value of M, $M_{cascade}$.

Several interesting results were deduced by Yeh concerning Equation [4]. It can be seen that if $(\tan\beta_1 \tan\beta_2) > 1$, higher values of N, that is, lower solidities, will decrease M_{limit} and thus promote rotating stall. The product $(\tan\beta_1 \tan\beta_2)$ is >> 1 in the present case and, hence, under these conditions, increasing the solidity will promote stability.

Equation [4] can be applied directly to the stability of a supercavitating impeller. All of the parameters in the equation can be obtained from the results of Reference 4 and the values of M and N obtained graphically. This procedure was applied to the design of the first stage. If the design was shown to be unstable, the design parameters were adjusted and the stability procedure repeated until a stable impeller design was obtained. The design parameters that could be modified in the interest of stability were the percentage of total head assigned to the first stage (first stage head coefficient), the design cavity length to chord ratio, the leading edge radius and the hub radius to tip radius ratio. The effect of each of these parameters on stability is discussed below. In all cases, the product of $\tan \beta_1$ and $\tan \beta_2$ was found to be greater than unity and hence the smaller the value of N, the larger was M_{limit}.

(a) Effect of Head Coefficient.

Figure 5 shows that large values of $\frac{C_L}{\sigma} \frac{c}{t}$ can be obtained by using high stagger angles and high solidities. However, this can be a practical design region only if stable flow exists under those conditions. Thus, the maximum allowable head coefficient will be stability-controlled. The higher the head coefficient, the larger the lift and drag coefficients and hence the larger the value of $M_{cascade}$. As the solidity increases, the value of N is reduced, consequently increasing M_{limit}. However, the increase in $M_{cascade}$ is much steeper than the increase in M_{limit} and at some value of head coefficient, ψ, the flow through the impeller will become unstable.

(b) Effect of Cavity Length

In the design of a supercavitating first stage for a given head coefficient, it was necessary to determine the optimum cavity length to chord ratio. The longer the cavity, the lower is the solidity required for a given $\frac{C_L}{\sigma}\frac{c}{t}$. Lower solidities increase N and consequently decrease M_{limit}. Large cavity length to chord ratios also result in large drag coefficients and hence large values of $M_{cascade}$. Thus, it appears that the shorter the cavity length, the more likely the design will be stable based on the Yeh criterion alone. The inherent stability of cavity flows, however, must also be considered.

(c) Effect of Leading Edge Radius.

From Figure 6, it can be seen that the larger the leading edge radius, the larger is the required solidity for a given $\frac{C_L}{\sigma}\frac{c}{t}$. This makes N small and M_{limit} large. However, the drag coefficient increases rapidly with leading edge radius and this causes a rapid increase in $M_{cascade}$. Hence, in general, it can be stated that increasing the leading edge radius tends to make the inducer unstable. A conservative procedure is to work with curves calculated for a leading edge radius slightly larger than the anticipated leading edge radius.

(d) Effect of Hub-Tip Radius Ratio.

For a given tip radius, an increase in the hub radius results in a higher local flow coefficient and lower stagger angle. From Figure 5 it can be seen that a fixed $\frac{C_L}{\sigma}\frac{c}{t}$ can be

obtained at smaller stagger angles by using higher solidities and higher values of α/C_L. Higher solidity is beneficial for stability; however, higher drag coefficients decrease the stability margin. No general statement can, therefore, be made as to the effect of hub-tip radius ratio changes and each case must be studied individually.

2.1.5 Results of Design Procedure

It has been previously explained that the maximum allowable design head coefficient for the supercavitating first stage is determined by stability requirements. At first, the supercavitating impeller was designed to produce 0.25 of the total inducer head coefficient. However, when Yeh's stability criterion was applied to this design, it was found that the flow through the impeller would be unstable. A second design was produced in which the first stage head coefficient was 0.20 of the total inducer head coefficient. Once again, Yeh's stability analysis showed that the flow through the impeller would be unstable. A third design was initiated with a design head coefficient 0.15 of the total inducer head coefficient. For this value of 0.15, the stability analysis showed that the impeller was stable. The results of the final design and stability analysis are presented in Appendix A. Figure 8 shows a photograph of the first stage model.

An analysis of the stresses in the first stage was made to insure the structural adequacy of a full scale impeller that might be used in future rocket fuel pump designs. The working

stress used in the design of the first stage was determined in the following manner.

It was assumed that prototype impellers would be made from the Titanium alloy Ti-Al6-V4 with high yield strength and anti-corrosion properties. This alloy at room temperature has a yield strength (0.2% offset) of 120,000 psi. The fatigue limit of the material for 10^7 cycles, with a load factor of 0.6 is equal to 103,000 psi. Assuming a factor of safety = 2, the working stress in the prototype was taken as 51,500 psi. The working stress in the model was obtained by the use of the fo lowing relationship:

$$\frac{\text{Model Stress}}{\text{Prototype Stress}} = \frac{\rho_m}{\rho_p}\left(\frac{\eta_m}{\eta_p}\right)^2\left(\frac{D_m}{D_p}\right)^2 = K \qquad [6]$$

By comparing existing prototype designs with the first stage of the tandem row inducer, values of K from 0.2 - 0.4 were obtained. Thus, a model working stress of 0.2 x 51,500 = 10,300 psi was selected. The maximum stress in the hub section due to combined bending, centrifugal forces and shear was below 6000 psi. However, because of the thin leading edges in supercavitating blade sections, the chordwise bending stresses at the tip were higher than the stresses at the hub. The leading edge radius of the supercavitating sections was selected such that the leading edge stresses would be about 10,000 psi. The design of the first stage was thus considered to be structurally compatible with typical full scale impellers.

2.2 Second Stage of Inducer Number 1

2.2.1 Design Criteria

In the design of a tandem row inducer, the second stage has to be matched to the flow conditions downstream of the first stage. Since the first stage was designed to develop 15% of the total inducer head, the second stage must be designed for the remaining 85% of the total head. The second stage also operates at a much lower suction specific speed than the first stage. The second stage pitch also must take into account the swirl behind the first stage. For continuity the flow coefficient for both stages is the same since the hub to tip diameter ratio does not change.

2.2.2 Design Procedure

The design procedure used for the first stage could not be used for the second stage since the performance of two-dimensional, high solidity, high stagger angle cascades is not known. It became necessary therefore, to adopt a method by which impellers could be designed without the use of experimental or theoretical cascade data. One such method was presented by Bowerman (6) as an improvement over the design method which uses two-dimensional cascade theories. Bowerman has verified his design method experimentally for an impeller with a specific speed of 10,000. However, the limitations of the method are not known, especially in the realm of low specific speeds, where the solidity must become high.

The design method consists of representing the impeller blades by a number of radial line vortices. One blade (vortex) is removed from the impeller and the interference streamline due to all the other blades and the total downstream vorticity is calculated. The camber and thickness distributions are then superimposed on the interference streamline, resulting in the final impeller design. The constants used in the calculation of the interference streamline are presented in Reference 6 for one particular blade angle. Since the blade angles encountered in the design of the second stage were different from those used in Reference 13, these constants were evaluated according to the method suggested in Reference 13. Use was made of the results of Reference 17, in which the distribution of tangential, axial and radial velocities due to a single radial line vortex in an annular space are given. The tangential component of velocity V_u due to all of the other blades is non-dimensionalized as follows:

$$C_\theta = \frac{V_u \, r_t}{\Gamma} \qquad [7]$$

It was found, as in Reference 6, that C_θ varied almost linearly with non-dimensional axial distance $\xi = z/r_t$. Thus,

$$C_\theta \approx K_o + K_1 \frac{\xi}{\xi_t} \qquad [8]$$

where ξ_t is the value of ξ at the trailing edge of the foil.

The values of K_o and K_1 for the three different radii are presented below.

Radius/Tip Radius	K_o	K_1
1.0	0.0112	0.1368
0.8	0.007	0.185
0.6	0.017	0.232

The formulae given in Reference 13 enable the streamline equation to be derived when C_θ is given. These formulae were modified slightly to take into account the initial swirl from the first stage of the inducer. The equations for the streamlines at three different radii are given below.

At $r/r_t = 1.0$ $\quad \theta = 1.735\ z - 0.0955\ z^3$

$r/r_t = 0.8$ $\quad \theta = 1.708\ z - 0.161\ z^3$

$r/r_t = 0.6$ $\quad \theta = 1.592\ z - 0.27\ z^3$

The details of the design calculations are presented in Appendix B and a photograph of the second stage is shown in Figure 8. A camber line of the NACA 67 series was chosen so that the pressure distribution would be such that possible blade cavitation would be minimized. A thickness distribution of the NACA 16 series was used. These distributions were used along with the aforementioned design procedure to determine the final coordinates of the foil.

Theoretical pressure distributions were obtained for the sections at the tip, mid-radius and the hub by superimposing the pressure distributions due to the camber and thickness of the foil on the mean pressure rise in the pump. The pressure distributions for NACA 67 series mean camber line and NACA 16 series thickness distributions were obtained from Reference 18. The mean pressure rise in the pump was evaluated using the induced tangential velocity along the chord obtained previously for calculating the interference streamline. The final pressure distribution for the section at the tip radius is shown in Figure 10. The cavitation number σ of the approaching flow is also shown in Figure 10 and it can be seen that the minimum pressure coefficient is greater than $(-\sigma)$. Thus, the impeller was expected to be cavitation-free at design conditions.

The stresses in the blade at the hub section were low since the section modulus of the foil at the hub was large. The stresses near the leading and trailing edges of the foil at the tip section were also calculated and were found to be less than the selected working stress of 10,000 psi.

3.0 TEST FACILITY AND PROCEDURE

3.1 HYDRONAUTICS', Incorporated Variable Pressure Pump Loop

3.1.1 Description and Capabilities

HYDRONAUTICS, Incorporated has designed and fabricated a pump test loop capable of testing the performance of a variety of pumps over a wide range of operating conditions. The plexiglas test section of the loop is 22 inches long with an internal diameter of 7 inches. Plexiglas was used to make observations of the onset and extent of cavitation possible. Figure 11(a) shows the test section with the first stage of the tandem row inducer operating in it. The cloudy region is caused by cavitation.

The entire pump loop can be pressurized to 200 psi to eliminate cavitation or the pressure can be reduced to very low absolute values to simulate low cavitation numbers. Thus, pumps can be tested at suction specific speeds as high as 30,000. A continuously variable speed 150 hp drive provides a shaft speed up to 5000 rpm. A torque and thrust dynamometer located on the shaft downstream of the test section enables these quantities to be accurately measured. A specially designed valve located downstream of the test section allows flow regulation. A heat exchanger allows the water temperature to be kept steady even though considerable heat may be generated by the dissipation of energy in the water. Figure 11(b) shows overall photographs of the pump loop and associated instrumentation.

3.1.2 Instrumentation

The pump loop is equipped with instrumentation to measure static and total pressures and velocities in the test section. Three probes of the type shown in Figure 12 were inserted through the test section wall for radial surveys of pressures, velocities and flow angularity. These probes were calibrated in the High Speed Channel at HYDRONAUTICS, Incorporated for cavitation effects and for the effect of boundary proximity. The probes can be located at several points in the test section. Because of the large number of pressures that had to be measured for each test run, a "Scanivalve" was used. This device allows the pressures to be connected in succession to one of two pressure transducers. One transducer was used for low pressures (0 - 10 psi) and the other for high pressures (0 - 100 psi). Arrangements are provided to effectively bleed the tubing of air, which could be a major source of error especially at low absolute pressures.

The pressure transducers used are of the differential reluctance type and their output is displayed digitally. The transducers were calibrated and the output was found to vary linearly with pressure. The shaft rpm is measured by means of a calibrated strobe light, which is also essential for observation of the type and extent of cavitation occurring on the blades.

3.2 Test Procedure

The test procedure adopted for all impellers was the same as that used for cavitation tests on a conventional pump. The flow coefficient was held constant and the net positive suction

head (NPSH) of the pump lowered until the total head decreased rapidly due to cavitation. All tests were conducted at a shaft speed of 4000 rpm. The pressure upstream of the impeller was first reduced to the required value. The valve downstream of the pump was then regulated until the required flow coefficient was obtained. Measurements of the static and total pressures and flow angularity were made at 5 or 6 radial positions upstream and downstream of the impeller. These data were processed by an IBM 1130 computer which integrated the pressures and velocities and calculated the total flow and the total head rise. The computer program also calculated the overall efficiency, dimensionless coefficients and the radial variation of lift and drag coefficients.

4.0 RELATIONSHIP BETWEEN SUCTION SPECIFIC SPEED AND CAVITATION NUMBER

Since cavitating cascade performance, either experimental or theoretical, is presented in terms of the cavitation number while cavitating pump performance is presented in the common parameter of suction specific speed, a discussion of the relationship between these two parameters is appropriate.

The cavitation number is related to suction specific speed in the following manner. Assuming an axial flow machine with no prerotation, the inlet cavitation number will vary in the radial direction. For purposes of comparison, the tip cavitation number will be used since it represents the lowest value of any radial location. The tip cavitation number is defined as:

$$\sigma_T = \frac{H_{static} - H_{vapor}}{w_1^2/2g} \qquad [8]$$

where

$$w_1 = \sqrt{U_T^2 + V_f^2}, \quad U_T = \frac{2\pi n}{60} r_t$$

w_1 is the velocity of flow relative to the impeller blade.

Suction specific speed is not dimensionless and is defined as:

$$N_{ss} = \frac{n\sqrt{Q}}{NPSH^{\frac{3}{4}}} \qquad [9]$$

where

$$NPSH = H_{static} + \frac{V_f^2}{2g} - H_{vapor}$$

Combining these two relationships and further using the definition of flow coefficient,

$$\phi_o = \frac{V_{f_o}}{U_T} \qquad [10]$$

one may obtain the following relationship between σ_T and N_{ss} for an axial flow machine with a 60 percent hub.

$$N_{ss} = \sqrt{\phi_o} \left[\frac{67272}{.41 + \phi_o^2} \Big/ \sigma + \frac{\phi_o^2}{.41 + \phi_o^2} \right]^{\frac{3}{4}} \qquad [11]$$

For other hub-diameter ratios, the constants in the above equation will change. Figure 13 shows the solution of Equation [11] for a variety of tip cavitation numbers and flow coefficients. Two characteristics of this relationship should be noted. First, there exists an optimum flow coefficient for which a maximum value of N_{ss} can be obtained for each tip cavitation number. Secondly, for each flow coefficient there exists a theoretical maximum possible suction specific speed which occurs when the tip cavitation number (i.e. inlet static pressure) is zero. This maximum possible N_{ss} is strongly dependent on ϕ_o. The purpose in introducing these relationships is to clarify the operating regime of the inducers presently being discussed. All of the data presented in this report will use suction specific speed rather than cavitation number as the parameter describing cavitating operating conditions.

5.0 RESULTS OF TESTS ON INDUCER NO.

5.1 First Stage Test Results

5.1.1 Blades at Design Pitch

The first stage of inducer No. 1 was tested at its design pitch at flow coefficients of 0.101, 0.080 and 0.064. The results of these cavitation tests are presented in Figures 14a, 14b and 14c. It can be seen from Figure 14a that complete head breakdown occurred at a suction specific speed of 22,000 - 23,000. The tests could not be conducted at flow coefficients less than 0.06 because of cavity instabilities that developed under those conditions. At flow coefficients greater than 0.1, face cavitation developed with consequent poor head generation. Figure 14b indicates the cavity length to chord ratios observed during the tests and Figure 14c shows the variation of the efficiency of the impeller. The impeller was unable to operate at the design suction specific speed, (30,000) longer cavity length to chord ratios were obtained than the design value of 1.5, and the measured efficiencies were lower than the design value (≈65 percent).

When operating at a flow coefficient ϕ of 0.1, some face cavitation was observed at the leading edge of the blades. At $\phi = 0.08$, the face cavitation was reduced substantially and at $\phi = 0.064$ it disappeared completely. Because of this it was deduced that altering the pitch of the blades would improve cavitation performance by more nearly approaching shock free entry at a flow coefficient of 0.10. The hub of the first stage was modified so that the pitch could be changed to 1°, 2° and 4° less than the design value. The results of these tests are described below.

5.1.2 Blades 1°, 2° and 4° Less than Design Pitch

The results of tests on the impeller with blades set 1°, 2° and 4° less than design pitch are presented in Figures 15, 16 and 17 respectively. A comparison of the performance of the impeller at design flow coefficient and various pitch settings is presented in Figure 18. The pitch setting 2° less than design appears to perform best at low cavitation numbers. At higher cavitation numbers, there was little difference in performance among the three modified pitch settings. Although somewhat improved, the performance at the new pitch settings did not approach the desired design performance. Cavity lengths and efficiencies at the new pitches were nearly identical to those at design pitch and were therefore not presented.

5.2 Second Stage Test Results, Inducer No. 1

The second stage was initially tested in the pump loop without the first stage. Results of these tests are tabulated below:

TABLE 1

Performance of 2nd Stage of Inducer No. 1

Pitch = 65.8°

	Design Conditions	Test Run No. 1	Test Run No. 2	Test Run No. 3
Flow Coef. ϕ	0.100	0.0510	0.0443	0.0370
Head Coef. ψ	0.2125	0.0485	0.250	0.278
Efficiency, η	0.85	0.12	0.62	0.73
Suction Spec. Speed N_{ss}	13,250	5,300	5,800	9,000
$2g(NPSH)/U_T^2$	0.113	0.245 see Note 1	0.196	0.0971 see Note 2

Note 1: Extensive Face Cavitation - Choked Flow.

Note 2: Separation Occurs at the hub section with resulting increased flow at the tip section.

In these tests, head coefficients higher than the design value were developed. This indicated that the solidity of the blades was more than adequate. However, the flow coefficient, at which these high heads were developed, was much lower than the design value.

6.0 ANALYSIS OF PERFORMANCE OF INDUCER NO. 1

6.1 First Stage, Inducer Number 1

An analysis was made to determine the reason for the discrepancy between the design and test performance of the first stage. The assumptions necessary for the application of two-dimensional theory to the design of axial-flow pumps appeared to be satisfied. Thus, the total head generated by the impeller was constant along the radius, indicating a free-vortex pattern of flow. The axial component of the velocity ahead and behind the impeller was nearly constant along the radius, indicating that the flow streamlines occurred on co-axial cylinders. Figure 19 shows the radial distribution of total head and axial velocity measured during a typical test of the first stage of inducer no. 1. The cavity length to chord ratio was also reasonably constant with radius as was assumed in the design. It was thus concluded that three-dimensional deviations from the two dimensional theory used for the design were not responsible for the discrepancy.

The results of the theoretical performance of constant pressure cambered supercavitating cascades were re-examined. In checking the numerical results of the theory of Reference 11, a small source of error in the numerical procedure was detected and corrected. Another source of error lay in the fact that the performance of foils with zero leading edge radius were used in the design of the impeller. However, the actual impeller had a leading edge radius of about 0.005 inches or $\rho/cC_L = .0087$ at

the characteristic radius. The total effect of the above corrections could account for only a portion of the total discrepancy between the theory and experiment.

Despite the poor performance of the first stage at design pitch, it was anticipated that appropriate changes in the blade pitch could improve the cavitation performance of the impeller. Such changes are standard procedure in regular turbomachine practice and form the foundation of controllable pitch, axial-flow runners. Normally, when the blade pitch of an axial flow turbomachine is changed and the flow conditions are kept constant, the angle of attack at each flow condition is changed by the amount of the pitch change. However, the present experiments showed that as the blade pitch changed, slight prerotation of the flow ahead of and in the direction of rotation of the impeller took place decreasing the effect of angle of attack increase. The mechanisms responsible for the prerotation are probably back flow at the tip radius evidenced by occasional flashing of the tip cavity upstream of the impeller and hub friction, since the hub extends upstream of stage 1. As shown in Figure 18, the 63.5° pitch was clearly more than the optimum while 59.4° was clearly less than the optimum leading to earlier cavitation breakdown. For the present design, 62.5° is probably near the optimum pitch angle for $\Phi_{o} = .10$.

In order to further understand why the original supercavitating first stage did not produce the predicted head coefficient at the design suction conditions, an analysis of the measured data at three pitch angles was made with particular emphasis on cavity length.

Figures 20, 21 and 22 show theoretical cascade performance for a cascade of the solidity ($c/t = .54$) used in the original first stage design.

As an initial check of these theoretical results, the relationship between camber, angle of attack and lift coefficient (f/cC_L and α/C_L) for long cavities ($\ell/c \geq 3$) were compared with results for cascades with infinite length cavities as used for propeller design. Figures 20 and 21 indicate that the behavior of the cascade becomes constant for cavity lengths greater than three chords, and that the performance for that region should be essentially the same as for cascades with infinite cavity lengths For the cascade geometry at the characteristic radius ($\gamma = 79^{\circ}18'$ $f/c = 0.0143$, $c/t = 0.54$) and using $\rho/cC_L^2 = 0$ and $\ell/c > 3.0$. Figures 20 and 21 give a theoretical lift coefficient of 0.071 and an angle of attack of 0.071. Data for two-dimensional isolated constant pressure foils and theoretical results for cascades with infinite cavity lengths (24) yield an estimated lift coefficient of 0.070 for this same cascade geometry (solidity, stagger angle, angle of attack, and camber). The excellent agreement of this value with the present theoretical value indicates that Figures 20 and 21 are valid for long cavities ($\ell/c \geq 3.0$).

Data from the present test program was then used to check the consistency between the results of Figures 20 and 21 in the region of finite cavity lengths. For a given measured cavity length, blade angle of attack, and flow coefficient the lift coefficient at the characteristic radius was determined using

Figure 20. The cavity length corresponding to this lift coefficient and the design camber (f/c = 0.0143) was then determined from Figure 21 and compared with the measured value. The two cavity lengths are in quite good agreement as seen in Figure 23. Based on this comparison it can be concluded that the results of Figures 20 and 21 are consistent for both finite and infinite cavity lengths.

The lift coefficient obtained from Figure 20 as described above was the corresponding head coefficient, and these values compared with the experimentally measured head coefficients. Assuming the head coefficient is proportional to the lift coefficient at the characteristic radius, which should be a good approximation, the head coefficient can be estimated as:

$$\psi = (\psi \text{ design}) \frac{C_L}{C_{L \text{ design}}} = .1875\ C_L \qquad [12]$$

A comparison of the measured and calculated head coefficients, again showed quite good agreement further indicating the validity of Figures 20 and 21.

The discrepancies between measured and theoretical head coefficients are thus likely to be due to some error in the results given by Figure 22. That is, the theory of Yim (11) appears to reasonably predict the relationship among cavity length, camber, angle of attack, and lift coefficient, but fails to predict the relationship between cavity length and cavitation number.

The difficulty in relating cavity length to cavitation number has been common in most theoretical work on finite cavity length supercavitating flows.

It was shown by Tulin (25) that for supercavitating struts and lifting foils, the cavity length is directly proportional to the scaling parameter, C_D/σ^2. The original relationship for lifting foils at small σ was given by

$$(\ell/c - 1) \sim \left(\frac{8}{\pi} \frac{C_D}{\sigma^2}\right) \quad \text{as } \sigma \to 0 \qquad [13]$$

Available data and later theoretical models indicate wide variations in the constants of proportionality between the cavity length and the scaling parameter. In order to examine the validity of Figure 22, the theoretical and experimental values of C_L were used to calculate the parameter, k, defined as:

$$\ell/c = k \frac{C_D}{\sigma_e^2} = k \frac{\alpha C_L}{\sigma_e^2} \qquad [14]$$

It should be noted that the cavitation number in Equation [14] is not the inlet cavitation number σ_i, of Figure 22 but rather an average or effective cavitation number, σ_e. Previous studies of cavities in pressure gradients (26) and behind supercavitating propellers (27) indicate that an effective cavitation number based on the pressure at 40 percent of the cavity length

(measured from the leading edge) correlates well with cavity length. The resulting effective cavitation number for a cascade (assuming a linear pressure rise across the foils) is given by

$$\sigma = \sigma_i \left[1 + .40 \frac{\ell}{c} \left(\frac{C_L}{\sigma_i} \frac{c}{t} \right) \right] \qquad \text{for } 0.40\ \ell/c \leq 1.0 \qquad [15]$$

and

$$\sigma = \sigma_i \left[1 + \left(\frac{C_L}{\sigma_i} \frac{c}{t} \right) \right] \qquad \text{for } 0.40\ \ell/c > 1.0 \qquad [16]$$

The results of Figure 22 for $\rho/cC_L^2 = 0$ have been analyzed using Equation [15] to determine the values of the constant k of Equation [14]. The resulting values of k are presented in Figure 24 as a solid line. These k values range from 0.60 to 1.20.

The experimentally measured performance has also been analyzed, and the values of k determined for various operating conditions using calculated values of $(C_L/\sigma_i)(c/t)$. These results are also shown in Figure 24.

From the measured data, there appears to be a somewhat linear relationship between k and ℓ/c. The significance of this relationship is not known but a straightline fit through the data is shown in Figure 24. The equation of the line is:

$$k = .833\ \ell/c + .167 \qquad [17]$$

The values of k from the tests are, generally, within the range of values predicted by existing isolated foil theories (28) and existing data.

Also shown in Figure 24 is a region bounded by 2 times and 3 times the k values from the theory. It can be seen that the majority of the experimental points fall within this region.

To correct a figure such as Figure 22 for the differential between the theoretically determined k values and the values from the experiments it is necessary to multiply the theoretical cavity lengths by the ratio of the k values. The resulting reduction in the lift parameter $(C_L/\sigma_i)(c/t)$ for a given cavity length is obvious.

Because of the large reductions in the values of the lift parameter, it is thus necessary to increase the pump solidity over the values required by the theory of Yim (11) to obtain the desired headrise at the desired σ_i.

It should further be noted that there exist inherent inaccuracies in the linear theory for cascades with high stagger angles. This problem was discussed in Reference 11. At high stagger angles predictions using linear theory lose accuracy at higher solidities and angles of attack. Previous investigators (19, 20, 21 and 22) have presented numerical results for lower stagger angles only (i.e. 60° and less).

6.2 Second Stage, Inducer Number 1

The second stage operated with minimum cavitation at a flow coefficient only 37 percent of the design flow coefficient. As the operating flow coefficient was increased, face cavitation developed indicating negative angles of attack at the leading edge. It was thus concluded that the blades were inducing higher tangential velocities ahead of the impeller than used in the design. The impeller also developed a higher head coefficient than the design value, indicating that the theory (Reference 6) failed to predict the downstream vorticity correctly. The theory of Reference 13 utilized the theoretical results presented in Reference 17, in which velocities induced by a radial line vortex in an annulus were derived numerically at specified axial and angular intervals. In the design of the second stage, induced velocities were required at smaller axial intervals than were available from the work of Tyson (17) and Bowerman (13). Hence, interpolation and extrapolation was necessary to obtain the induced velocities at the required intervals. In doing so, errors may have arisen leading to the incorrect prediction of induced tangential velocities. The results of Reference 17 should be made available at smaller axial intervals for use in the design of high solidity, high stagger angle impellers.

Figure 25 shows the radial distribution of measured parameters during test run no. 3 on the second stage. It can be seen that neither the total head nor the axial velocity remained constant along the radius as assumed in the design. This was caused

by flow separation along the hub section causing flow "pile up" at the tip sections. The diffusion factor (23) has been shown to correlate well with limiting blade loading or separation in axial flow compressor blades. The diffusion factor was derived beginning with a parameter frequently used in establishing a separation criterion in two-dimensional, turbulent boundary layer theory. After several simplifications and substitutions, the following form is obtained:

$$D = \left(1 - \frac{w_2}{w_1}\right) + \frac{\Delta V_u}{2(c/t)w_1}$$

Correlation with NACA compressor data shows that to avoid separation this factor should be less than 0.60. The present second stage design calls for diffusion factors at the tip radius, mid radius, and hub radius of 0.259, 0.362, and 0.701 respectively. The diffusion factor at the hub was too large because of the high head coefficient and low peripheral speed. It could be reduced by decreasing the head coefficient, increasing the peripheral speed or increasing the hub to tip diameter ratio.

7.0 DESIGN OF INDUCERS NO. 2 AND NO. 3

7.1 First Stages, Inducers 2 and 3

In order to improve the performance of the first stage of Inducer No. 1, it was necessary to increase the solidity and the camber of the blades. However, as was indicated in an earlier section of this report, it is a characteristic of constant-pressure cambered cascades that as the solidity increases, the camber of the foil decreases and tends to approach a flat plate. Because of this characteristic, it did not seem appropriate to use the results of the theory of Reference 11 for the new design. A study of other types of supercavitating foils in which the camber is an independent variable is currently being conducted as a continuation of the present work. When this study is complete, it should be possible to design an impeller with increased solidity and camber. For the purposes of the present study it was decided to study the effects of increased solidity, keeping the camber constant. Thus, the solidity was increased to 1-1/2 times that of Inducer no. 1 by using three blades instead of two, each blade of the new impeller identical with the blades used in Inducer no. 1. A photograph of this new impeller is shown in Figure 26.

The first stage of Inducer No. 3 was fabricated with 4 blades, each blade identical with those used in the first stage of Inducer No. 1. The solidity of the resulting impeller was 1.08 or twice that of Inducer No. 1. A photograph of the four-bladed first stage impeller is shown in Figure 27. Each of these impellers were tested at various pitch settings to determine the best performance.

7.2 Second Stages, Inducers 2 and 3

Since the second stage of Inducer No. 1 developed a more than adequate head coefficient (131 percent of design in run no. 3) but at less than the required flow coefficient, (37 percent of design in run no. 3) it was speculated that proper changes in the pitch of the blades might increase the flow coefficient without decreasing the head coefficient substantially. The second stage of Inducer No. 2 therefore had the blades pitched at $5\text{-}1/2^{\circ}$ less than those of Inducer No. 1. The second stage of Inducer No. 3 had the blades pitched at 10° less than Inducer No. 1.

8.0 RESULTS AND ANALYSIS OF TESTS ON INDUCER NO. 2

8.1 First Stage, Inducer Number 2

The first stage of Inducer No. 2 (3 blades) was tested at two pitch settings (67.5° and 63.5°). Figures 23, 25 and 26 present the results of tests at the first pitch setting. Figure 28 shows that the impeller performed well only at a flow coefficients near 0.07 Breakdown of the total head occurred at a suction specific speed of 20,600 but the head coefficient is improved over that developed by the first stage of inducer number 1. The form of the curve is different than that obtained previously, being almost flat until breakdown as compared to the continuous decreasing characteristic obtained for Inducer no. 1. The variation of efficiency under these test conditions is noted by each data point in Figure 28.

Since the flow coefficient, at which the above impeller operated satisfactorily, was less than the required value of 0.1, it was decided to change the pitch of the blades to increase the flow coefficient. The new pitch setting chosen was 63.5°. The results of tests at this setting are presented in Figure 29. The flow coefficient was indeed increased as had been anticipated, however, no significant improvement in the maximum achievable suction specific speed occurred. The efficiencies at all values of N_{ss} were significantly improved. Just previous to breakdown, the cavity lengths were $\ell/c = 1.6 - 1.8$. After breakdown, the cavities entirely filled the space between the impeller and the downstream guide vanes. Cavity length data is included in Figure 39 with additional test data for this impeller when tested in tandem.

8.2 Second Stage, Inducer Number 2

The new pitch of the second stage was 60.3°, 5.5° less than that of Inducer No. 1. At this pitch, the blades were further apart producing wider flow passages and allowing tests at a lower cavitation number before choking of the passages occurred. Figure 30 shows the results of tests on the second stage at this pitch setting. The flow coefficients for this impeller are much higher than those of the second stage of Inducer No. 1. At a flow coefficient of 0.064, the impeller was able to develop a higher-than-design head coefficient at a higher-than-design suction specific speed. At the higher values of N_{ss}, face cavitation occurred and choked the passages. Some cavitation also occurred on the suction side of the blades but only from about mid chord on to the trailing edge of the blades. The radial distribution of parameters in this case was about the same as that for the second stage of Inducer No. 1 (Figure 25) and is not presented again.

9.0 RESULTS AND ANALYSIS OF TESTS ON INDUCER NO. 3

9.1 First Stage, Inducer Number 3

The first stage of Inducer No. 3 was tested at two different pitch settings, at 48.5° and 53.5°. The results of tests on the first stage at 48.5° pitch are shown in Figure 31. At this pitch, tests were conducted at $\phi > 0.125$. Even at this high ϕ the angle of attack was large and hence a very thick cavity developed behind each blade. The cavitation performance of this stage was thus inferior to that of Inducers No. 1 or No. 2. The highest N_{ss} obtained at this flow coefficient was 15,300. The head coefficient for this impeller was higher than that of the previous inducers because of the increased solidity and angle of attack. The maximum stable cavity length to chord ratio obtained was 1.15. As the cavitation number was decreased, the cavity length suddenly became very long and extended downstream to the guide vanes.

Since the angle of attack was too large at the pitch setting of 48.5°, the blades were reset at a pitch of 53.5° and the impeller tested. The results of these tests are presented in Figure 32. It can be seen that the head coefficient developed at this pitch is higher than that developed at the previous pitch setting, and the cavitation performance is slightly better, although it is not as good as that of Inducer numbers 1 or 2.

A summary of the performance of the Stage 1 models with various pitches and numbers of blades is presented in Figure 33. Stage 1 of inducer no. 2 with 3 blades pitched at 63.5° was chosen as the most acceptable first stage.

9.2 Second Stage, Inducer Number 3

The second stage of inducer no. 3 had blades pitched 10° less than the pitch of inducer no. 1. The results of tests at this new pitch are presented in Figure 34. The best cavitation performance occurs at a flow coefficient of 0.088 as compared with 0.064 for stage 2 of inducer no. 2. Both the head coefficient and the suction specific speed were in excess of the design requirements at this flow coefficient. The design ψ and N_{ss} could not be achieved, however, at a flow coefficient of $\phi = .097$. The pattern of cavitation at the higher values of N_{ss} was the same as that on the second stage of inducer no. 2. That, is face cavitation occurred at the leading edge for 0.1 - 0.2 of the chord and back cavitation occurred from about 0.5 chord to the trailing edge.

10.0 EXPERIMENTAL RESULTS OF TESTS ON TANDEM INDUCERS WITH -6 INCH AND -1.5 INCH OVERLAPS

A tandem model using Stage 1 of inducer no. 2 (3 blades at 63.5°) and stage 2 of inducer no. 3 (6 blades at 55.8°) was tested at -6 inches overlap and 0° offset. This model is shown assembled in Figure 35. The performance in terms of head and efficiency is shown in Figure 36. Note that in tandem, the characteristic of higher head generation at lower flow coefficients which appeared in nearly all tests of either stage alone did not occur. First stage cavity length to chord ratios of 1.60 and 2.00 at respective flow coefficients of .075 and .083 are the maximum values which can be tolerated prior to flow breakdown. Total head generation was considerably in excess of the required $\psi = 0.25$ and maximum N_{ss} values ranged from 21,500 to 23,000 depending on flow coefficient. The total tandem efficiency varied from 55 to 70 percent with higher efficiency at higher flow coefficients.

Using the same individual stages the overlap was reduced from -6 inches to -1.5 inches as shown in Figure 37. Figure 38 shows that the head coefficient $-N_{ss}$ performance varied little from the -6 inch overlap performance for a similar range of flow coefficients. Two major differences may be noted. First, the data collapsed to a single curve approximately midway between the two performance curves presented for the -6 inch overlap. Secondly, breakdown occurred at about $N_{ss} = 22,000$ but with a cavity length of 1.50, shorter than the breakdown ℓ/c values for the -6 inch overlap.

To further evaluate the effect of tandem "stacking" of the stages, the performance of each stage in tandem was compared to the performance of each stage when tested alone. Figure 39 shows the performance of the first stage when tested alone and its performance when in tandem with each of the overlaps used. A continuous spectrum of performance can be constructed using all of the data available. These results show little effect of the presence of Stage 2 on Stage 1 performance. Included in Figure 39 are lines of approximately constant cavity length. Cavity length observations are difficult to make and considerable interpolation was required to draw the cavity length lines as shown.

Figure 40 shows the performance of Stage 2 when tested alone and in tandem. The performance of the second stage has been considerably modified due primarily to the "prerotation" from the swirl introduced by Stage 1. In the isolated case, performance degradation at higher values of N_{ss} was caused by cavitation and choking. In the tandem case performance degraded at lower values of N_{ss} as well. This degradation can be explained by the fact that as inlet N_{ss} decreases, Stage 1 generates higher heads and thus introduces more "prerotation" to Stage 2. Higher values of prerotation to Stage 2 mean lower angles of attack and therefore lower head generation. As the Stage 1 head generation decreases, the Stage 2 performance in tandem approaches the isolated Stage 2 performance. This "trade-off" in head generation is shown in Figure 41 where the percentage of total head generated by the second stage is shown as a function of inlet N_{ss} to Stage 1. This

phenomenon is particularly valuable in the operation of an inducer over a range of N_{ss} values such as might occur during a rocket flight because of the resultant flat characteristic of the head - N_{ss} curve as shown in Figures 36 and 38. The total efficiency curves are also flat over a wide range of N_{ss} values.

The cavity lengths presented in Figures 36 and 38 for the first stage are supplemented in Figure 42 where the relatively more complex cavitation patterns observed for Stage 2 are summarized in a plane defined by flow coefficient and second stage N_{ss}. The major types of second stage cavitation recorded were tip, face, and back cavities. Using second stage N_{ss} automatically accounts for the head rise from Stage 1 when the inducer was tested in tandem. A number of the data points in Figure 42 have solid symbols indicating that the axial velocity profiles leaving Stage 2 indicated separation or near separation at the hub. This is of course undesirable and could be alleviated through the use of a larger hub/diameter ratio for Stage 2 or possibly a tapered hub for this stage.

11.0 OPTIMUM TANDEM INDUCER PERFORMANCE COMPARED TO ORIGINAL DESIGN REQUIREMENTS

In order to compare the performance of the final tandem inducer selected to the original design requirements, the operating point where the distribution of head generation between the first and second stages matched the original design point distribution was chosen. This point is where 15 percent of the total head is generated by the first or supercavitating stage and 85 percent by the second or subcavitating stage. From Figure 41 this occurs at about N_{ss} = 22,000 for the six inch overlap and N_{ss} = 22,500 for the 1.5 inch overlap.

Using N_{ss} = 22,000 for Stage 1 and $\phi \approx .083$, from Figure 36 the head coefficient generated is approximately $\psi = 0.29$ and the first stage cavity length $\ell/c = 1.75$. Overall efficiency at this point is 62 percent. This operating point is shown as a solid triangular symbol in Figure 36. Similarly for a 1.5 inch overlap, the same operating point is shown in Figure 38. In this case the first stage cavity length is about $\ell/c = 1.50$ and the overall efficiency 66 percent.

The following table summarizes the optimum experimental inducer performance and compares these results to the original design parameters.

TABLE 2

Summary of Tandem Inducer Performance

Operating Parameter	Original Design Value	Experimental Value at -1.5 inch overlap	Experimental Value at -6 inch overlap
N_{ss}, entrance	30,000	22,000	22,000 to 23,000
ϕ_o, average	0.100	0.083	0.083
ψ, total	0.250	0.283	0.296
ψ_{2nd}/ψ_{1st}	0.85	0.85	0.85
η_T, total	65% (1st stage only)	66%	62%
Stage 1 Pitch	63.5°	63.5°	63.5°
Stage 1, No. of blades	2	3	3
Stage 1, Char. solidity	0.540	0.810	0.810
Stage 1, ℓ/c	1.50	1.50	1.75
Stage 2, N_{ss}	13,250	10,600	10,600
Stage 2, pitch	65.8°	55.8°	55.8°
Stage 2, no. of blades	6	6	6
Stage 2, Char. solidity	2.43	2.43	2.43

12.0 FLUCTUATING PRESSURE MEASUREMENTS

Unsteady components of the flow through the inducers generated fluctuating pressures which were recorded and analyzed for intensity and frequency. A pressure measuring system capable of measuring frequencies up to 10,000 cps with flat response was designed for this purpose. The main components of the system were a piezoelectric pressure gage, an impedance matching unit, a wave analyzer, and a level recorder. Figure 43 shows the details of the gage mounting located in the stainless steel portion of the test section about one diameter ahead of the impeller. The system was designed for the high natural frequency based on some preliminary test runs indicating that under heavy cavitation, the fluctuating pressure contained energy at 6000 cps and sometimes at 10,000 cps. The piezoelectric gage was calibrated such that 1 mv was generated for 0.125 psi or 362 dynes/cm^2. This level was used as the 0 dB reference.

The sound pressure level (SPL) in decibels is defined as

$$SPL = 20 \log \left(\frac{p_e}{p_o} \right) \qquad [19]$$

where

p_e is the effective pressure of the acoustic wave, and

p_o is the reference pressure.

The standard reference pressures usually used in water are .0002 dynes/cm^2 and 1 dyne/cm^2. If 58.6 dB are added to the values reported in this text, the resulting values will be referred to the standard reference of 1 dyne/cm^2.

All frequency distribution recordings indicated a high energy level at the shaft rpm frequency of 66.7 cps. It was assumed that pressures encountered at this frequency were likely to come from mechanical vibration of the test facility. The signal at this frequency was therefore subtracted from the overall level and the remainder attributed to actual pressure fluctuations in the flow. In most cases, pressure fluctuations were detected at the blade passage frequency and its harmonics. The level at the fundamental was not always highest and the pressure fluctuations due to cavitation were often more intense. The frequencies at which fluctuations occurred due to cavitation varied with degree and type of cavitation. In single stage tests, the frequencies most often encountered were continuously distributed with peaks at 500, 1000, 2000 and sometimes 6000 and 10,000 cps. The distribution was dependent on both cavitation number and flow coefficient. At high cavitation numbers (low N_{ss}) when first stage impellers were partially cavitating, pressures at all the above mentioned frequencies were present. As N_{ss} was increased and the cavities grew longer, the signals at 6 and 10 kc disappeared. Supercavitation resulted in a general decrease in noise level and a shift in distribution toward the blade passage frequency. Figure 44a shows a recording for the 0 - 4000 cps range for a supercavitating impeller operating in a partially cavitating condition with N_{ss} = 13,900 and cavity length about equal to the chord. Strong fluctuations due to cavitation exist from 500 to 2000 cps. A less severe range of fluctuations also existed at

around 9000 cps as shown in the insert. The overall noise level for this operating point was 40.0 dB. Figure 44b shows the result of increasing the suction specific speed on the same impeller to 21,000. The fluctuations due to cavitation are considerably reduced, the high frequency components have disappeared, and the overall noise level has dropped to 34.7 dB. The cavity length has increased to about 1.50.

Figure 45 shows the effect of suction specific speed on the ratio of total pressure fluctuation level to the total head generated during tests of Stage 1, inducer no. 2 and Stage 2, inducer no. 3 tested as isolated stages and in tandem with both overlaps. The total fluctuation level in tandem was higher than that of either stage alone but lower than that of Stage 1 when presented as a fraction of total head generation. In tandem minimum fluctuations take place around cavity length, $\ell/c = 1.30 - 1.40$. The region of maximum fluctuations occurs in the range of $\ell/c = 0.90$ to 1.10. This is in agreement with the analysis of Barr (30) which indicated a range of likely cavity instabilities to be between 0.75 and 1.15. The work of Geurst (31) as summarized in (30) indicates that in cavity flow over a partially cavitating flat plate hydrofoil instabilities occur when ℓ/c exceeds 0.75. Furthermore, cavity lengths in some helical inducer tests (32, 5) have been reported to typically lie between 0.70 and 1.0. The flow coefficients among the various curves in Figure 45 are not the same. Direct comparison is, therefore, somewhat difficult. In the tandem tests, the high frequency noise in the 10,000 cps range was not present, in fact, noise was rarely recorded above 3,000 cps in the tandem.

It was not possible from the fluctuating pressure measurements to consistently identify the mode and extent of the cavitation on the inducer models except in a very qualitative manner. Some indications of alternate blade cavitations were noted when the peak at 1/2 the blade passage frequency exceeded the level at the blade passage frequency. Conclusive evidence of rotating stall type instabilities was not obtained.

13.0 SUMMARY, CONCLUSIONS, AND RECOMMENDATIONS

High suction specific speed pump inducers for use in rocket fuel/oxidizer pump applications result in reduced propulsion system weight and therefore increased payload. Operating at low inlet pressures, the inducers cavitate. The problem of flow instability is a significant limiting condition for acceptable operation. The tandem row inducer has been suggested as a means for reducing these instabilities. In the present study, the first stage of the tandem row inducer is designed to be "supercavitating" and the second cavitation free. Studies of flow instabilities using water for the model are conservative compared to prototype operation in cyrogenic fluids.

The design of the supercavitating first stages required a knowledge of the performance of two-dimensional supercavitating cascades. This performance was theoretically studied for the case of the constant pressure cambered blade (Yim, 11, 12). A generalized theory of rotating stall (Yeh 10) was used as the criterion to design a stable impeller. The characteristics of constant pressure cambered cascades indicate they are not the most suitable camber for the design of supercavitating impeller. As the solidity is increased, the camber of the foil decreases approaching a flat plate. Simultaneously, the range of cavitation number over which the cascade is supercavitating, yet stable, is narrowed.

The second stage of the tandem row inducer was designed using the method presented by Bowerman (13). The design technique accounts for induced interference effects at an impeller blade as influenced by the other blades and the total downstream vorticity along the pump centerline. A basic requirement is the distribution of velocities induced by a radial line vortex in an annulus (Tyson, 17). The advantage of the design procedure is that no theoretical or experimental data on high solidity cascades is necessary. Disadvantages lies in lack of previous verification for high solidity design and the fact that section drag does not appear in the design procedure.

Both the first and second stage designs required empirical modifications to improve performance. In the first stage case, both solidity and blade pitch were adjusted. For the second stage only blade pitch was modified.

The following points summarize the primary results of the experimental test program:

1. The best performance for an isolated supercavitating first stage was obtained for a model using 3 blades ($c/d = 0.810$) at the original design pitch of 63.5° (Stage 1, Inducer 2).

2. The best performance for an isolated second stage was obtained for a model using 6 blades ($c/d = 2.43$) with a pitch of 55.8°, 10° less than the original design value (Stage 2, Inducer 3).

3. These stages were then tested in tandem. In tandem little difference was observed between performance at -6 inch overlap and -1.5 inch overlap.

4. Performance of the supercavitating first stage in tandem was consistent with the isolated tests on the same stage. Second stage performance, however, was considerably altered due to"prerotation" from Stage 1.

5. A complete summary of performance parameters for the tandem inducer operated at both overlaps is presented in Table 2. The tandem model produced more than the design head coefficient (0.29/0.25) at slightly less than the design flow coefficient (.083/.100) and less than the design suction specific speed (22,000/30,000). First stage cavity lengths were approximately as required by the original design (1.50-1.75/1.50).

6. The "trade-off" of head generation between the first and second stages of the tandem inducer produces a relatively flat $\psi = N_{ss}$ characteristic well suited to rocket fuel pump applications where N_{ss} may vary during the course of a flight.

The experimental performance, while not quite reaching the design objectives does indicate that the tandem inducer using a supercavitating first stage has definite potential as a high suction specific speed design concept. Low frequency instabilities or oscillations were noted only at or near breakdown and appeared to stem from unstable cavity lengths rather than from Yeh (10) type instabilities which the original design was intended

to avoid. Further manipulation of the pitch of the tandem inducer stages (in particular smaller pitch angles for Stage 1) may have reduced the head coefficient and increased the flow coefficient bringing each closer to the design values. This would probably have resulted in higher breakdown N_{ss} values because of the smaller angles of attack. It is doubtful, however, with the present blade shapes that the design goal of 30,000 could have been reached.

Higher-term cambered first stages, should improve the suction performance of the tandem inducer considerably. Cavitation damage to the first stage blades in the present model indicates that the blades were definitely not of optimum shape for the present application. Even so, the tandem performance was marginally acceptable.

The original second stage design apparently induced a larger swirl than predicted by the theory (13). In order to improve the prediction of induced velocities, the velocities induced by a radial line vortex in an annulus (17) should be calculated for smaller axial and circumferential spacings and for larger hub to diameter ratios.

In later designs, careful selection of the hub/diameter ratio or the use of tapered hubs may improve the suction performance of Stage 1 and lessen the tendency toward separation at the hub in Stage 2. As noted, the primary source of instabilities in the present case appeared to be unstable cavity lengths leading to "infinite" cavities which extend into the second stage and cause complete flow breakdown. Since cavity length, as verified by the

present and other experimental studies (24), is critically sensitive to cavitation number the use of "artificial" methods to terminate first stage cavity length may be advantageous. Two possible means are the tapered hub in which centrifugal as well as blade lift forces may be used to increase the head rise across Stage 1 (mixed flow impeller) or a diffusing region between stages 1 and 2 to convert more of the swirl added by Stage 1 to static pressure rise before entering Stage 2.

Some loss of efficiency may occur due to the second technique. Another design feature which could prove advantageous is the addition of prerotation into Stage 1 since it would allow the use of lower stagger angles in Stage 1. As shown in Reference 3 cascade performance degrades rapidly with stagger angle.

14.0 ACKNOWLEDGMENTS

The authors gratefully acknowledge the technical advice and assistance of Mr. Virgil E. Johnson, Jr., Dr. Boyun Yim, Mr. Roderick Barr and Mr. C. C. Hsu and the assistance of Mr. J. McBeth and Mr. R. Bateman in the experimental program.

15.0 REFERENCES

1. Daily, J. W., "Theory of Turbomachinery," Chapter 8 in Engineering Hydraulics, H. Rouse, ed., Wiley, 1961.

2. Ross, C. C. and Banerian, G., "Some Aspects of High Suction Specific Speed Pump Inducers," Transactions ASME, Vol. 78, Number 8, 1956.

3. Pinkel, I. I., et al., "Conference on Selected Technology for the Petroleum Industry," NASA SP-5053, Chapter 6, Pump Technology, December 1965.

4. Acosta, A. J., "An Experimental Study of Cavitating Inducers," Trans. 2nd Symp. on Naval Hydrodynamics, ONR Publication ACR-38, 1958.

5. Hartmann, M. J., and Soltis, R. F., "Observations of Cavitation in a Low Hub-Tip Ratio Axial Flow Pump," ASME Paper No. 60-Hyd-14, March 1960.

6. Iura, T., Discussion of Ref. 4 by Acosta, Trans. 2nd Symp. on Naval Hydrodynamics, ONR Pub. ACR-38, 1958.

7. Soltis, R. F., "Some Visual Observations of Cavitation in Rotating Machinery," NASA TN D-2681, July 1965.

8. Crouse, James E. and Sandercock, Donald, M., "Blade-Element Performance of Two Stage Axial Flow Pump with Tandem Row Inlet Stage," NASA TN D-3962, May 1967.

9. Lewis, G. W., Jr., Tysl, E. R., and Sandercock, D. M., "Cavitation Performance of an 83° Helical Inducer Operated in Liquid Hydrogen," NASA TM X-419, March 1961, Declassified October 1966.

10. Yeh, H., "An Actuator Disc Analysis of Inlet Distortion and Rotating Stall in Axial-Flow Turbomachines," Journal of the Aeronautical Sciences, Vol. 26, No. 11, 1959.

11. Yim, B., "Supercavitating Cascades with Constant Pressure Cambered Blades," HYDRONAUTICS, Incorporated Technical Report 703-2, July 1967.

12. Yim, B., "The Higher Order Theory of Supercavitating Cascades with Constant Pressure Cambered Blades," HYDRONAUTICS, Incorporated Technical Report 703-3, October 1967.

13. Bowerman, R. D., "The Design of Axial-Flow Pumps," Transactions ASME, Vol. 78, No. 8, 1956.

14. Wislicenus, G. F., "Fluid Mechanics of Turbomachinery," Volumes I and II, Dover Publications, New York, 1965.

15. Stepanoff, A. J., "Centrifugal and Axial Flow Pumps," 2nd Ed. John Wiley and Sons, N. Y., 1967.

16. "Aerodynamic Design of Axial-Flow Compressors," Volumes I, II and III, NACA RME56B03, August 1956.

17. Tyson, Jr., H. N., "Three Dimensional Interference Effects of a Finite Number of Blades in an Axial Turbomachine," Hydrodynamics Laboratory Report E-19.1, California Institute of Technology, November, 1952.

18. Abbot, T. H. and Von Doenhoff, A. E., "Theory of Wing Sections," Dover Publications, Inc., New York, 1959.

19. Betz, A., and Petersohn, E., "Application of the Theory of Free Jets," NACA TN 667, April 1932.

20. Cohen, H., and Sutherland, C. D., "Finite Cavity Cascade Flow," Proceedings of the 3rd U. S. National Congress of Applied Mechanics, 1958.

21. Acosta, A. J., "Cavitating Flow Past a Cascade of Circular Arc Hydrofoils," California Institute of Technology, Hydrodynamics Laboratory Report No. E-79-2, March 1960.

22. Wade, R. B., "Flow Past a Partially Cavitating Cascade of Flat Plate Hydrofoils," California Institute of Technology, Hydrodynamics Lab. Report No. E-79-4, Jan. 1963.

23. Lieblein, S., Schwenk, F. C., and Broderick, R. L., "Diffusion Factor for Estimating Losses and Limiting Blade Loadings in Axial-Flow-Compressor Blade Elements," NACA RM E53D01, June 1953.

24. Tulin, Marshall P., "Supercavitating Propellers History, Operating Characteristics, Mechanism of Operation," HYDRONAUTICS, Incorporated Technical Report 127-6, June 1964.

25. Tulin, M. P., "Supercavitating Flow Past Foils and Struts," in Cavitation in Hydrodynamics, Proc. N.P.L. Symposium London, 1956.

26. Acosta, A. J., "Effect of a Longitudinal Gravity Field on the Supercavitating Flow Over a Wedge," C.I.T. Report No. 79.1, May 1958.

27. Barr, Roderick, A., "An Investigation of the Cavity Flow Behind Drag Discs and Supercavitating Propellers," M. S. Thesis, University of Maryland, June 1966.

28. Tulin, Marshall P., "The Shape of Cavities in Supercavitating Flows," HYDRONAUTICS, Incorporated Technical Report 121-5, April 1965.

29. Eisenberg, P. and Tulin, M. P., "Cavitation", Chap. 12 in Handbook of Fluid Dynamics, V. L. Streeter, ed., McGraw-Hill, 1961.

30. Barr, R. A., "Study of Instabilities in High Head Tandem Row Inducer Pumps," HYDRONAUTICS, Incorporated Interim Technical Report 703-1, February 1967.

31. Geurst, J. A., "Linearized Theory of Two-Dimensional Cavity Flows," Doctoral Thesis, Technical University of Delft, Published at the Hague, 1961.

32. Oshima, M., and Kawaguchi, K., "Experimental Study of Axial and Mixed Flow Pumps," Proc. IAHR Symposium on Cavitation in Hydraulic Machinery: Sandai, Japan, 1962.

APPENDIX A

THE DESIGN OF THE FIRST STAGE

(a) Equations used in the Design of the First Stage

The following equations have been derived from two-dimensional, incompressible cascade theory:

$$\frac{C_{L_1}}{\sigma}\frac{c}{t} = \frac{2gH}{\sigma w_1^2}\frac{V_f}{U}\frac{\cos\alpha_1}{\eta\cos(\beta_1 - \alpha_1)} \qquad [A-1]$$

$$= \frac{2gH}{\sigma w_1^2}\frac{V_f}{U}\frac{1}{\cos\beta_1} \qquad [A-2]$$

$$= \frac{2gH}{\sigma w_1^2}\frac{1}{\sin\beta_1} = \frac{2gH}{\sigma U^2}\sin\beta_1 = \frac{2\psi}{\sigma}\sin\beta_1 \qquad [A-3]$$

$$C_{D_1}\frac{c}{t} = w_1\frac{\cos\beta_1}{\sin^2\beta_1} \qquad [A-4]$$

$$\text{Efficiency } \eta = \frac{1 - C_{D_1}/C_{L_1}\cot\beta_1}{1 + C_{D_1}/C_{L_1}\tan\beta_1} + \frac{\Delta V_u}{2U} \qquad [A-5]$$

$$\text{Reaction Ratio } R_r = \frac{1}{\eta}\frac{V_f}{U}\tan(\beta_1 - \alpha_1) \qquad [A-6]$$

$$= 1 - \frac{\psi}{2\eta} \qquad [A-7]$$

(b) Details of First Stage of Tandem Row Inducer

The first stage of the tandem row inducer is a two bladed, supercavitating impeller that will develop 15 percent of the total inducer head and be theoretically free of instabilities. Table A-1 presents a summary of the design at three different radii of the impeller. The head to be generated at the hub was reduced by 10 percent to increase the stability at that section. This increase in head produced little effect on the overall performance of the inducer. It was verified that at a section close to the hub (R = 2.25") the total head could be developed without any instability.

TABLE A-1

Summary of Design of Stage 1

Total Head = .15 x 200 - 30 ft.

Discharge = 4.28 cfs = 1925 gpm

Pump rpm = 5200

Specific Speed N_s = 17,900

Net Positive Suction Head = 15.0 ft.

Suction Specific Speed N_{ss} = 30,000

Hub to Tip Diameter Ratio = 0.6

Number of Blades = 2

Quantity	Tip Radius R = 3.5"	Characteristic Radius R = 2.88"	Hub Radius R = 2.1".
Total Head H, ft.	30	30	27
Cavitation No. σ_1	0.0130	0.0189	0.0346
Peripheral Speed U, fps	160	132	96
Relative Inlet Angle β_1	$81^\circ 07'$	$79^\circ 18'$	$75^\circ 24'$
Relative Mean Angle β_∞	$80^\circ 56'$	$78^\circ 59'$	$74^\circ 43'$
Relative Exit Angle β_2	$80^\circ 46'$	$78^\circ 39'$	$73^\circ 58'$
Relative Inlet Velocity w_1 fps	162	134.4	99.2
Relative Mean Velocity w_∞ fps	159	130.8	94.9
Relative Exit Velocity w_2 fps	155.9	127.1	89.5
Flow Velocity V_f, fps	25.0	25.0	25.0

TABLE A-1 (Continued)

Quantity	Tip Radius R = 3.5"	Characteristic Radius R = 2.88"	Hub Radius R = 2.1"
ΔV_u, fps	6.04	7.32	9.06
$\frac{C_L}{\sigma}\frac{c}{t}$	5.86	5.72	5.19
c (in.)	5.57	4.89	3.92
c/t	0.507	0.540	0.595
C_L	0.150	0.200	0.302
Angle of Attack α_1	$3^\circ 49'$	$5^\circ 16'$	$8^\circ 29'$
Angle of Attack α_m	$4^\circ 00'$	$4^\circ 57'$	$7^\circ 48'$
Degree of Reaction R	0.99	0.982	0.860
Section Efficiency η	0.68	0.675	0.646
Turning Parameter $N = \frac{d(\tan \beta_2)}{d(\tan \beta_1)}$	0.898	0.894	0.804
Loss Parameter = M_{limit} from Yeh's theory	0.672	0.605	0.827
Calculated M for section	0.567	0.513	0.786
M/M_{limit}	0.844	0.846	0.950

APPENDIX B

The design details of the second stage of the tandem row inducer are tabulated in Table B-1. This impeller is a 6 bladed, high solidity rotor, designed to be free of cavitation at the design condition.

TABLE B-1

Summary of Design of Stage 2

Total Head = 0.85 x 200 = 170 ft. of water
Discharge = 4.28 cfs = 1925 gpm
Impeller rpm = 5200
Specific Speed = 4880
Net Positive Suction Head = 45 ft. of water
Suction Specific Speed = 13,250
Hub to Tip Diameter Ratio = 0.6
Number of Blades = 6

Quantity	Tip Radius R = 3.5"	Mid Radius R = 2.8"	Hub Radius R = 2.1"
Peripheral Speed U, fps	160.0	132.0	96.0
Relative Inlet Angle, β_1	$80^\circ 46'$	$78^\circ 39'$	$73^\circ 58'$
Relative Mean Angle, β_∞	$79^\circ 38'$	$76^\circ 27'$	$66^\circ 41'$
Relative Outlet Angle, β_2	$78^\circ 12'$	$73^\circ 18'$	$49^\circ 11'$
Relative Inlet Velocity, w_1, fps	155.9	127.1	90.4
Relative Mean Angle, w_∞, fps	139.0	106.9	63.1
Relative Outlet Velocity, w_2, fps	122.5	86.9	38.3
Cavitation Number σ	0.0672	0.100	0.176
Flow Velocity, V_f, fps	25.0	25.0	25.0
ΔV_u, fps	34.2	41.5	58.0
C_L (c/t)	0.492	0.777	1.84
C_L	0.206	0.347	0.708
c/t	2.40	2.43	2.57
c, inches	8.876	7.204	5.132

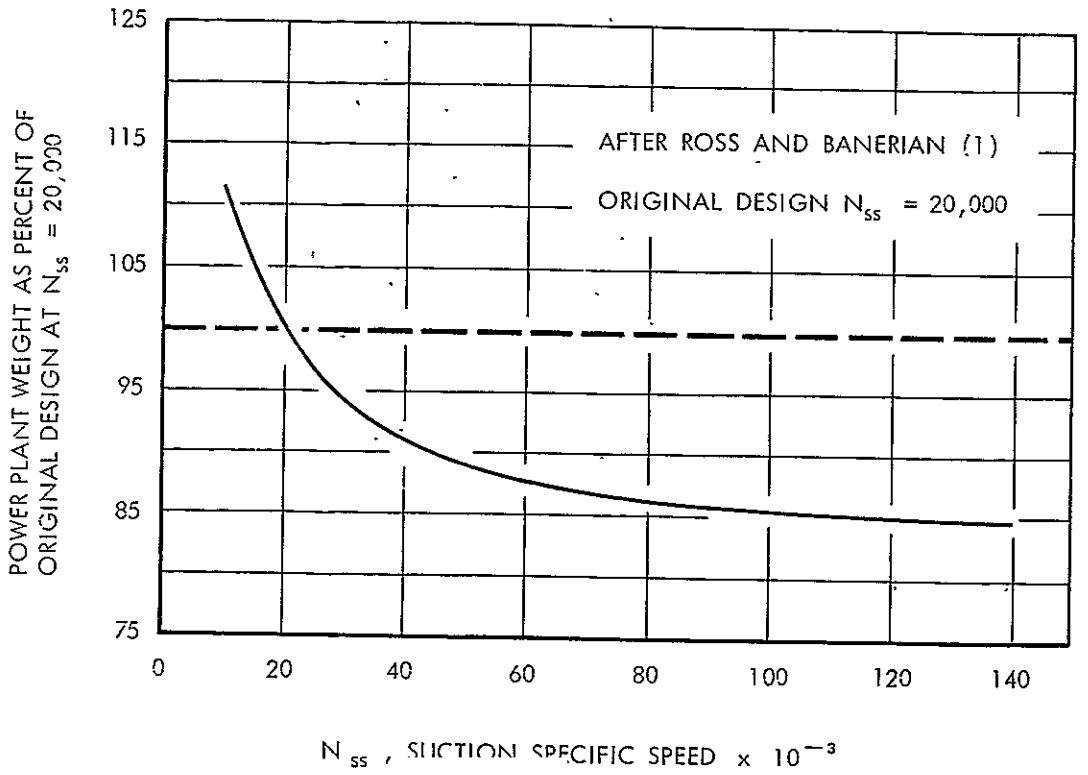

FIGURE 1 - EFFECT OF SUCTION SPECIFIC SPEED ON TOTAL POWER PLANT WEIGHT FOR A TYPICAL ROCKET ENGINE

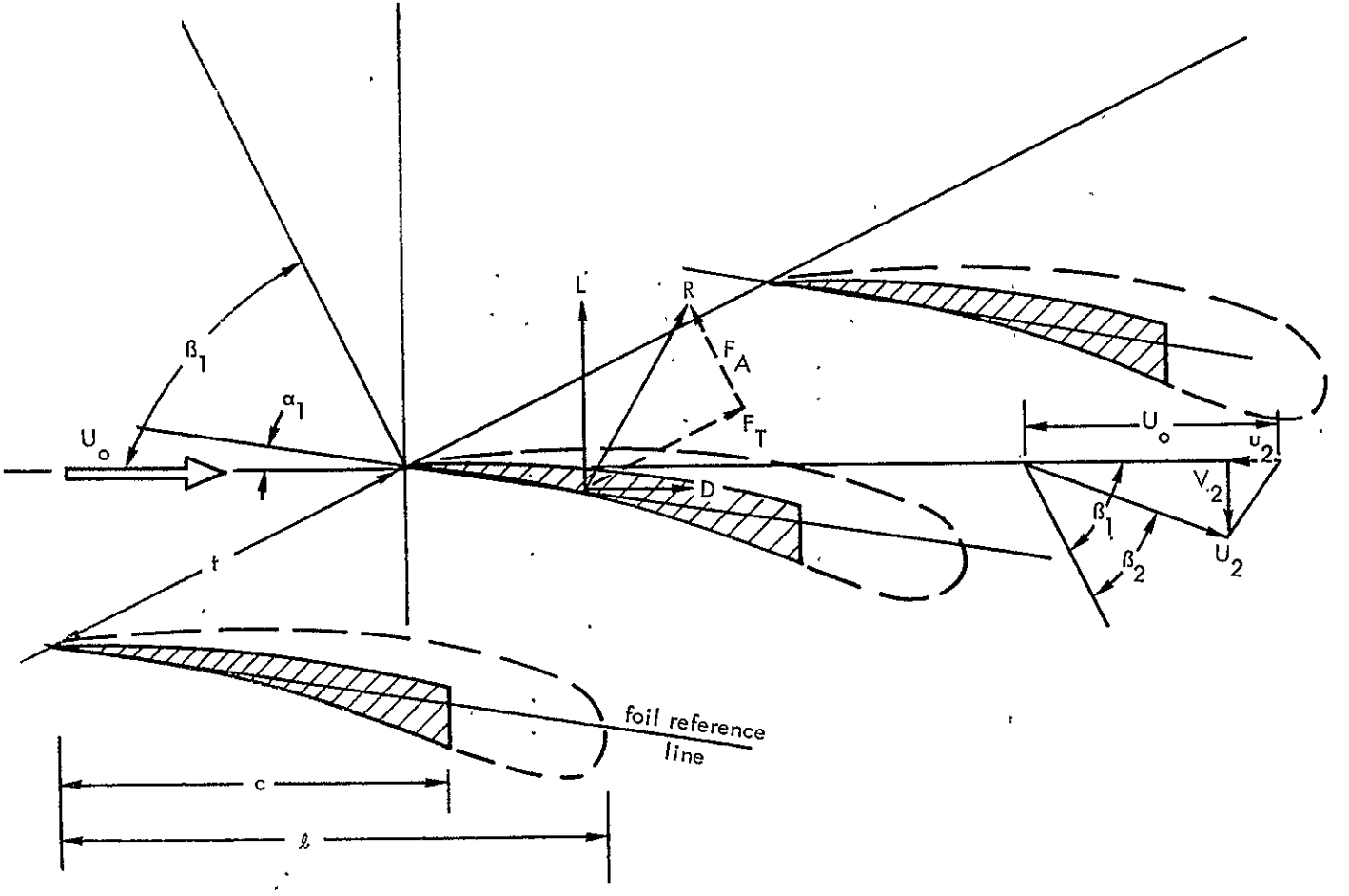

FIGURE 2a - DEFINITION SKETCH FOR A TWO DIMENSIONAL SUPERCAVITATING CASCADE

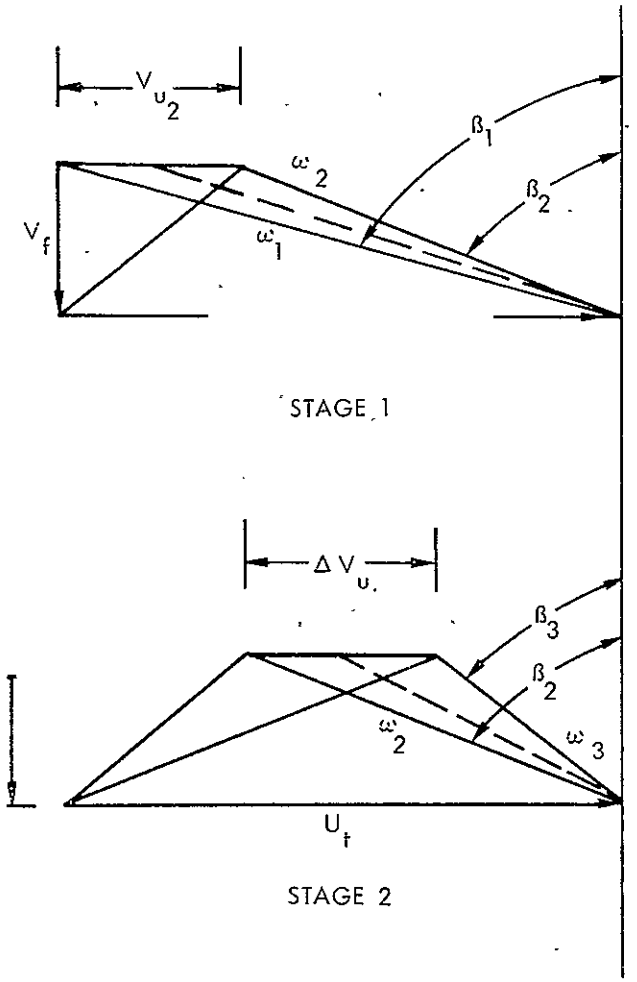

NOTES:

$\omega_1 = U_o$ OF FIGURE 2a

$\omega_2 = U_2$ OF FIGURE 2a

V_f = AXIAL FLOW VELOCITY

U_t = TANGENTIAL SPEED OF IMPELLER

V_u = SWIRL VELOCITY

FIGURE 2b - VELOCITY TRIANGLES FOR FIRST AND SECOND STAGES OF A TANDEM INDUCER

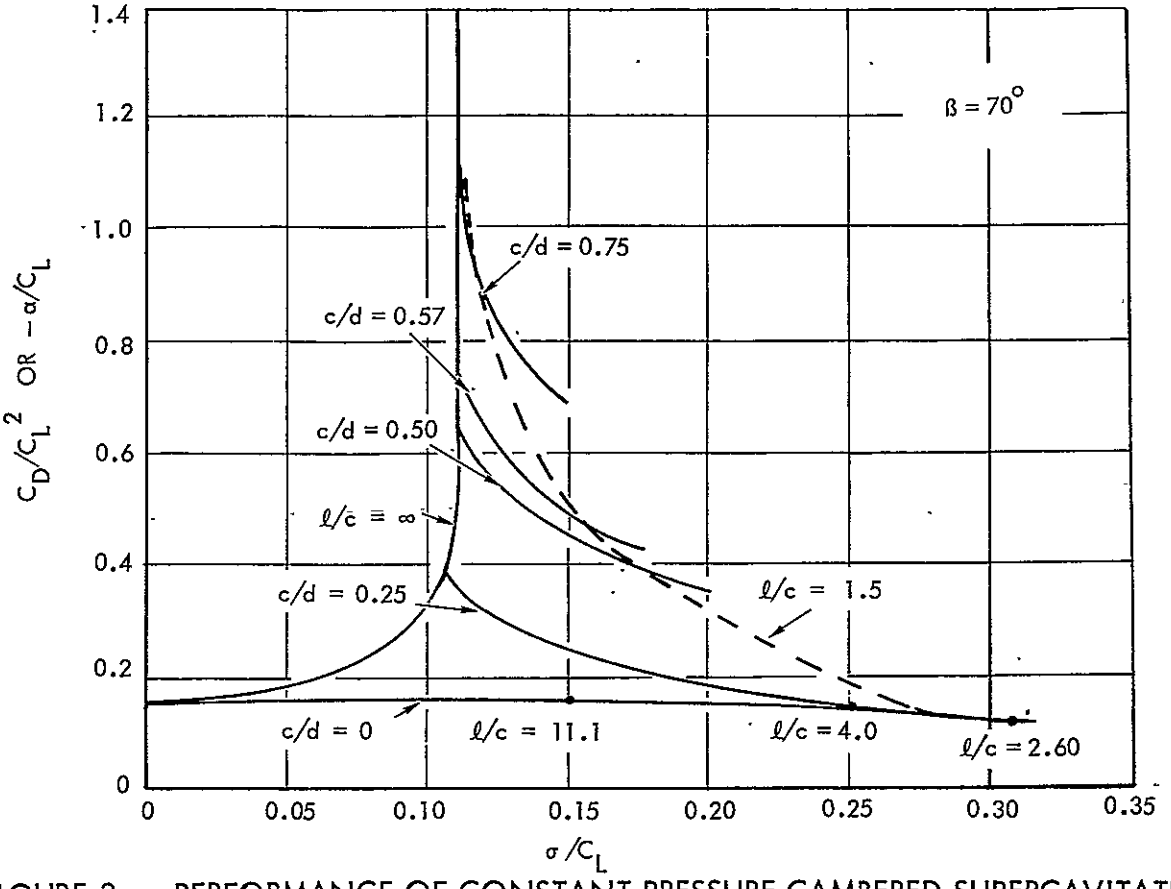

FIGURE 3 - PERFORMANCE OF CONSTANT PRESSURE CAMBERED SUPERCAVITATING CASCADES WITH A STAGGER ANGLE OF 70 DEGREES

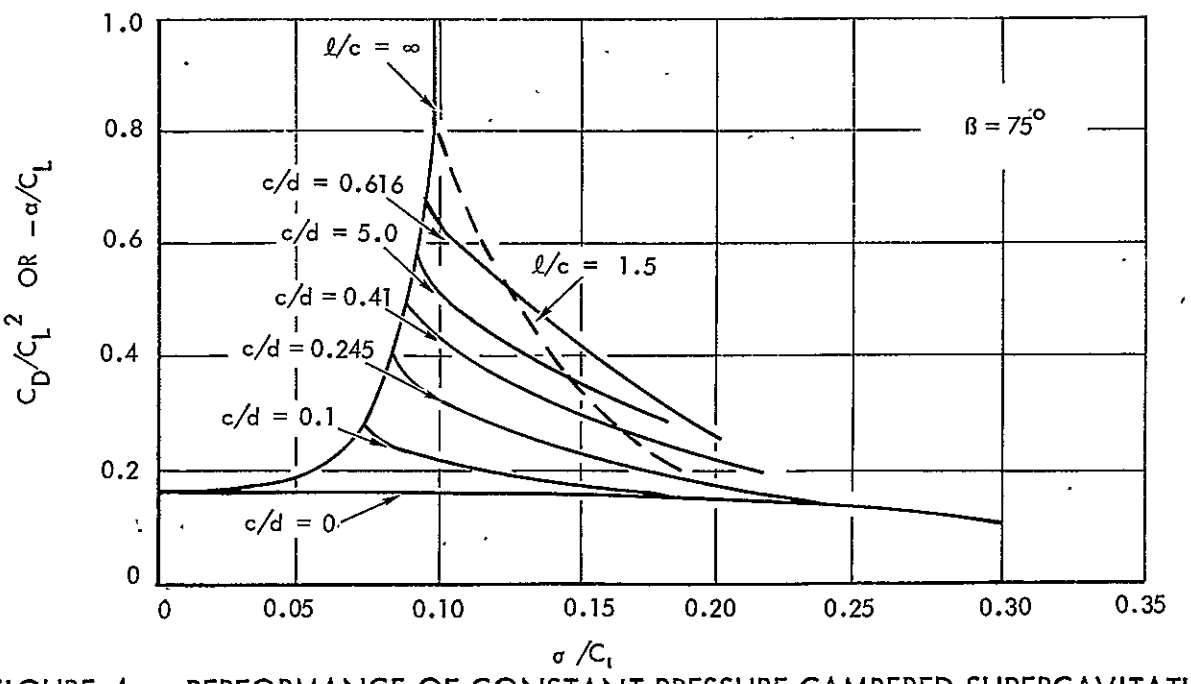

FIGURE 4 - PERFORMANCE OF CONSTANT PRESSURE CAMBERED SUPERCAVITATING CASCADES WITH A STAGGER ANGLE OF 75 DEGREES

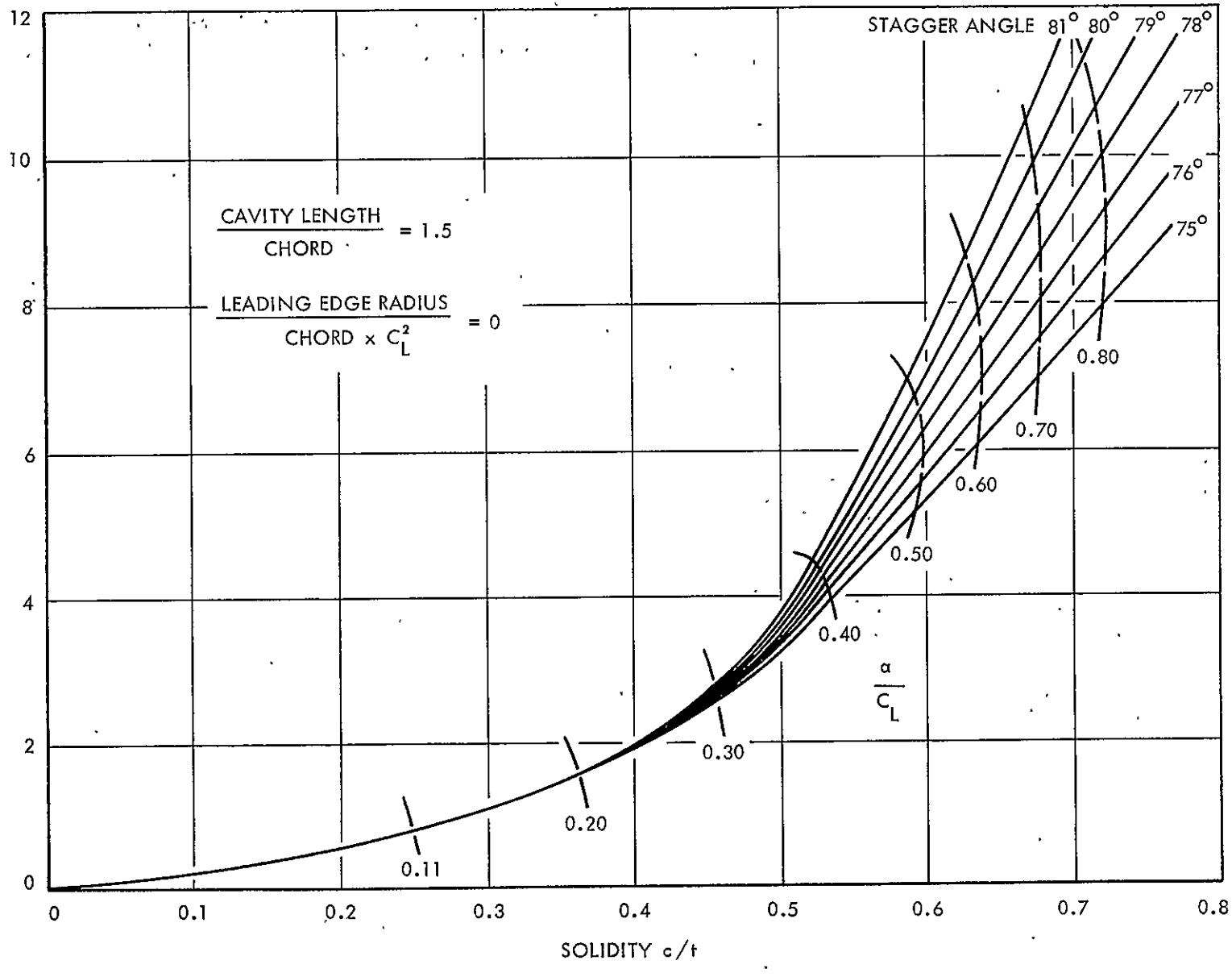

FIGURE 5 - CONSTANT PRESSURE CAMBERED SUPERCAVITATING CASCADE CHARACTERISTICS IN TERMS OF INDUCER REQUIREMENTS

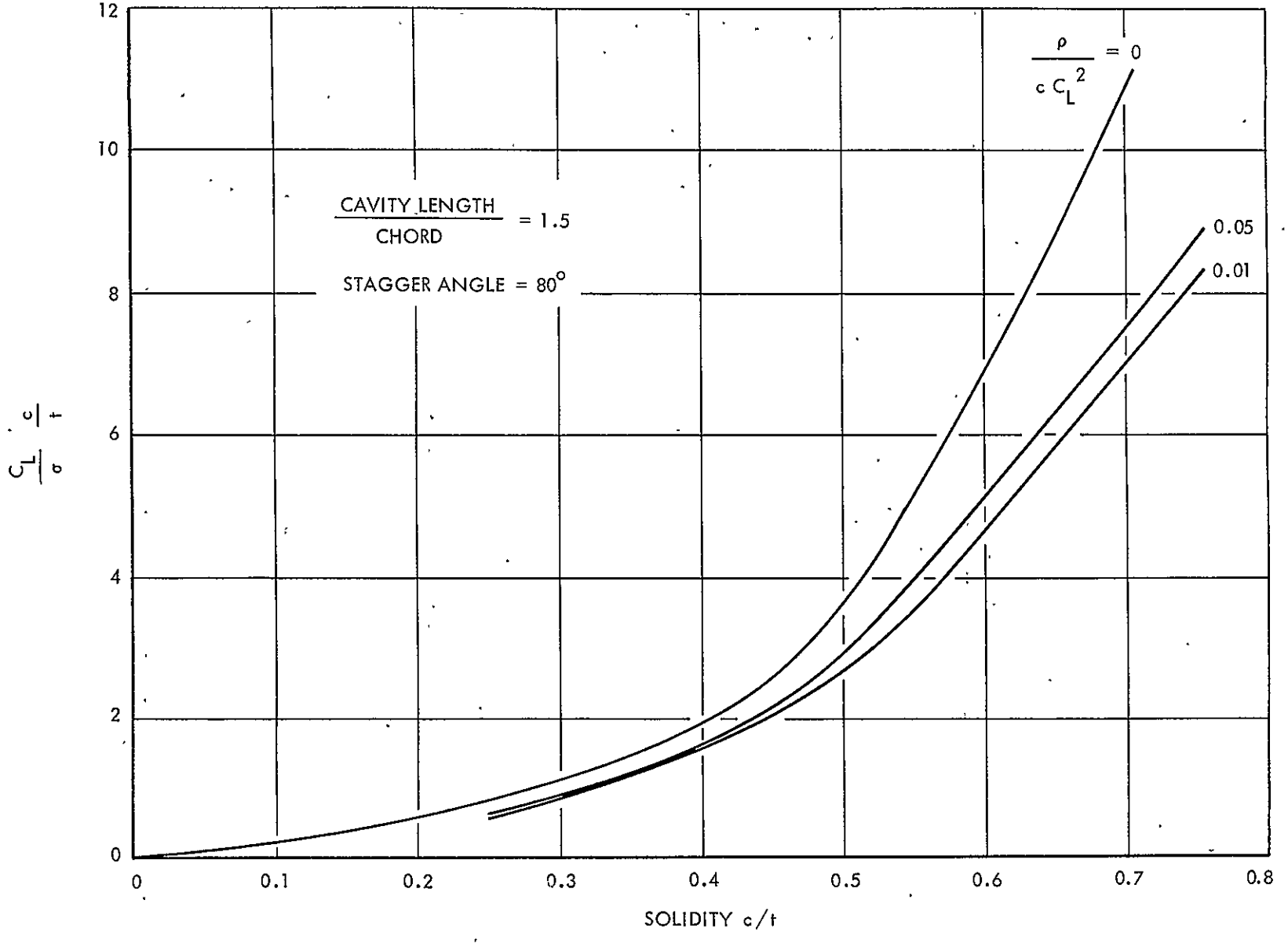

FIGURE 6 - EFFECT OF LEADING EDGE RADIUS ON PERFORMANCE OF CONSTANT PRESSURE CAMBERED SUPERCAVITATING CASCADES.

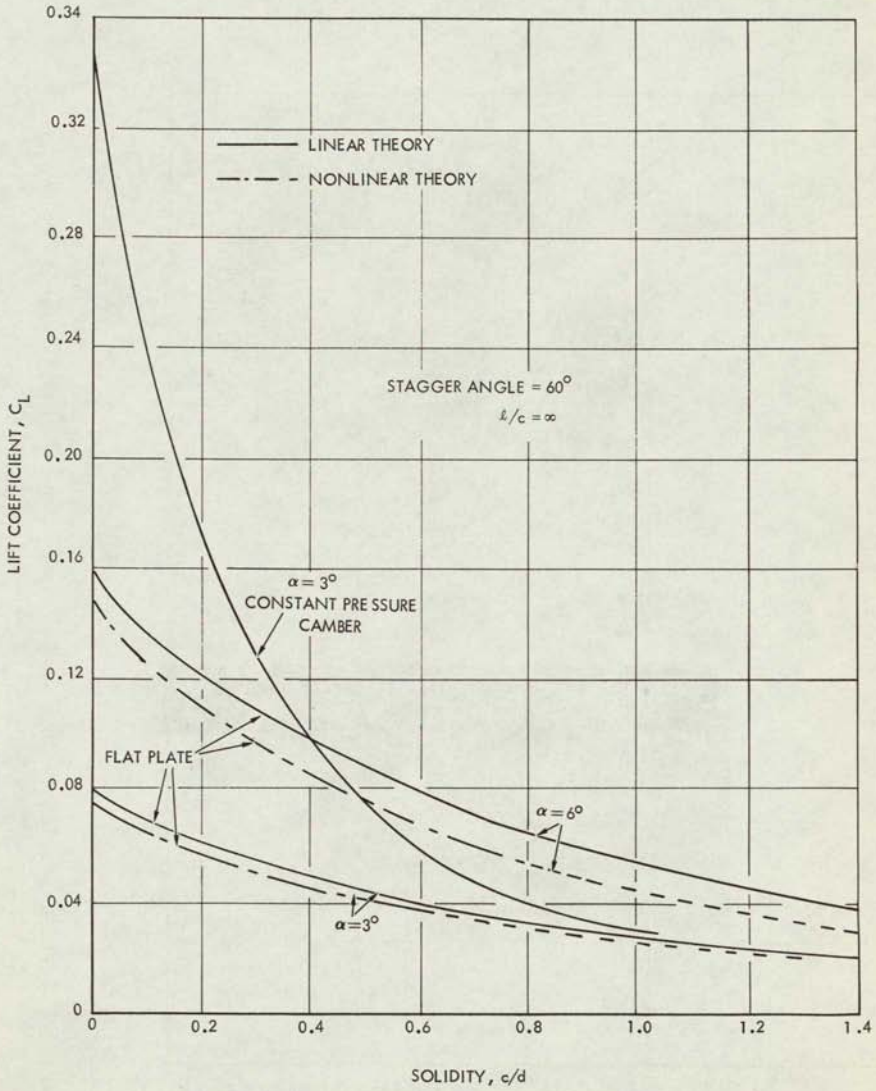

FIGURE 7 - COMPARISON OF CONSTANT PRESSURE CAMBERED AND FLAT PLATE CASCADES

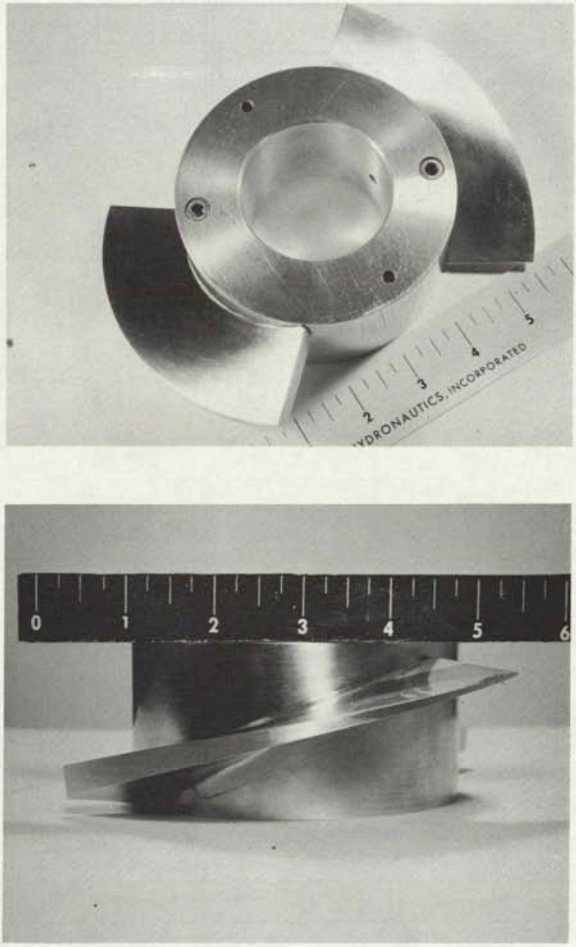

FIGURE 8 - FIRST STAGE OF TANDEM ROW INDUCER NO. 1; 2 BLADES (c/d = 0.540).

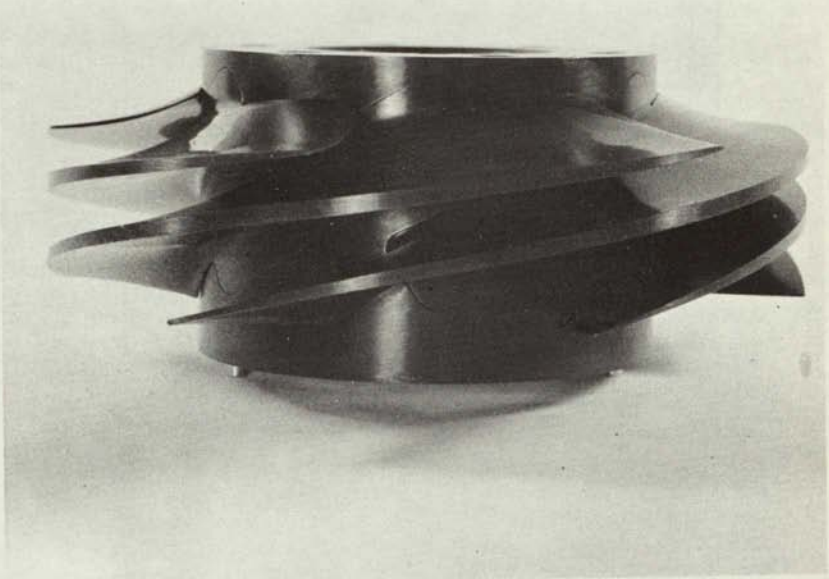

FIGURE 9 - SECOND STAGE OF TANDEM ROW INDUCER NO. 1;
6 BLADES ($c/d = 2.43$).

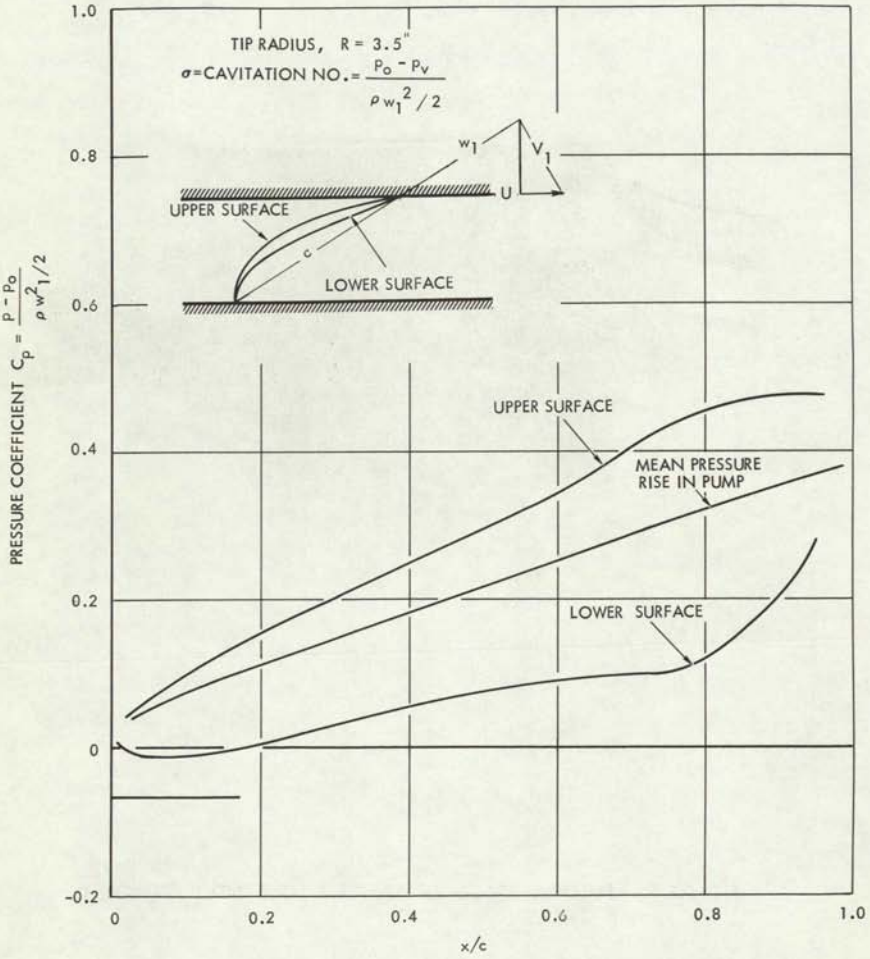

FIGURE10- THEORETICAL PRESSURE DISTRIBUTION ALONG TIP SECTION IN SECOND STAGE OF INDUCER NUMBER 1

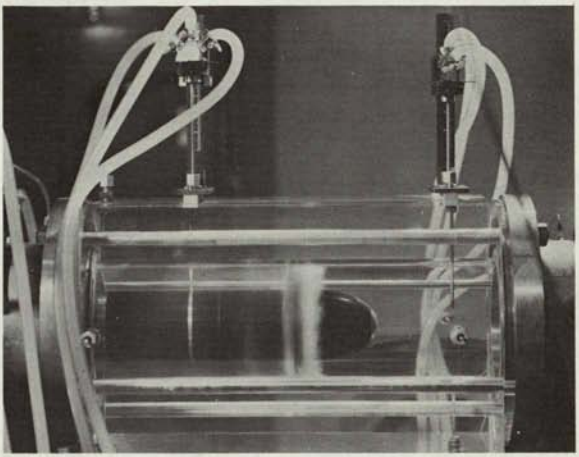

FIGURE 11a - TEST SECTION OF HYDRONAUTICS, INCORPORATED PUMP LOOP

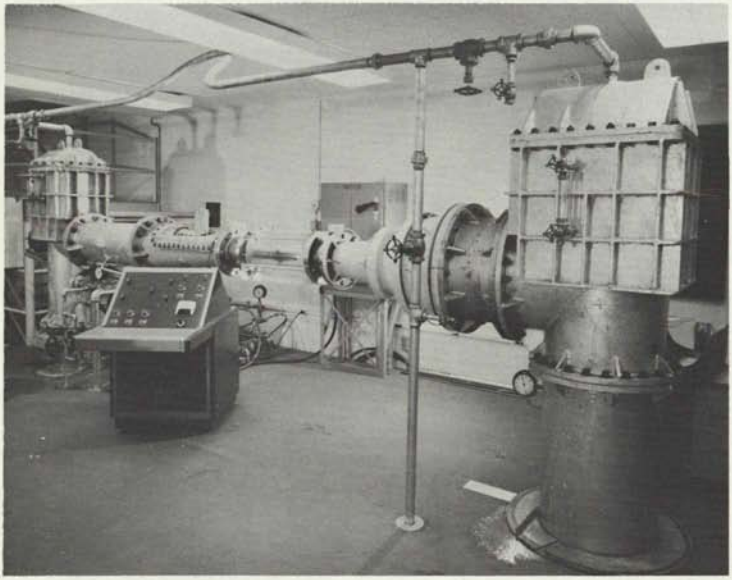

FIGURE 11b - OVERALL VIEW OF HYDRONAUTICS, INCORPORATED PUMP LOOP

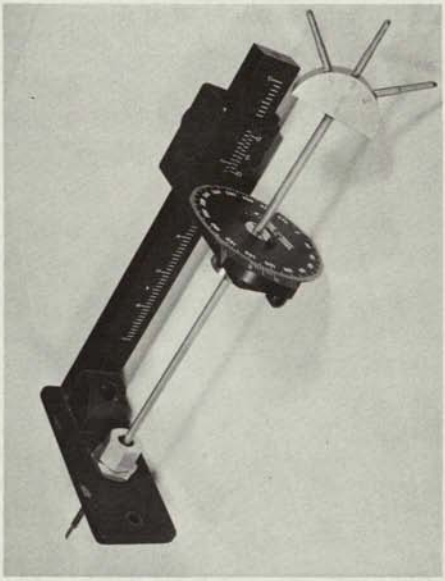

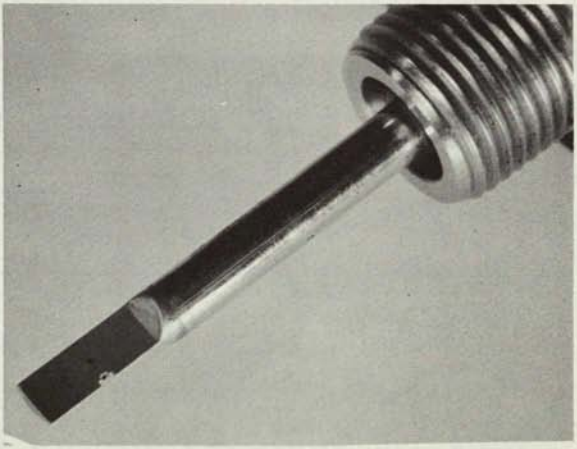

FIGURE 12 - YAW HEAD PROBE AND TRAVERSE STAND.

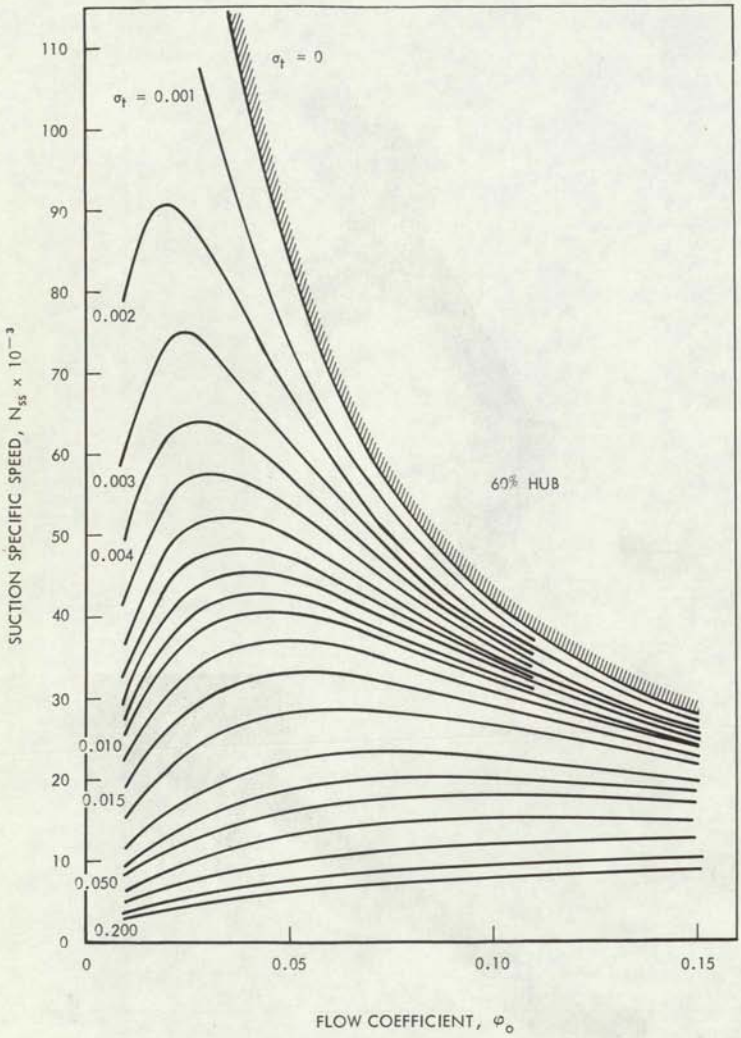

FIGURE 13 - INFLUENCE OF FLOW COEFFICIENT ON RELATIONSHIP BETWEEN SUCTION SPECIFIC SPEED AND TIP CAVITATION NUMBER FOR A 0.60 HUB / DIAMETER RATIO

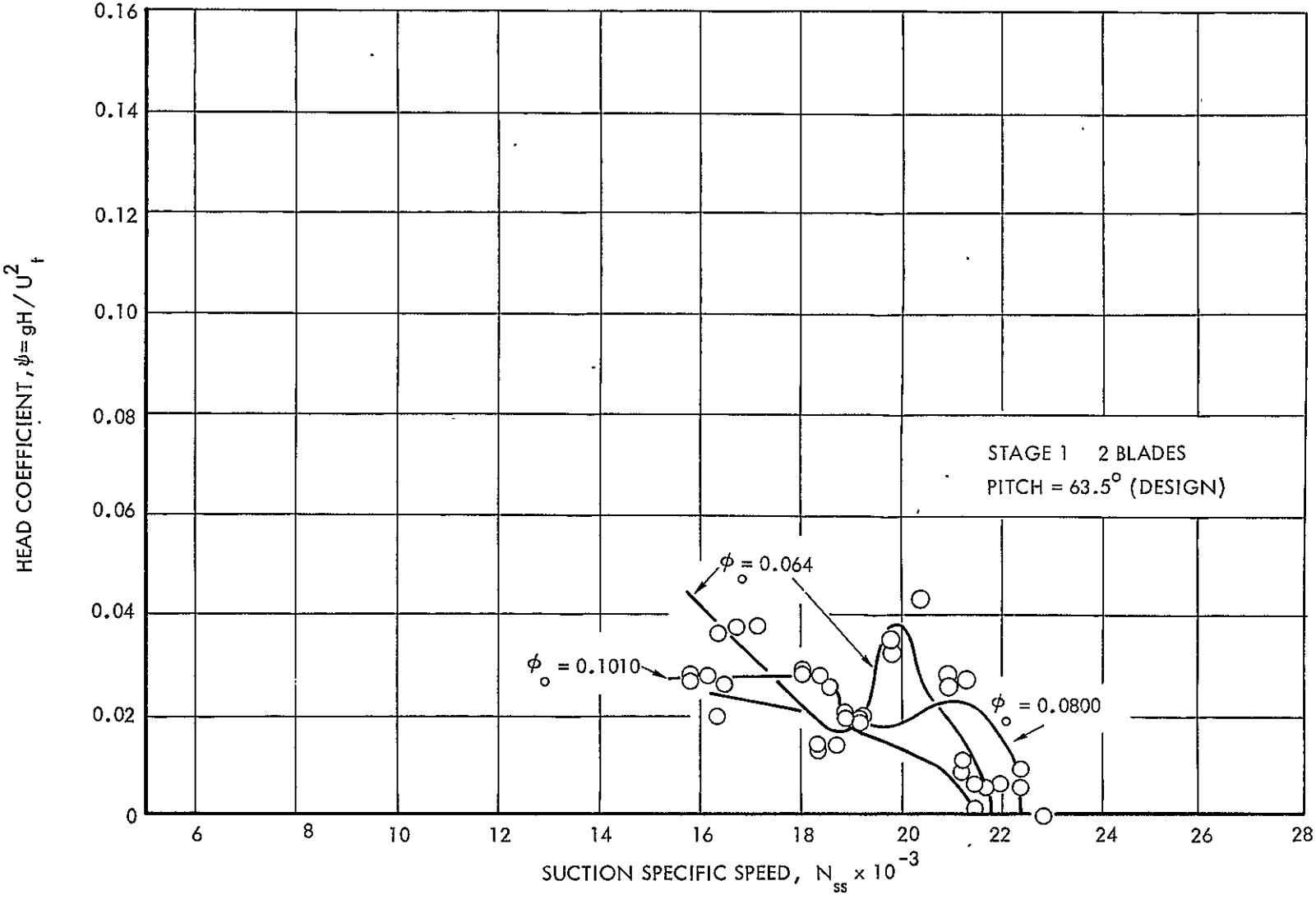

FIGURE 14a - INFLUENCE OF SUCTION SPECIFIC SPEED ON THE PERFORMANCE OF STAGE 1, INDUCER NO. 1 WITH 2 BLADES AT A PITCH OF 63.5° (DESIGN PITCH)

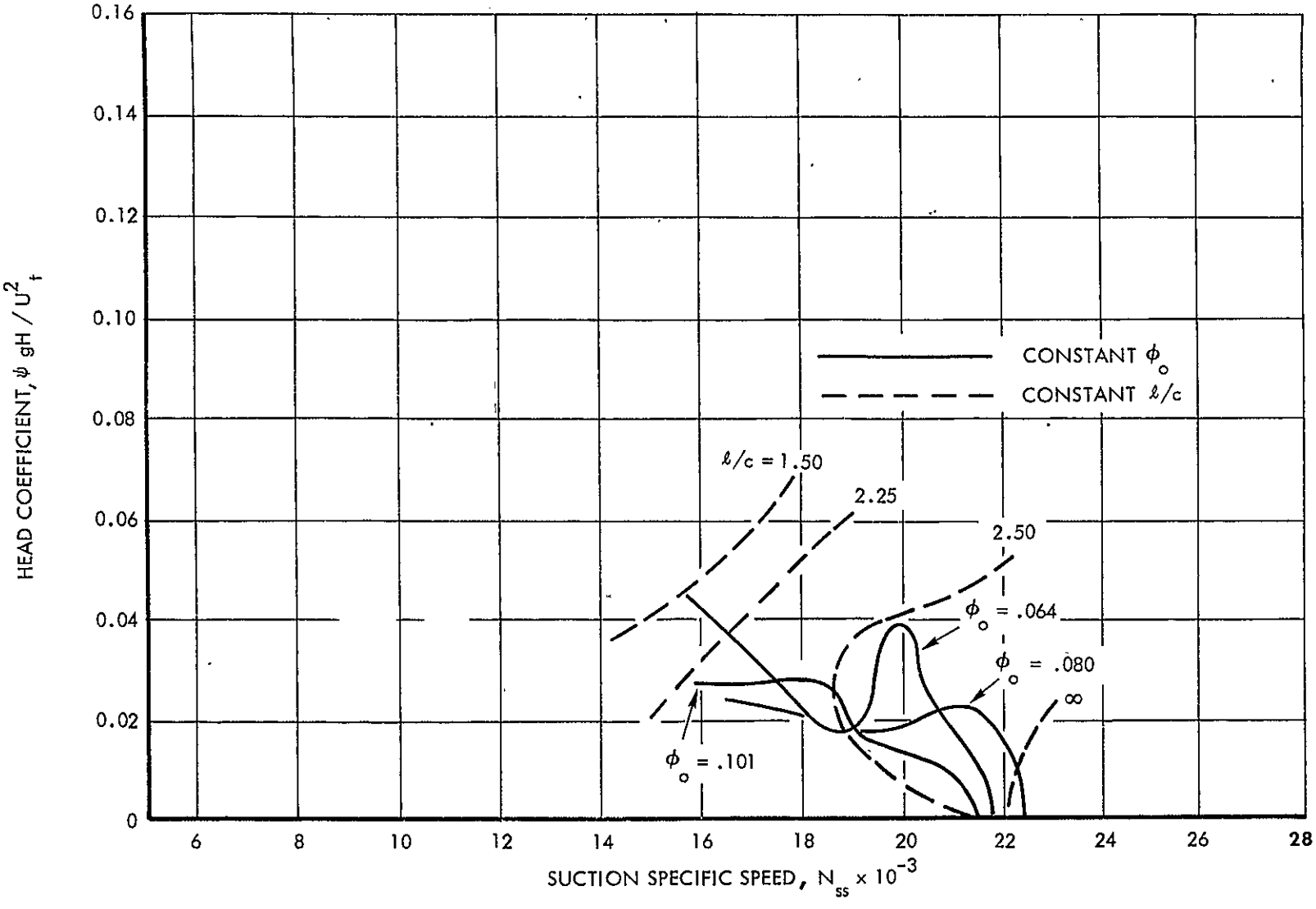

FIGURE 14b - INFLUENCE OF SUCTION SPECIFIC SPEED AND FLOW COEFFICIENT ON CAVITY LENGTH FOR STAGE 1, INDUCER NO. 1

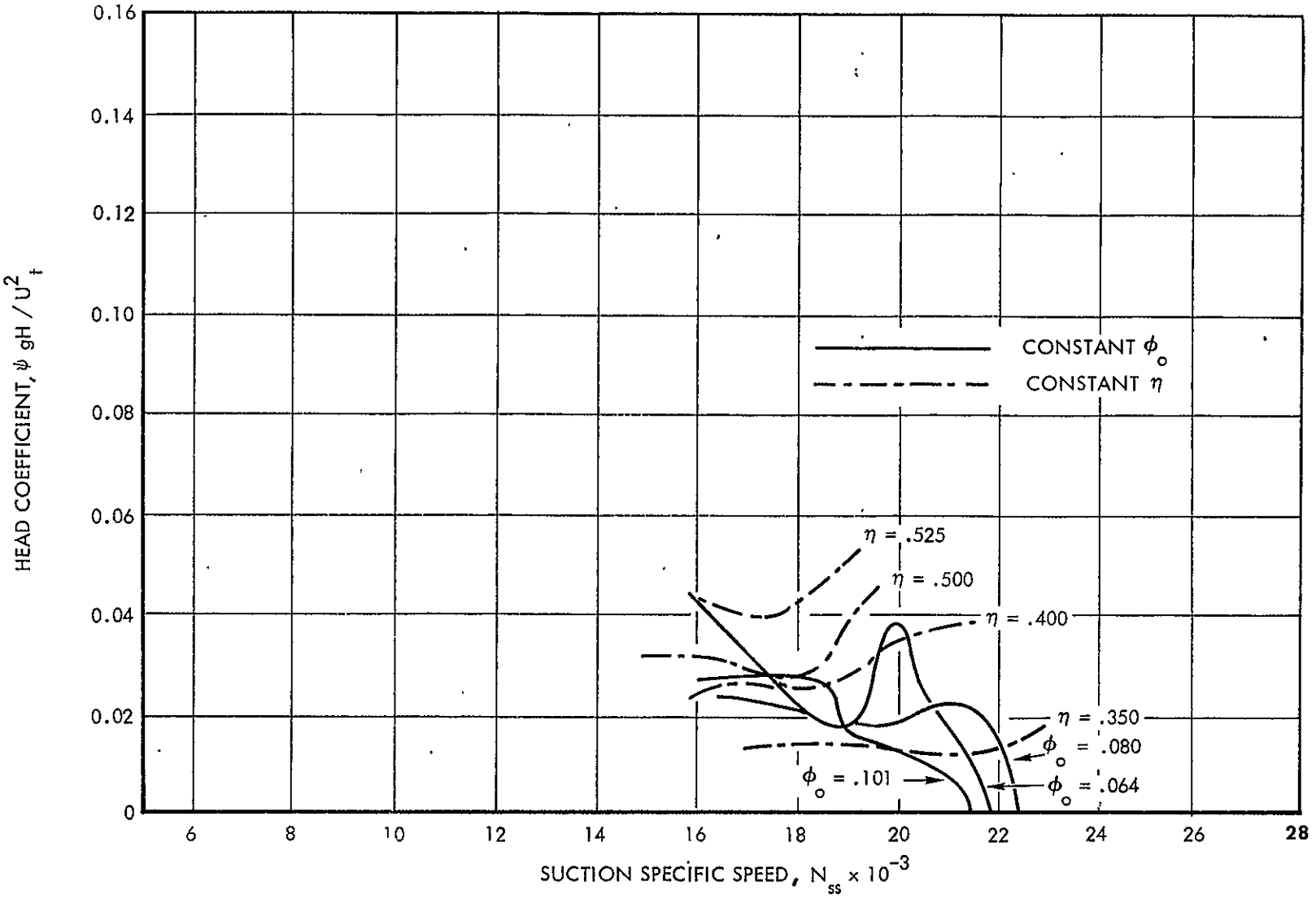

FIGURE 14c - INFLUENCE OF SUCTION SPECIFIC SPEED AND FLOW COEFFICIENT ON EFFICIENCY FOR STAGE 1, INDUCER NO. 1

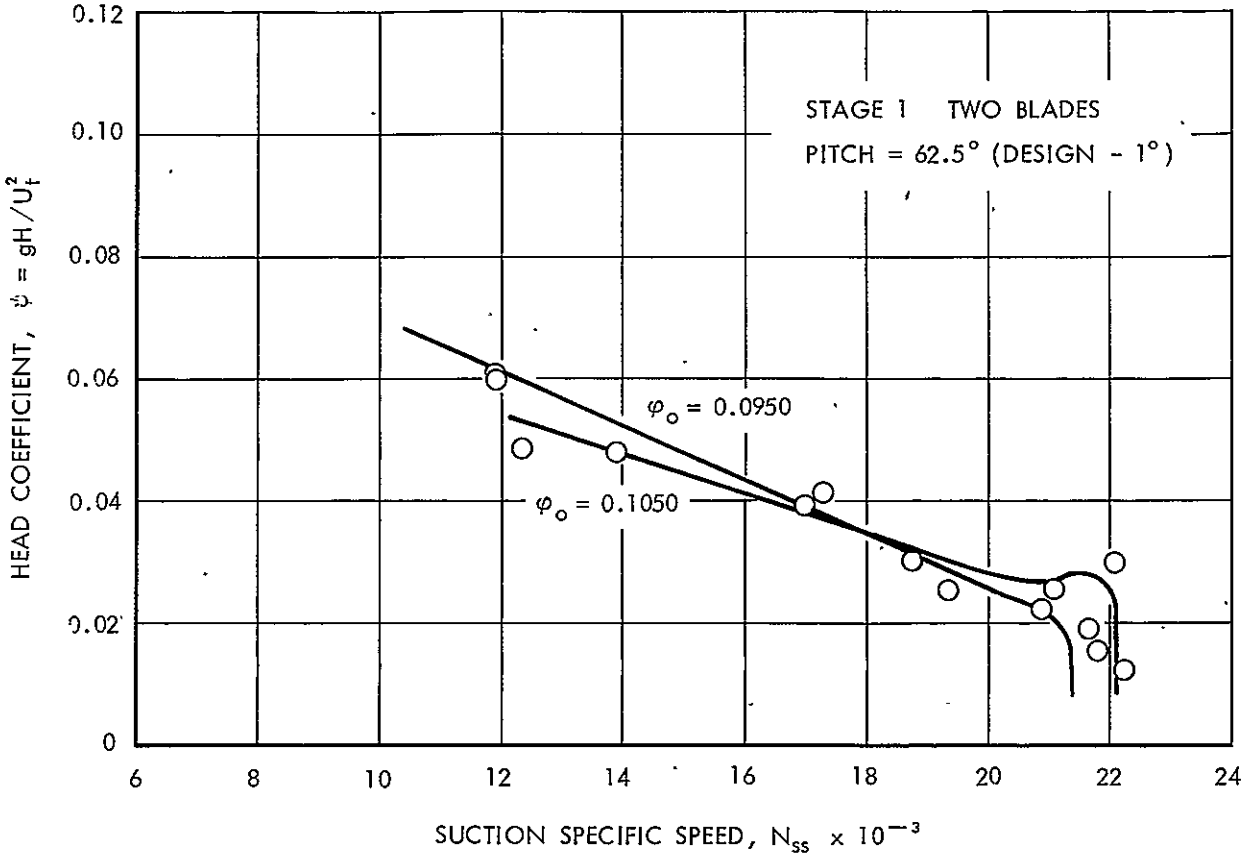

FIGURE 15 - INFLUENCE OF SUCTION SPECIFIC SPEED ON THE PERFORMANCE OF STAGE 1, INDUCER NO. 1 WITH TWO BLADES AT A PITCH OF 62.5° (DESIGN PITCH - 1°)

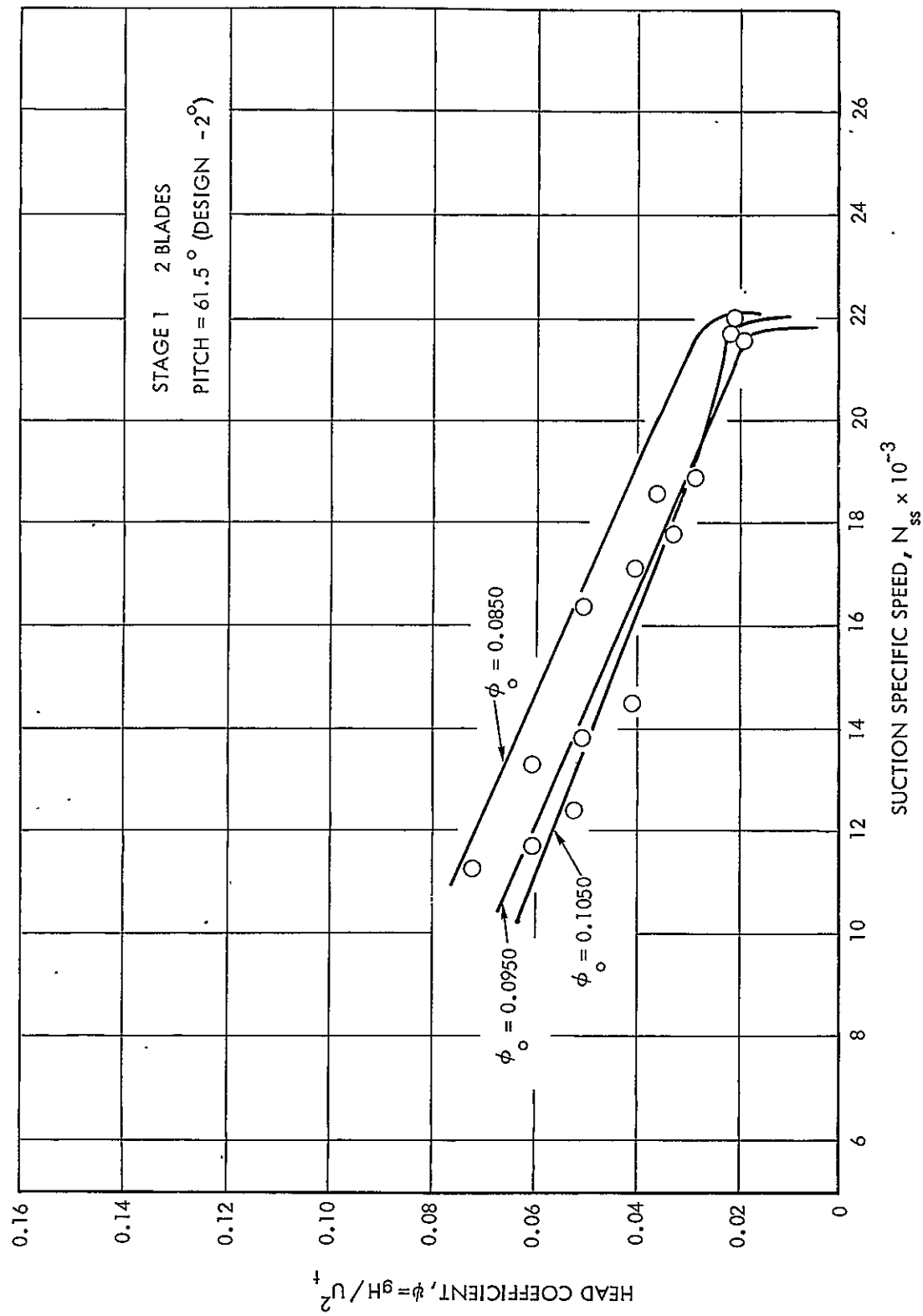

FIGURE 16 - INFLUENCE OF SUCTION SPECIFIC SPEED ON THE PERFORMANCE OF STAGE 1, INDUCER NO. 1 WITH 2 BLADES AT A PITCH OF 61.5° (DESIGN PITCH -2°)

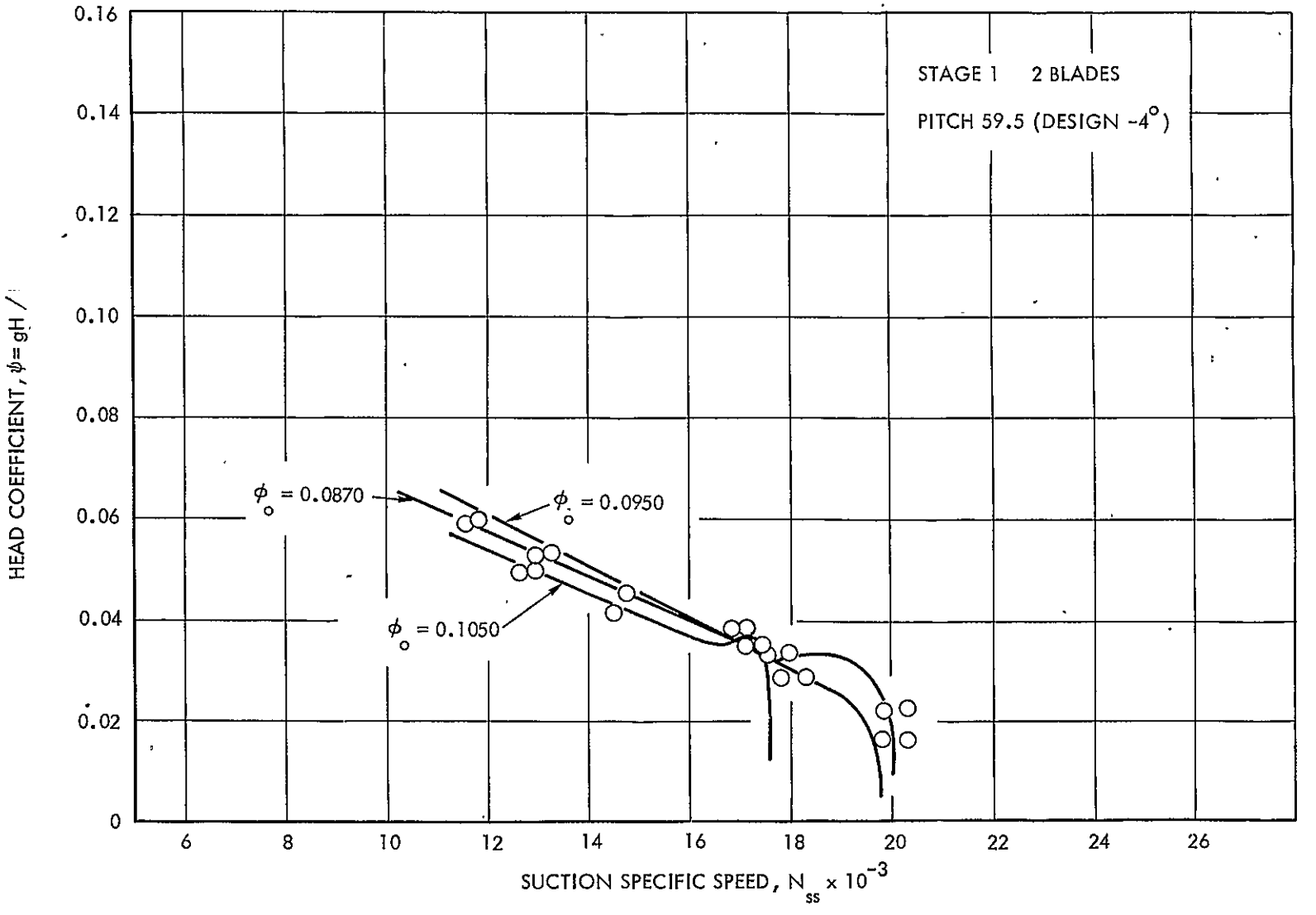

FIGURE 17- INFLUENCE OF SUCTION SPECIFIC SPEED ON THE PERFORMANCE OF STAGE 1, INDUCER NO. 1 WITH 2 BLADES AT A PITCH OF 59.5° (DESIGN PITCH -4°)

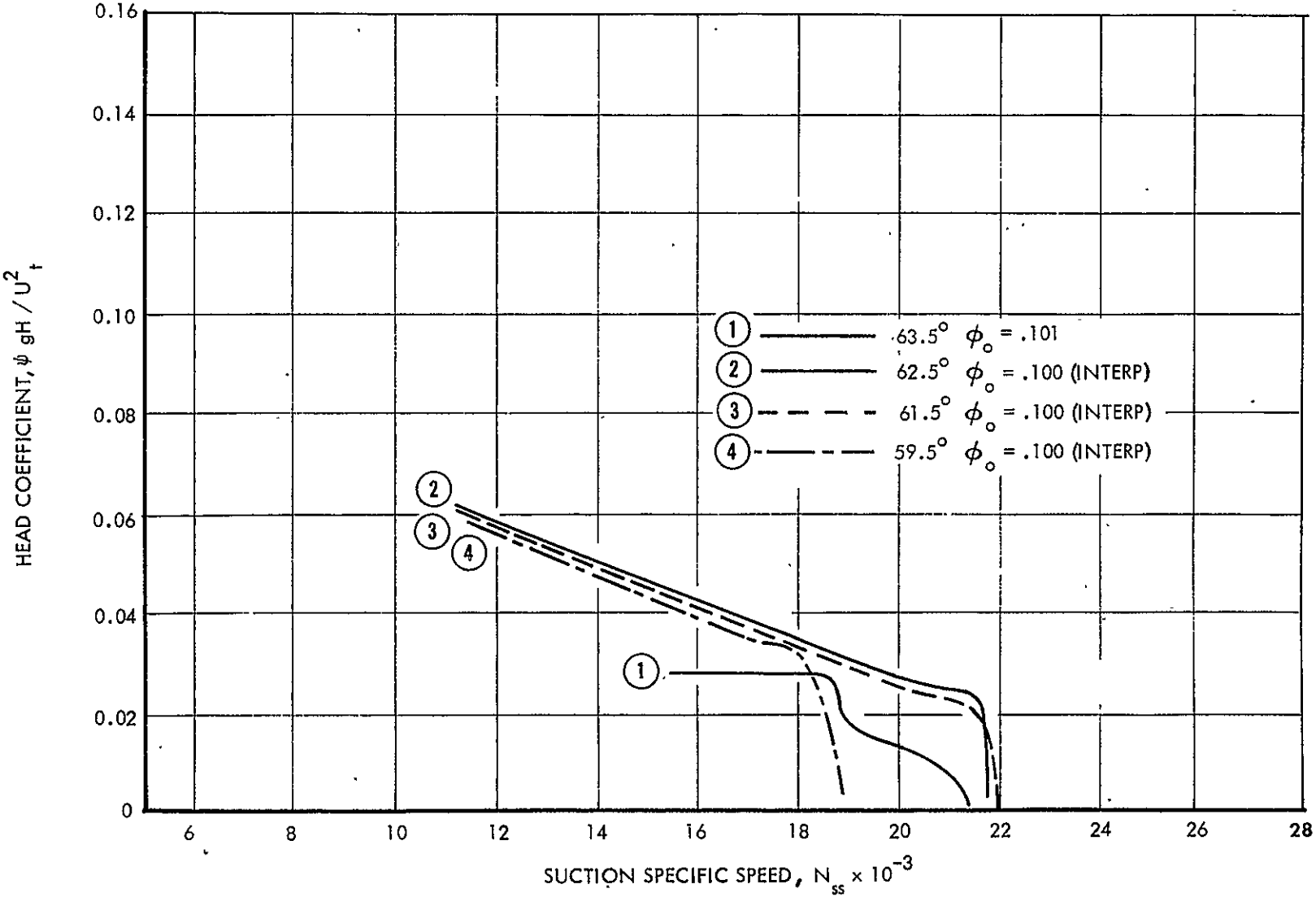

FIGURE 18 - COMPARATIVE PERFORMANCE OF STAGE 1, INDUCER NO. 1 AT DESIGN FLOW COEFFICIENT (. 10) WITH VARIOUS PITCH SETTINGS

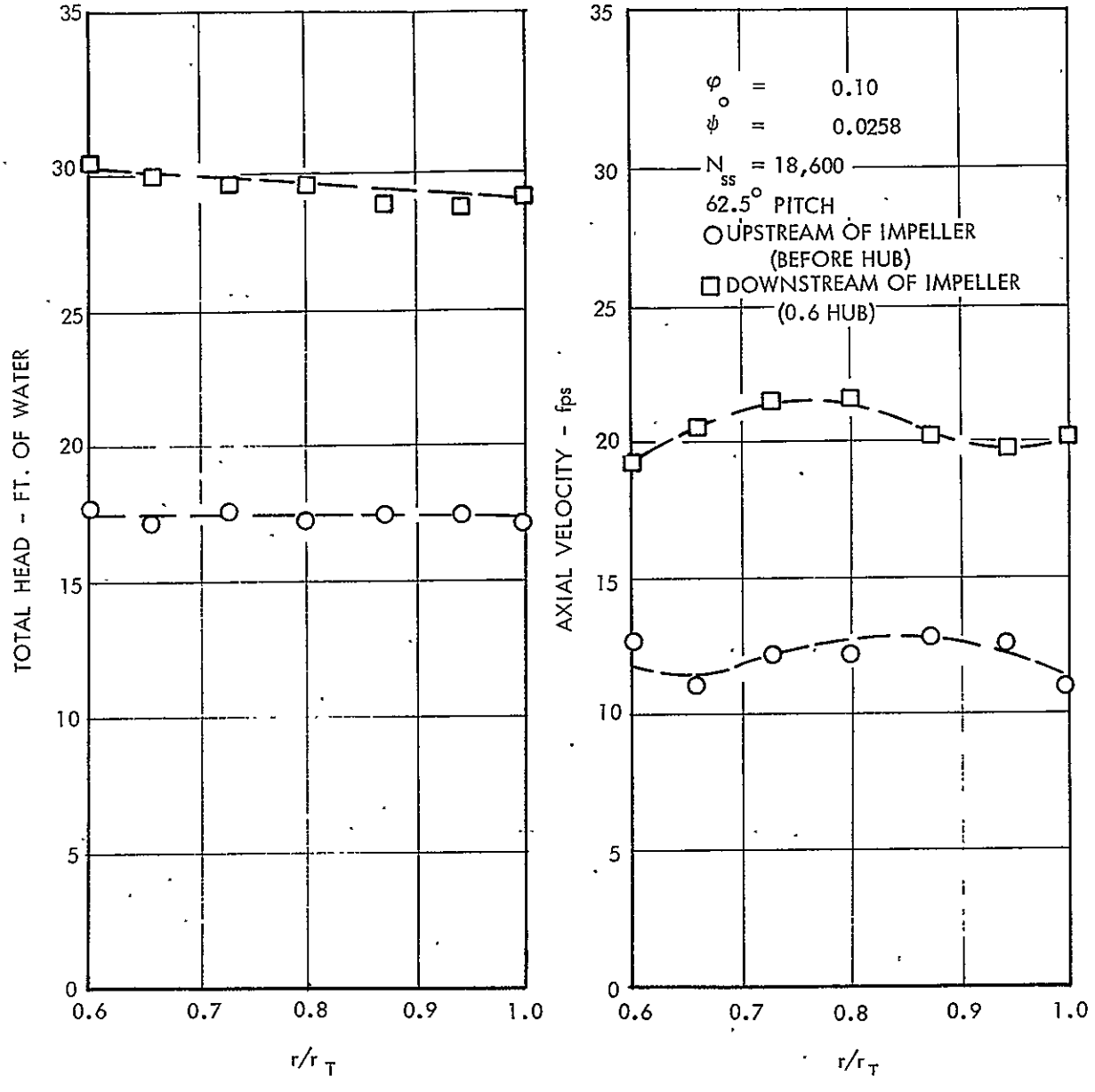

FIGURE 19 - RADIAL DISTRIBUTION OF TOTAL HEAD AND AXIAL VELOCITY DURING A TYPICAL TEST ON THE FIRST STAGE OF INDUCER NO. 1

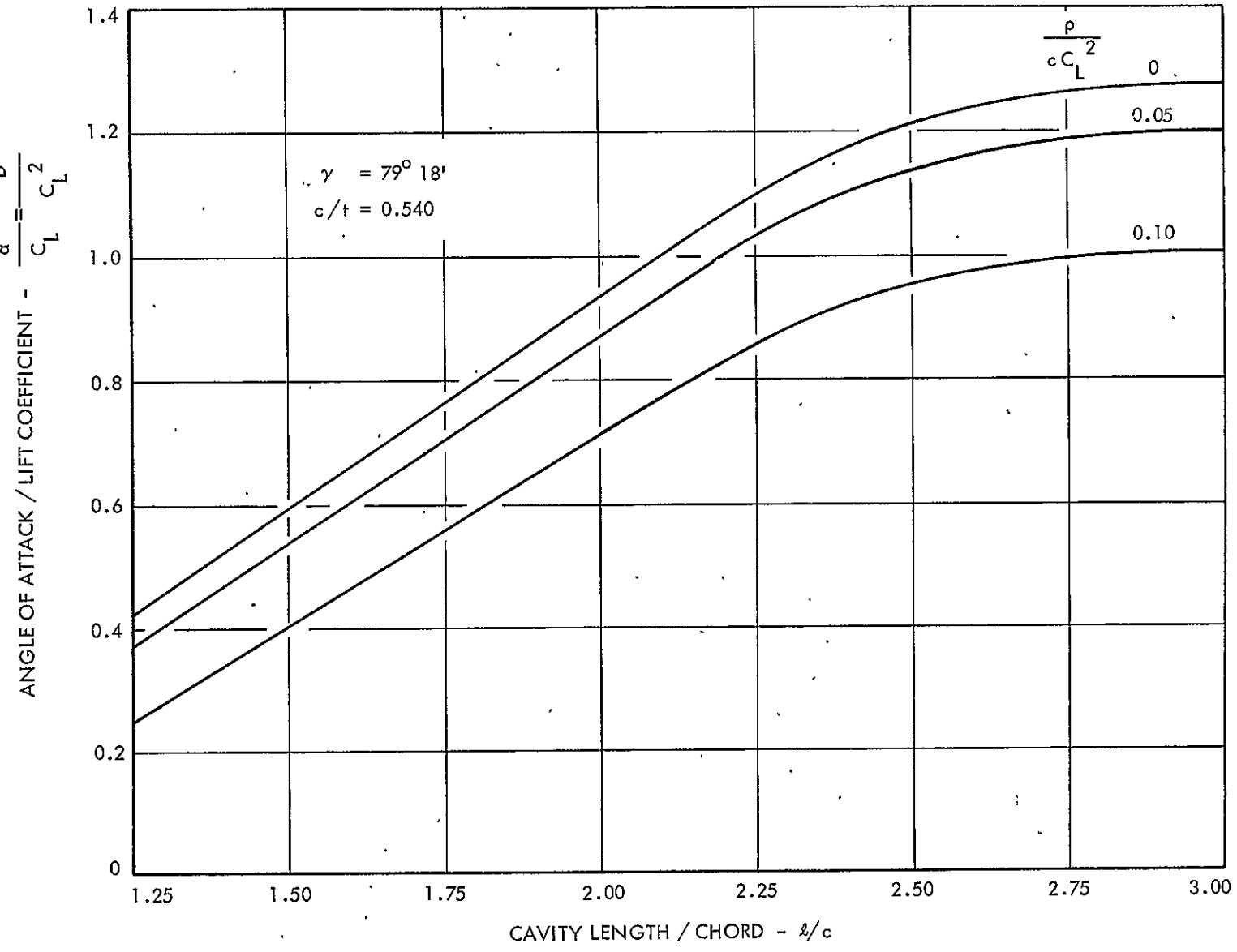

FIGURE 20 - THEORETICAL VARIATION OF REQUIRED ANGLE OF ATTACK WITH CAVITY LENGTH FOR CONSTANT PRESSURE CAMBERED SUPERCAVITATING CASCADES (11)

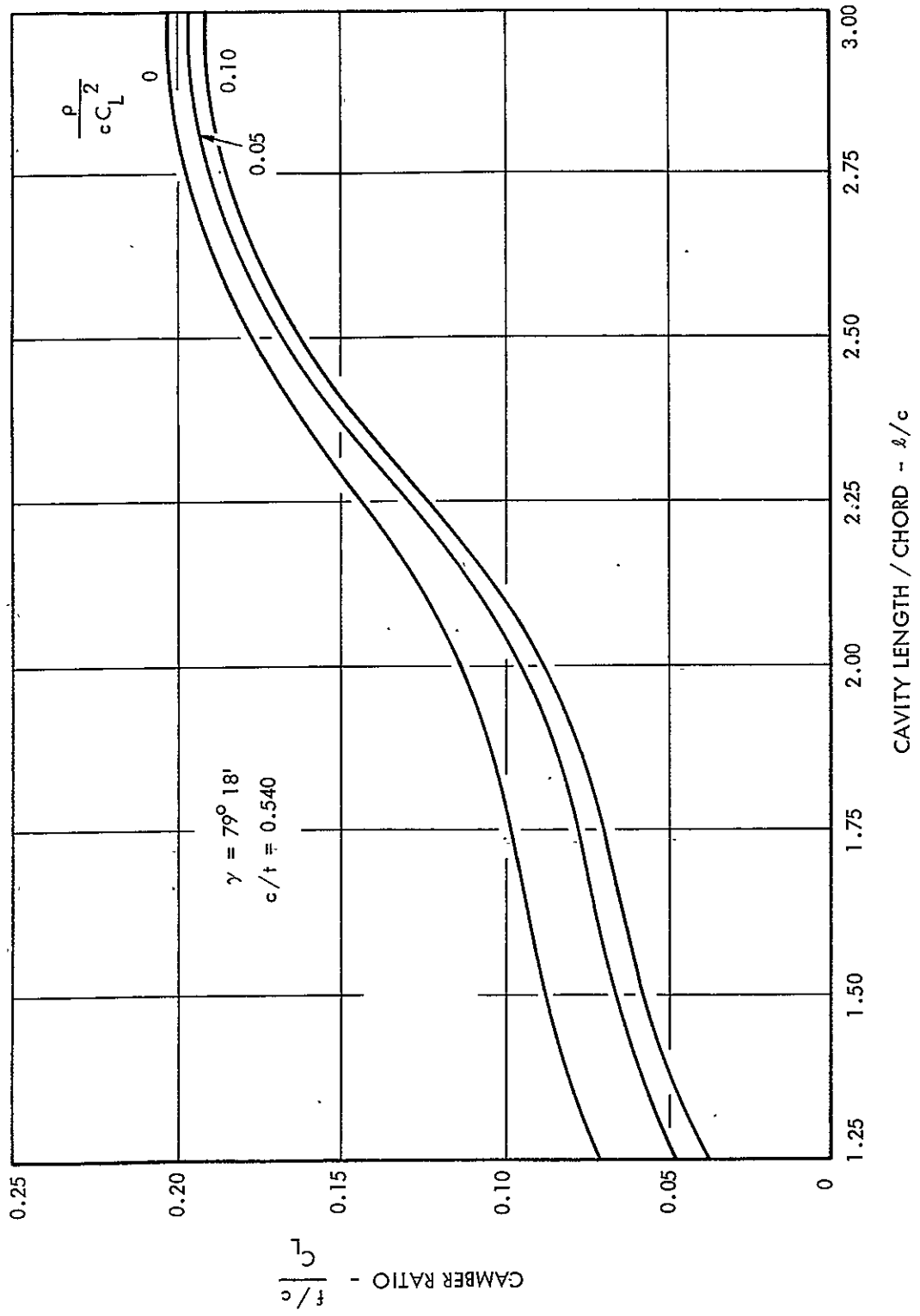

FIGURE 21 - THEORETICAL VARIATION OF CAMBER WITH CAVITY LENGTH FOR CONSTANT PRESSURE CAMBERED SUPERCAVITATING CASCADES (11)

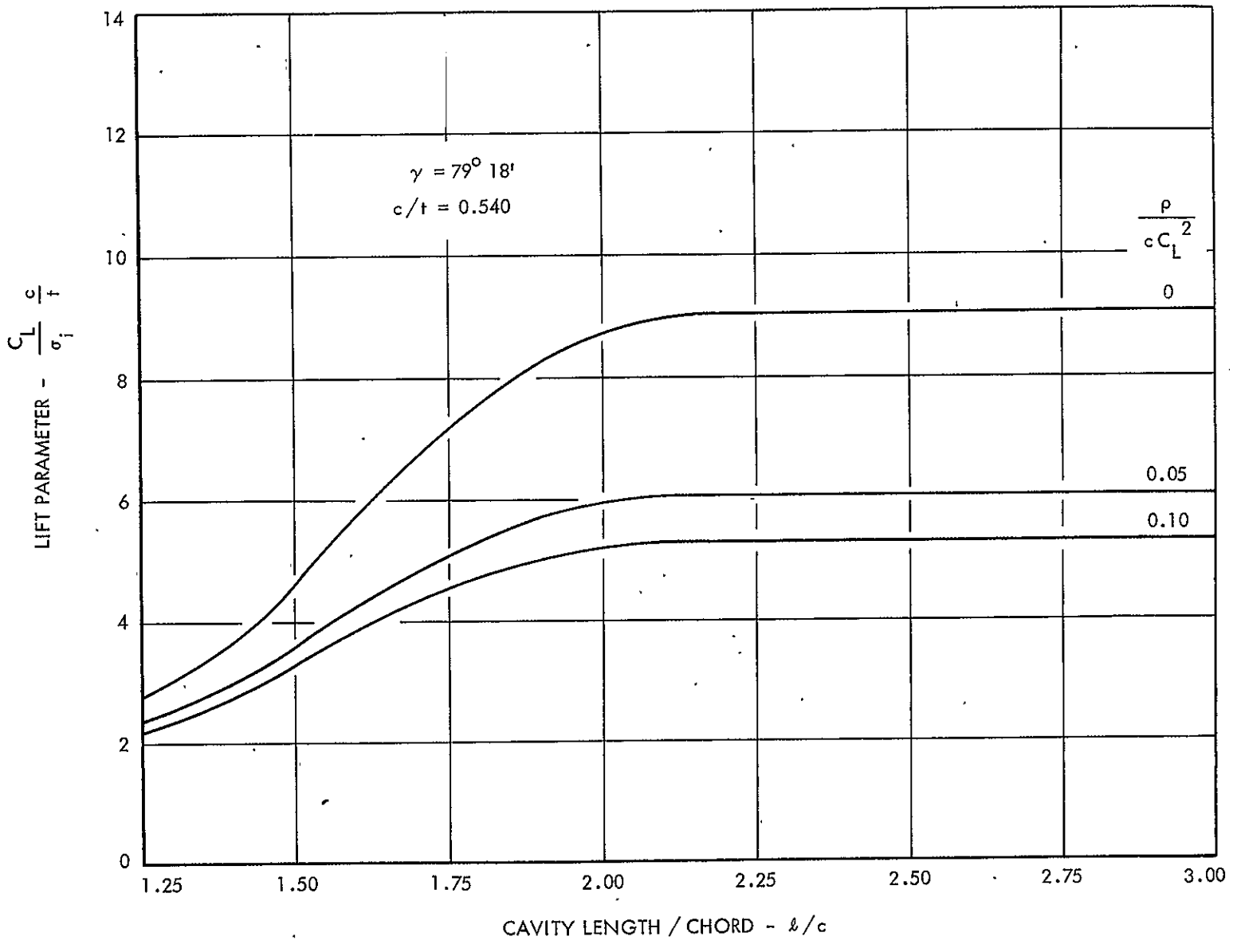

FIGURE 22 - THEORETICAL VARIATION OF LIFT PARAMETER WITH CAVITY LENGTH FOR CONSTANT PRESSURE CAMBERED SUPERCAVITATING CASCADES (11)

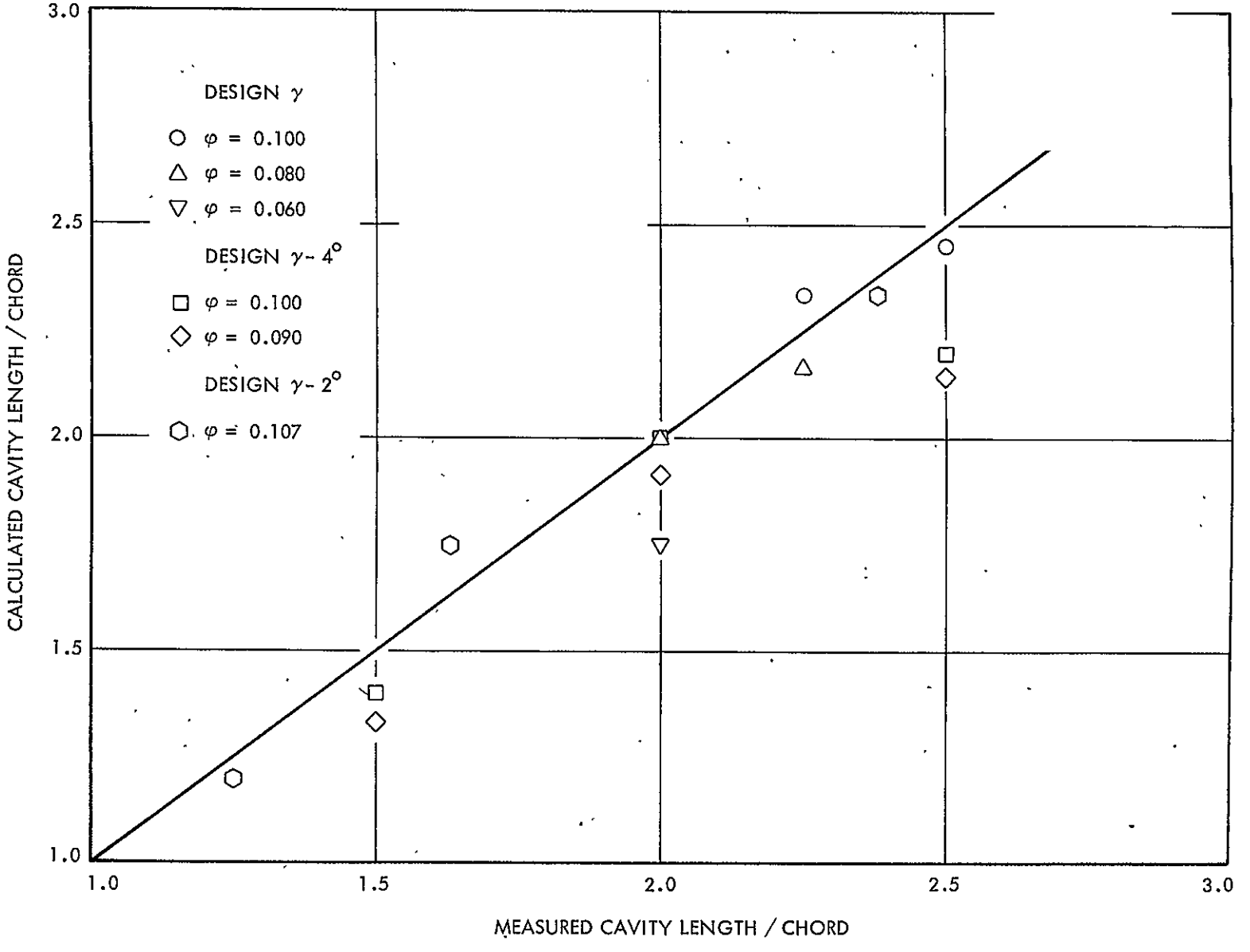

FIGURE 23 - COMPARISON OF MEASURED AND THEORETICAL CAVITY LENGTHS AT THE SAME VALUE OF C_L AND DESIGN CAMBER (CAVITATION NUMBER, σ , NOT CONSIDERED)

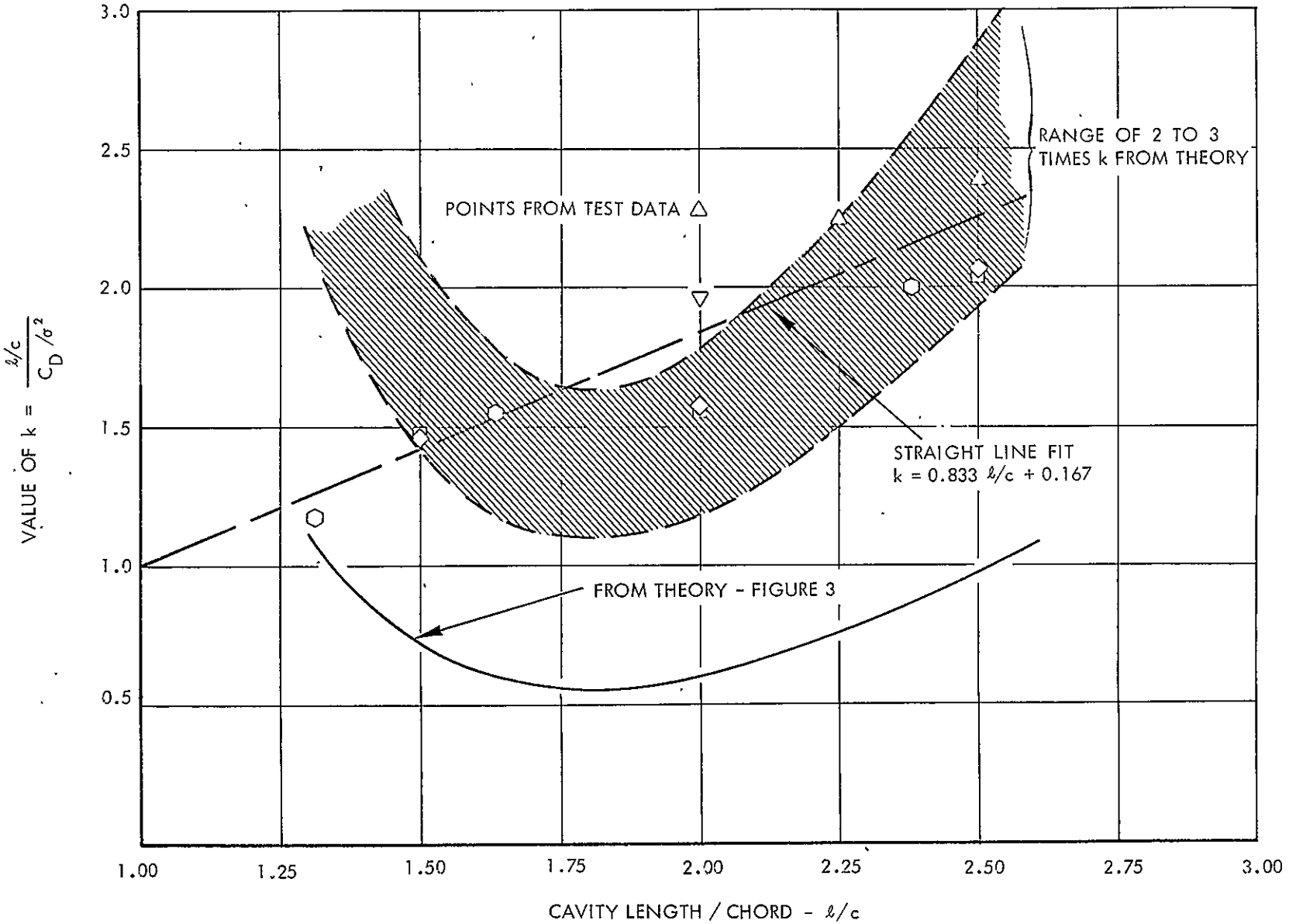

FIGURE 24 - THEORETICAL AND EXPERIMENTAL VALUES OF CONSTANT, k, FOR RELATIONSHIP BETWEEN CAVITY LENGTH AND DRAG PARAMETER

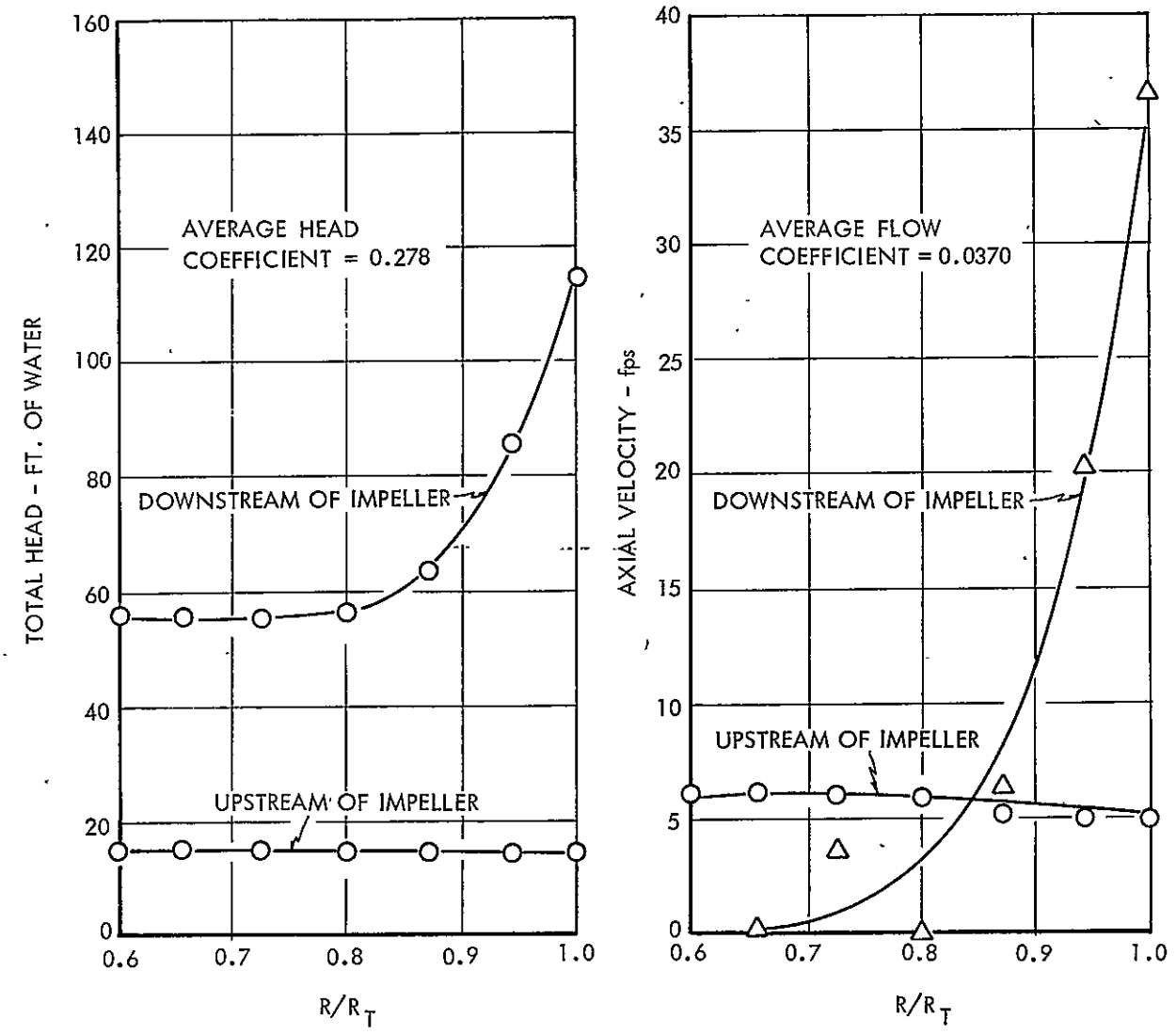

FIGURE 25 - RADIAL DISTRIBUTION OF HEAD AND FLOW COEFFICIENTS FOR SECOND STAGE; INDUCER NO. 1, TEST RUN NO. 3

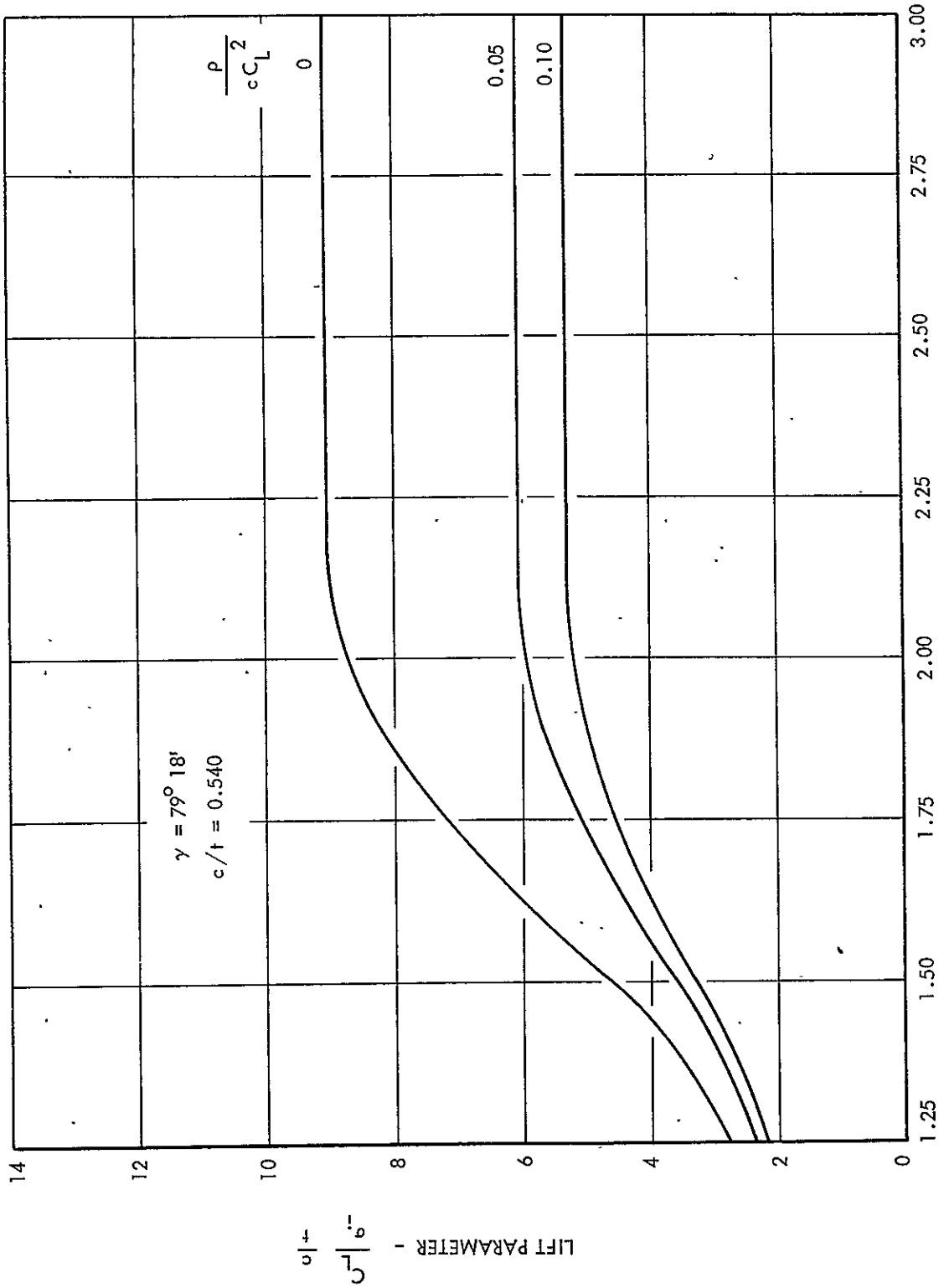

FIGURE 22 - THEORETICAL VARIATION OF LIFT PARAMETER WITH CAVITY LENGTH FOR CONSTANT PRESSURE CAMBERED SUPERCAVITATING CASCADES (11)

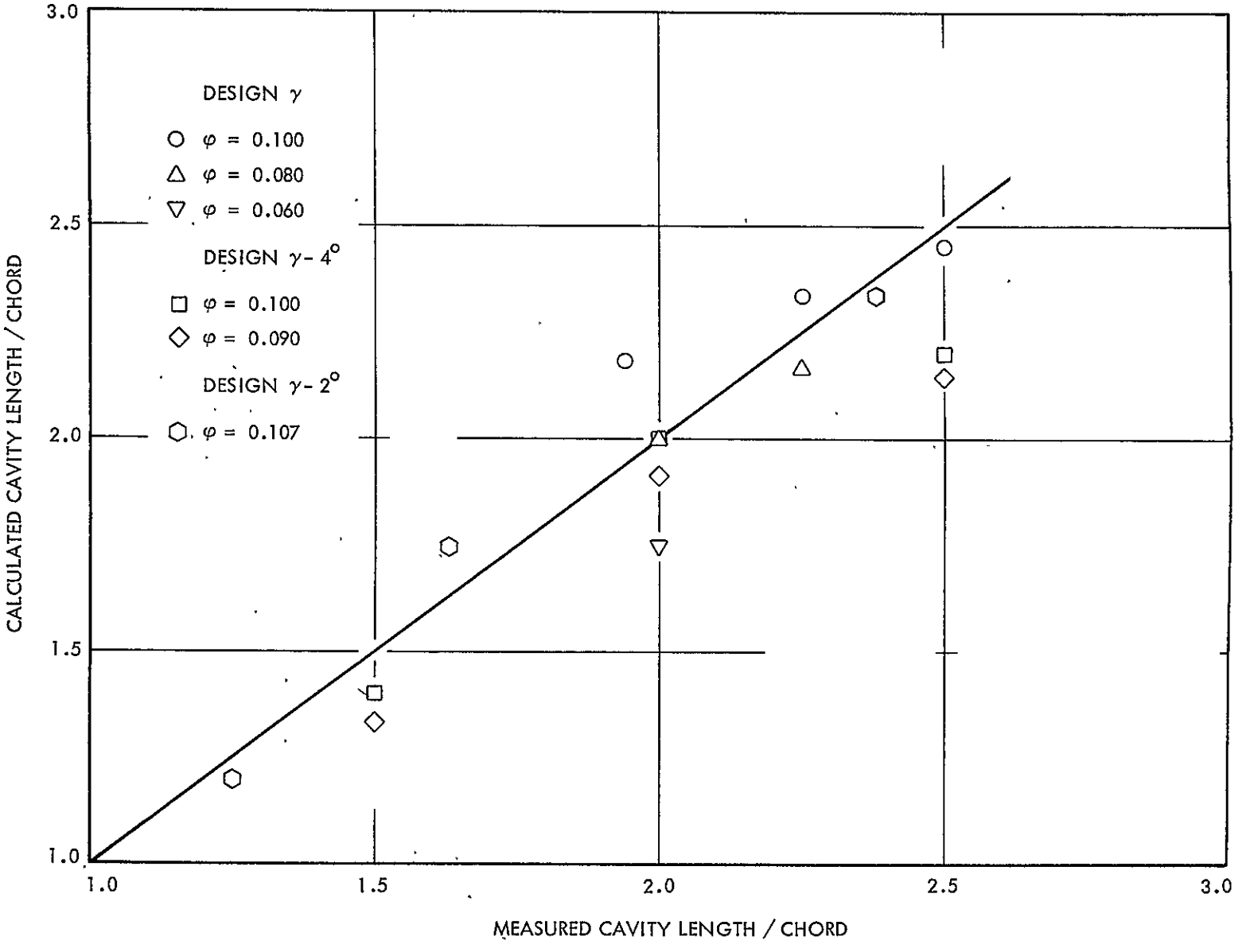

FIGURE 23 - COMPARISON OF MEASURED AND THEORETICAL CAVITY LENGTHS AT THE SAME VALUE OF C_L AND DESIGN CAMBER (CAVITATION NUMBER, σ , NOT CONSIDERED)

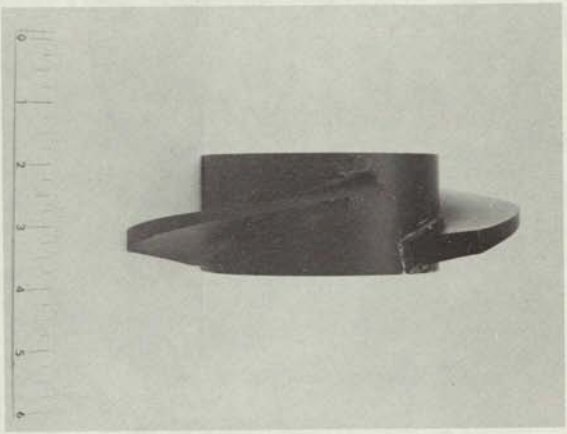

FIGURE 26 - STAGE 1 OF INDUCER NO. 2; 3 BLADES (c/d = 0.810) TESTED WITH PITCH = 67.5° AND 63.5°.

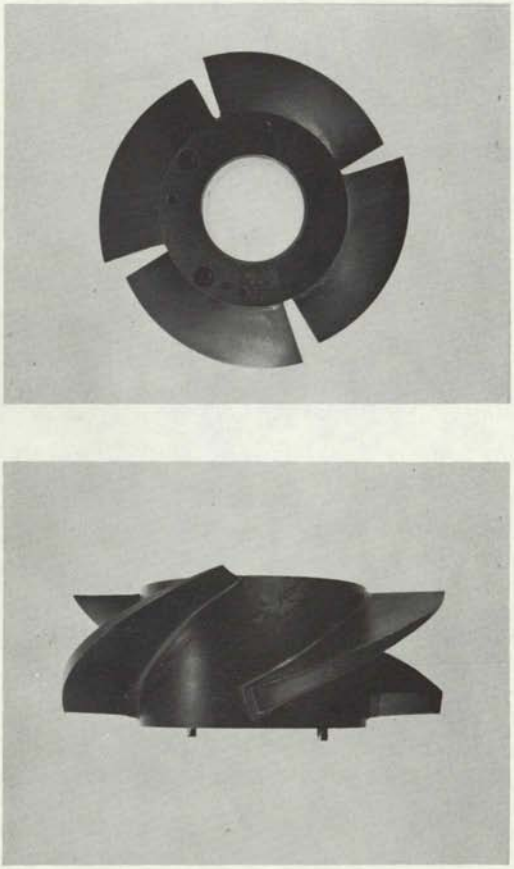

FIGURE 27 - STAGE 1 OF INDUCER NO. 3; 4 BLADES (c/d = 1.080) TESTED WITH PITCH = 48.5°AND 53.5°.

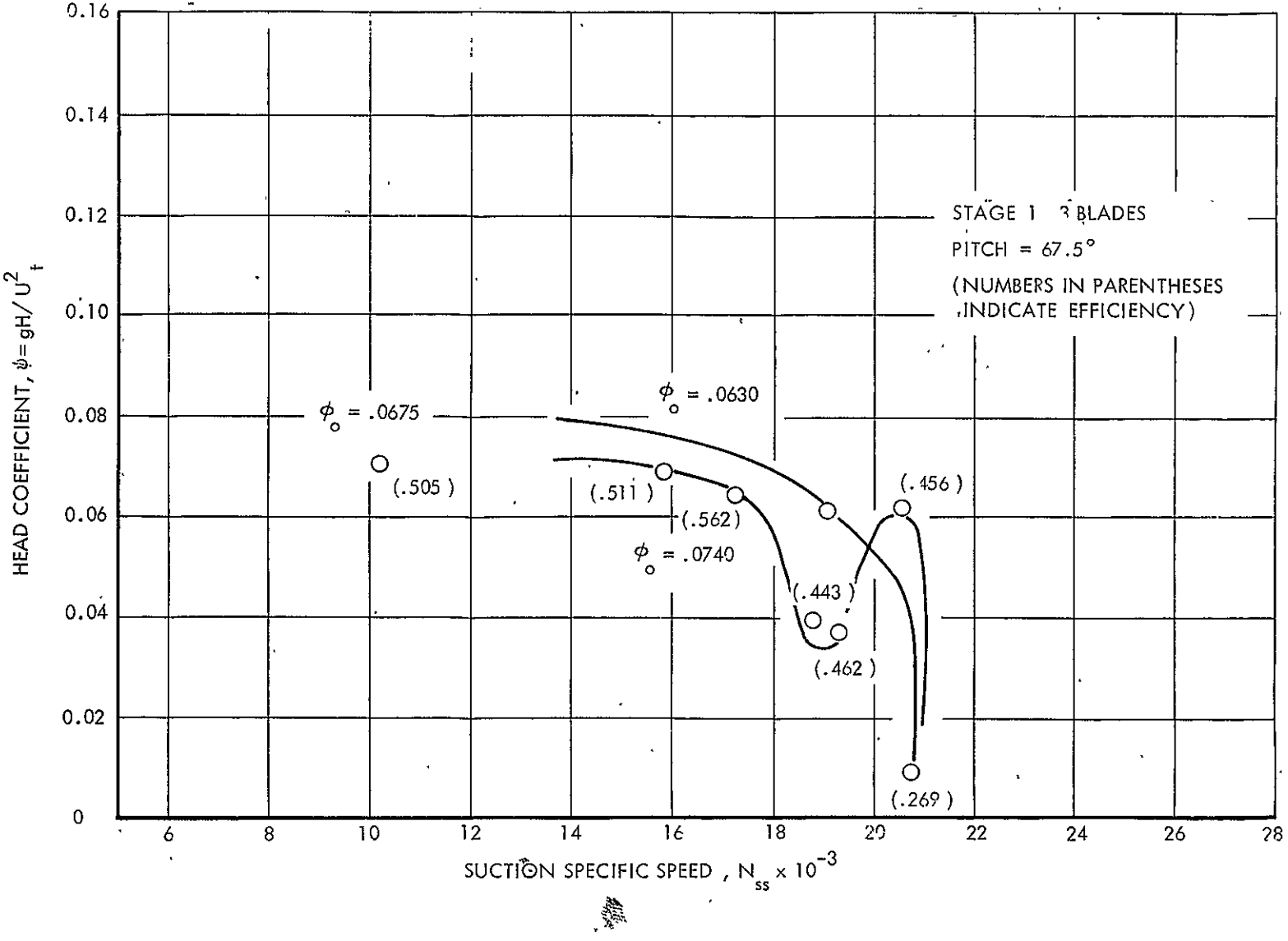

FIGURE 28 - INFLUENCE OF SUCTION SPECIFIC SPEED ON THE PERFORMANCE OF STAGE 1, INDUCER NO. 2 WITH 3 BLADES AT A PITCH OF 67.5

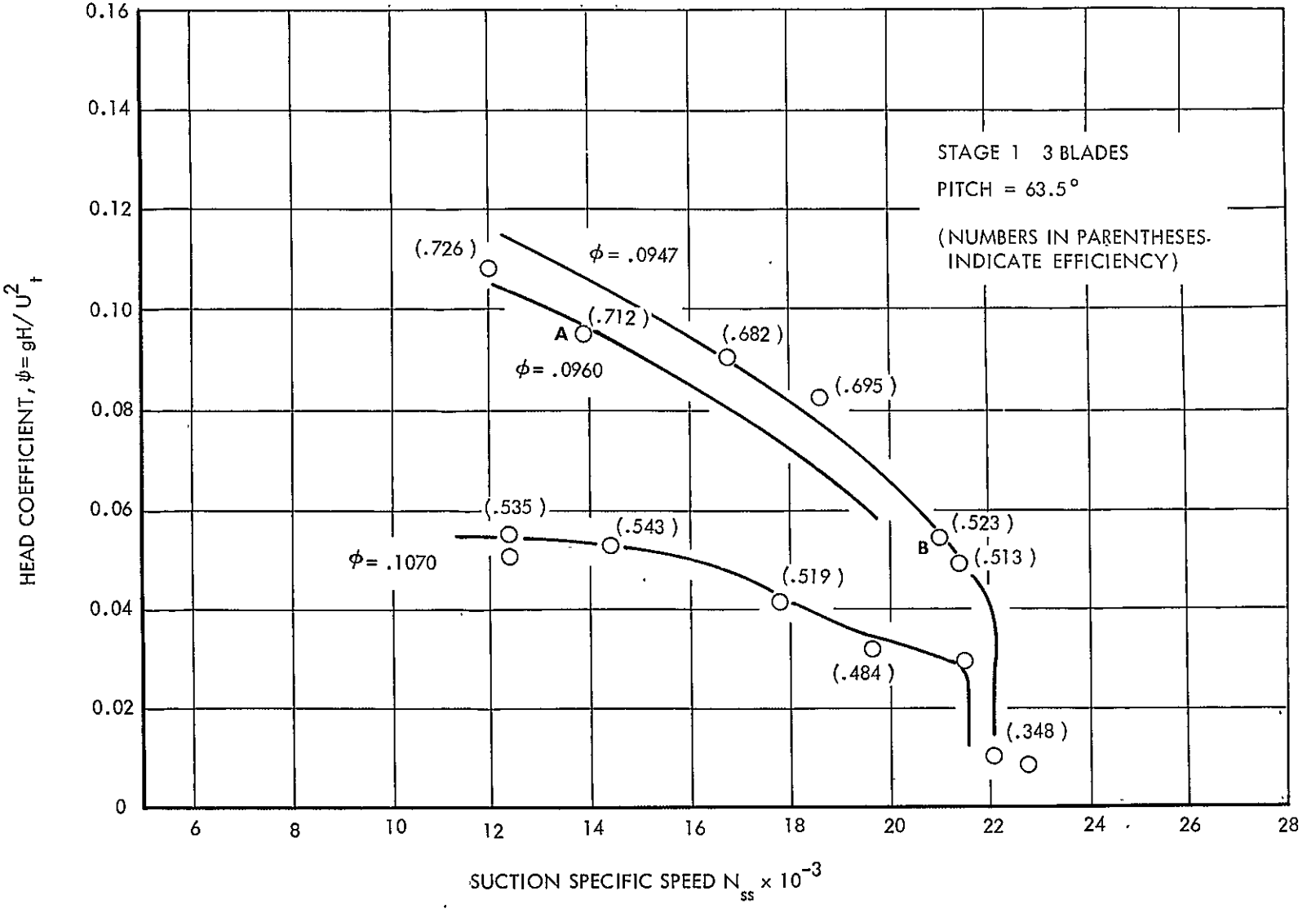

FIGURE 29 - INFLUENCE OF SUCTION SPECIFIC SPEED ON THE PERFORMANCE OF STAGE 1, INDUCER NO. 2 WITH 3 BLADES AT A PITCH OF 63.5°

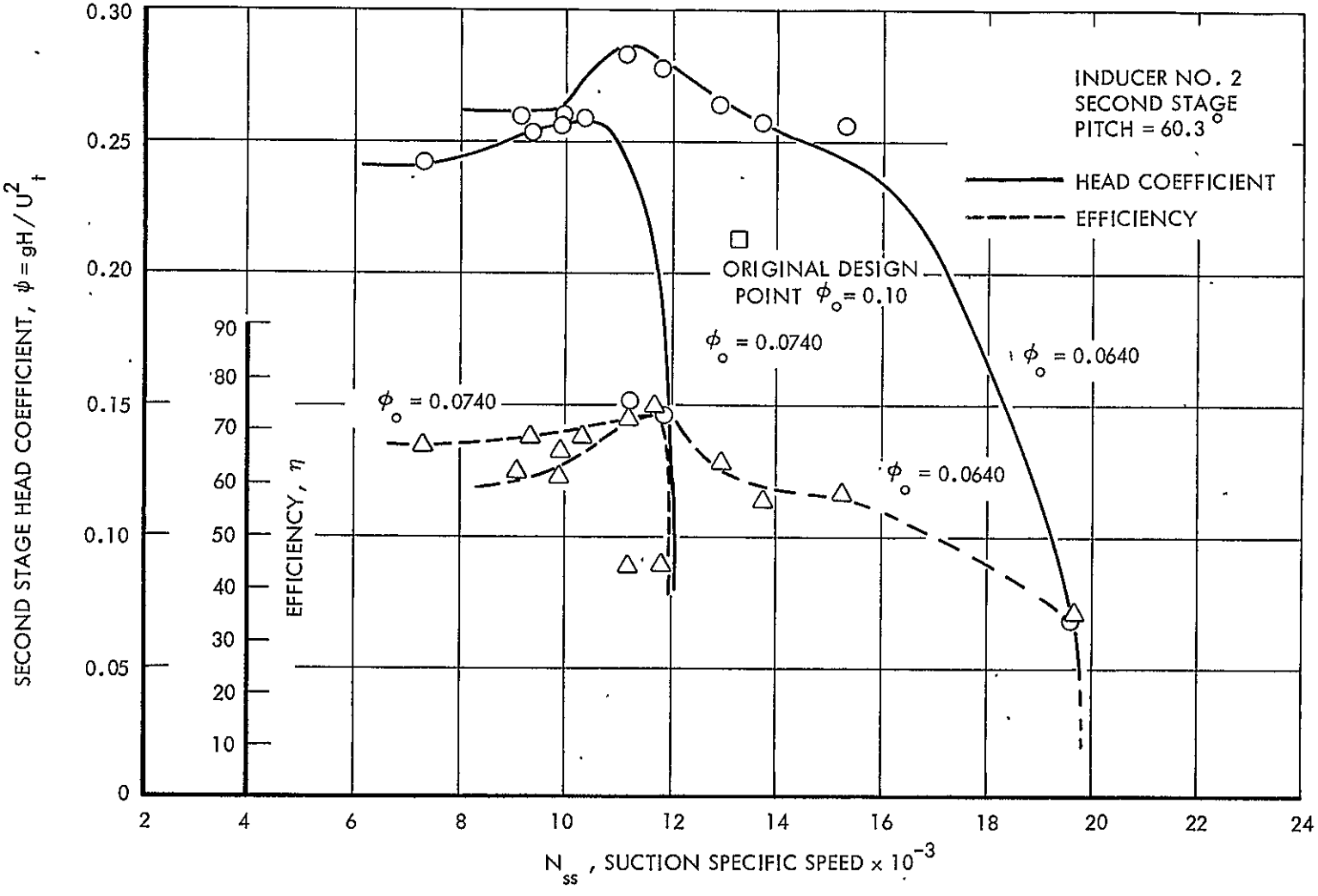

FIGURE 30 - INFLUENCE OF SUCTION SPECIFIC SPEED ON THE PERFORMANCE OF STAGE 2, INDUCER NO. 2 WITH 6 BLADES AT PITCH OF 60.3° (ORIGINAL DESIGN PITCH - 5.5°)

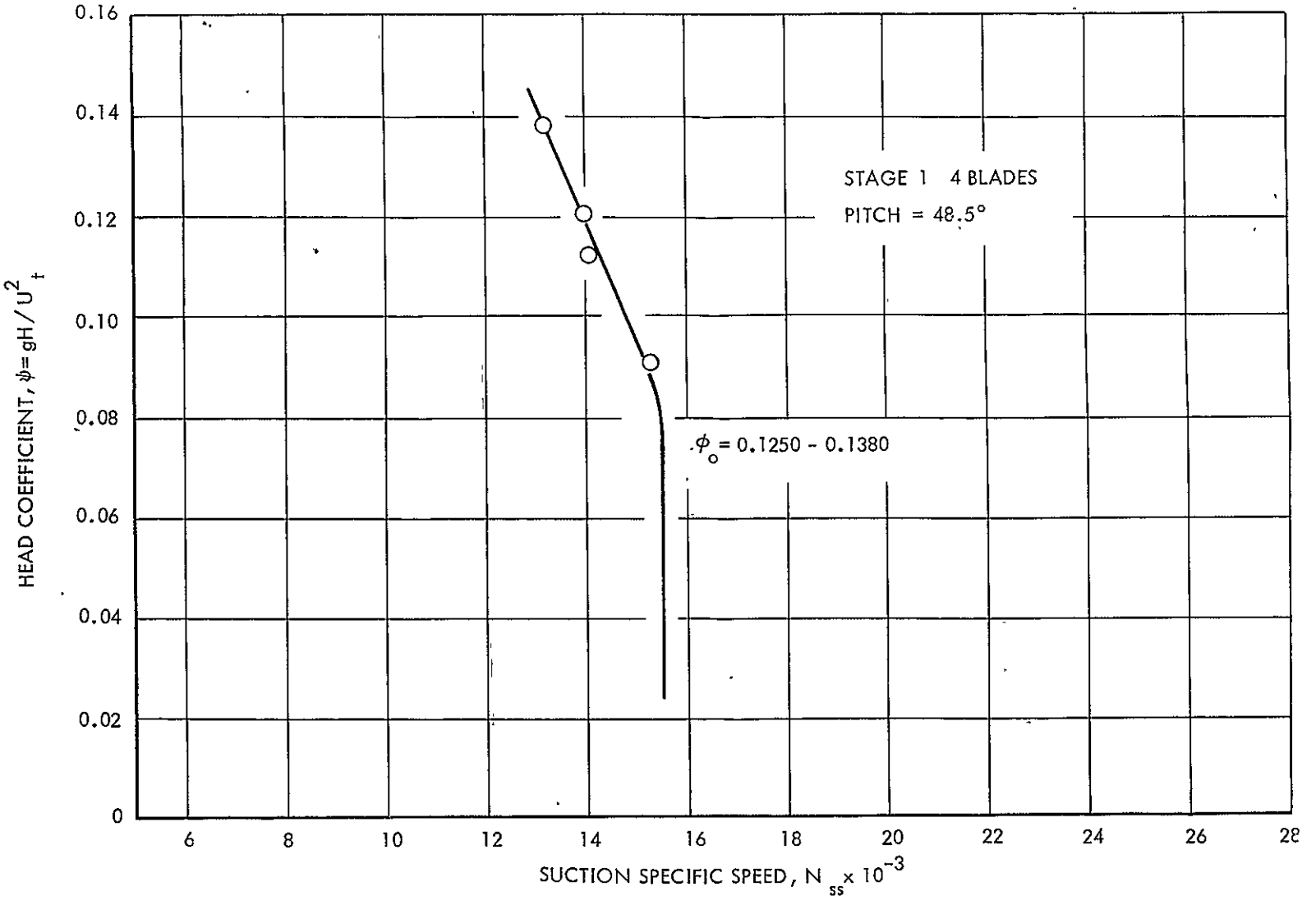

FIGURE 31 - INFLUENCE OF SUCTION SPECIFIC SPEED ON THE PERFORMANCE OF STAGE 1 , INDUCER NO. 3 WITH 4 BLADES AT A PITCH OF 48.5°

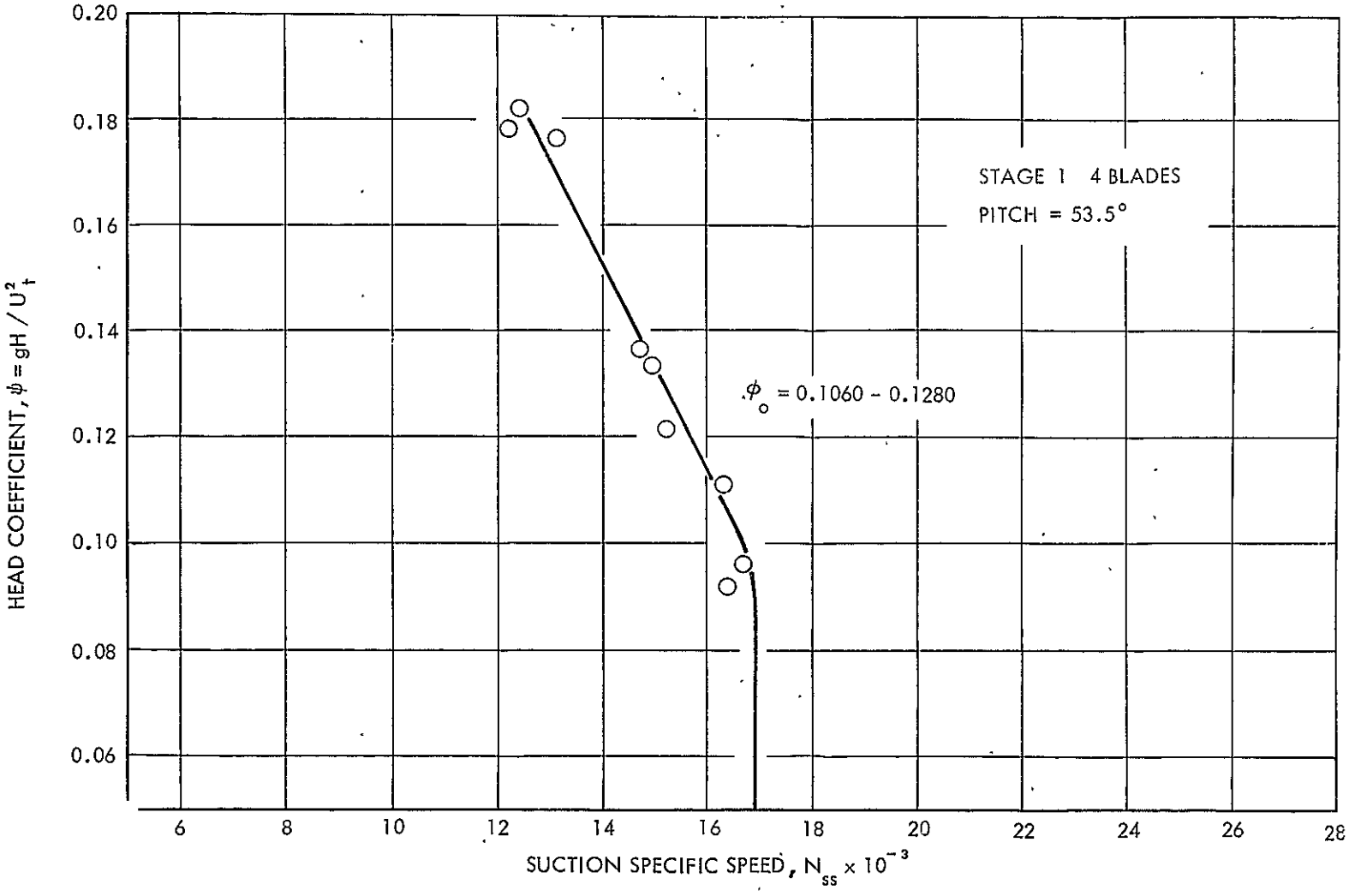

FIGURE 32 - INFLUENCE OF SUCTION SPECIFIC SPEED ON THE PERFORMANCE OF STAGE 1, INDUCER NO. 3 AT A PITCH OF 53.5°

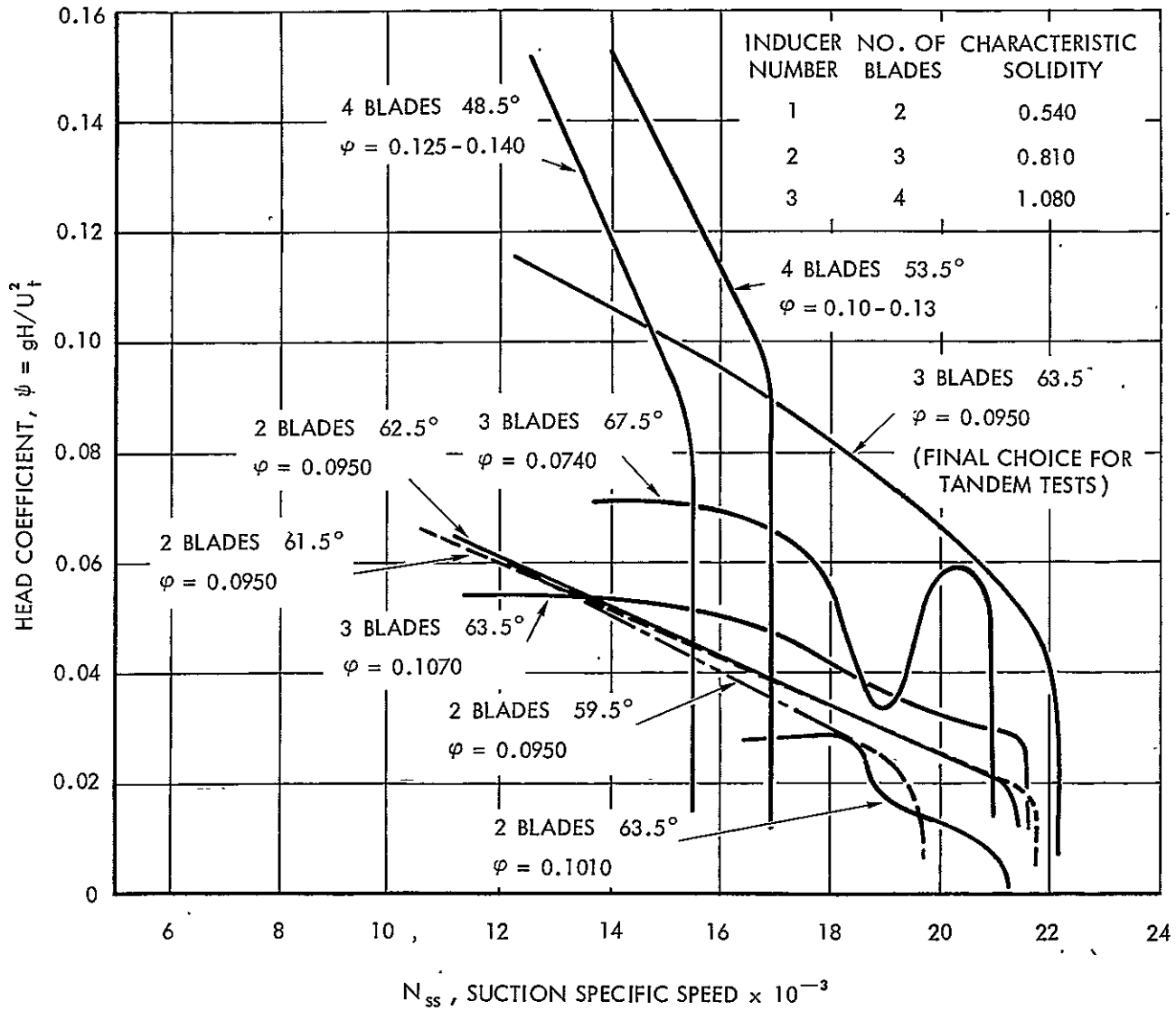

FIGURE 33 - SUMMARY OF PERFORMANCE OF SUPERCAVITATING FIRST STAGES FOR INDUCERS 1, 2, AND 3 AT NEAR DESIGN FLOW COEFFICIENT, $\varphi = 0$.

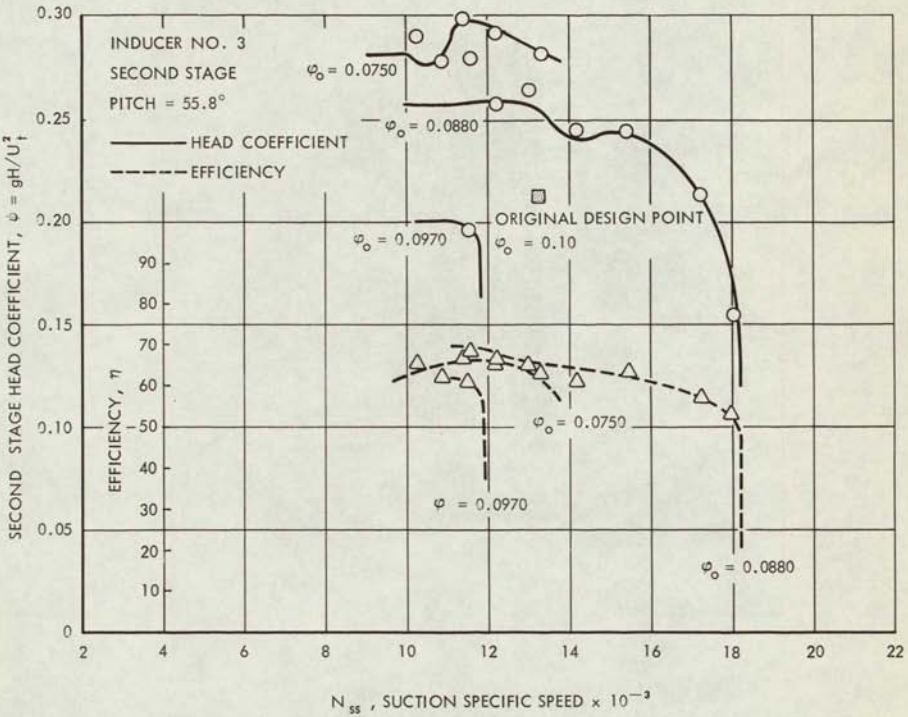

FIGURE 34 - INFLUENCE OF SUCTION SPECIFIC SPEED ON THE PERFORMANCE OF STAGE 2, INDUCER NO. 3 WITH 6 BLADES AT A PITCH OF 55.8° (ORIGINAL DESIGN PITCH - 10°)

FIGURE 35 - TANDEM INDUCER MODEL WITH −6 INCH OVERLAP AND 0° OFFSET. FIRST STAGE - 3 BLADES AT 63.5° PITCH, SECOND STAGE - 6 BLADES AT 55.8° PITCH.

FIGURE 37 - TANDEM INDUCER MODEL WITH −1.5 INCH OVERLAP AND 0° OFFSET. FIRST STAGE - 3 BLADES AT 63.5° PITCH, SECOND STAGE - 6 BLADES AT 55.8° PITCH.

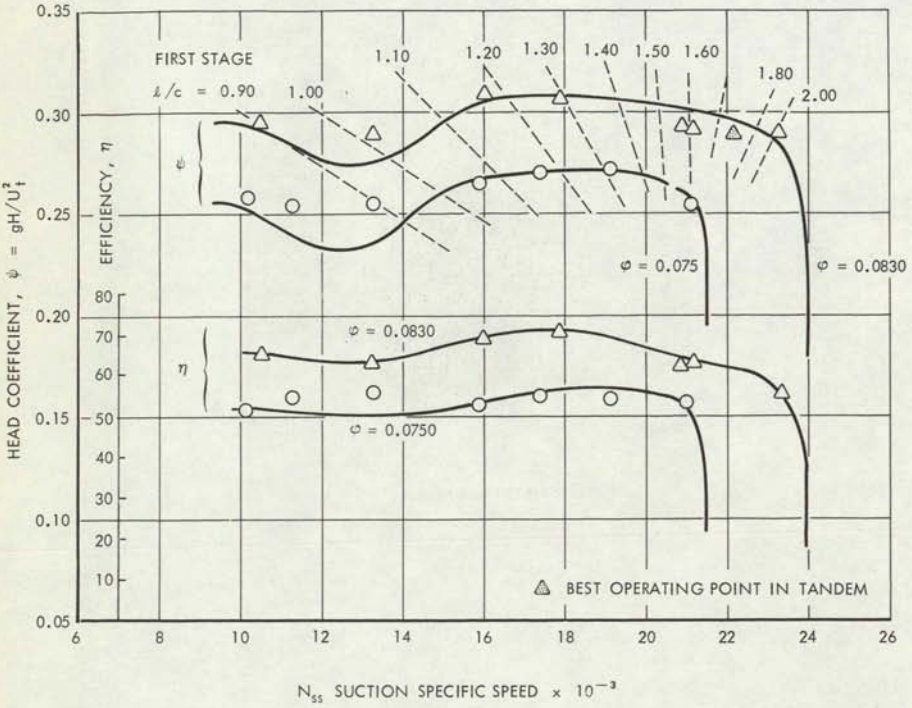

FIGURE 36 - TANDEM INDUCER PERFORMANCE WITH – 6" OVERLAP, STAGE 1 - THREE BLADES 63.5° PITCH; STAGE 2 - 6 BLADES, 55.8° PITCH

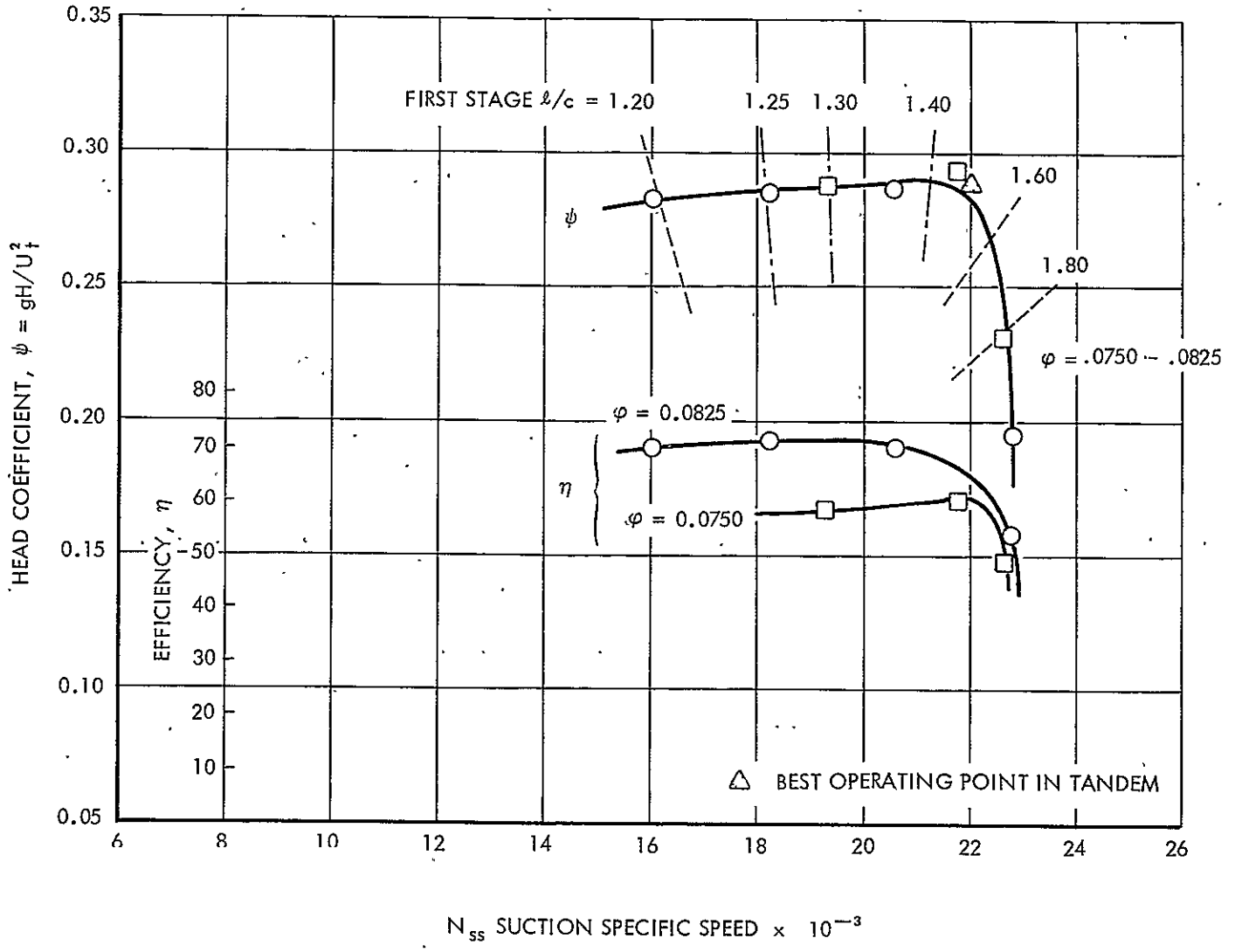

FIGURE 38 - TANDEM INDUCER PERFORMANCE WITH −1.5" OVERLAP STAGE 1 - THREE BLADES, 63.5° PITCH; STAGE 2 - SIX BLADES, 55.8° PITCH

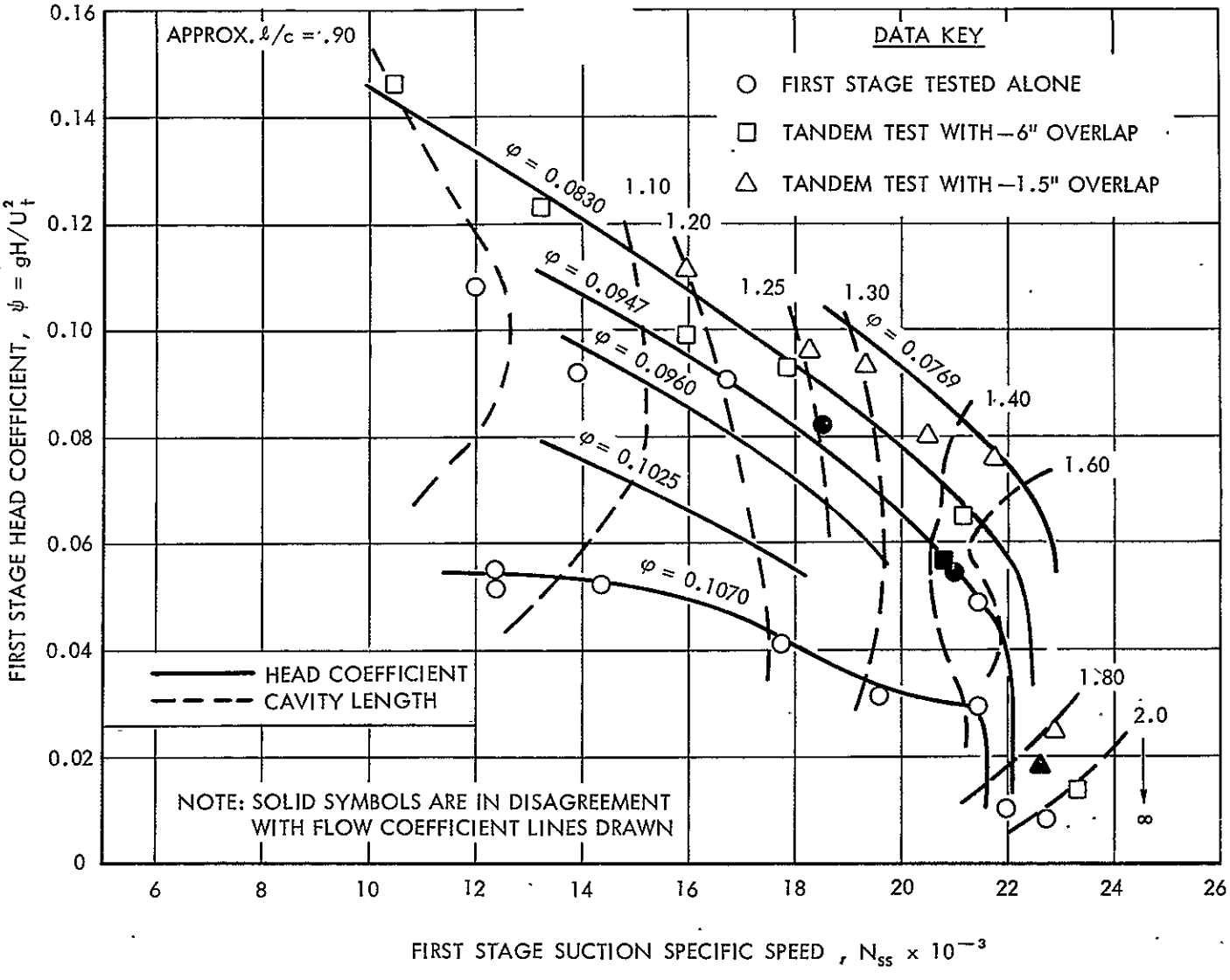

FIGURE 39 - SUMMARY OF PERFORMANCE OF STAGE 1 IN TANDEM AND ISOLATED WITH THREE BLADES AT 63.5° PITCH

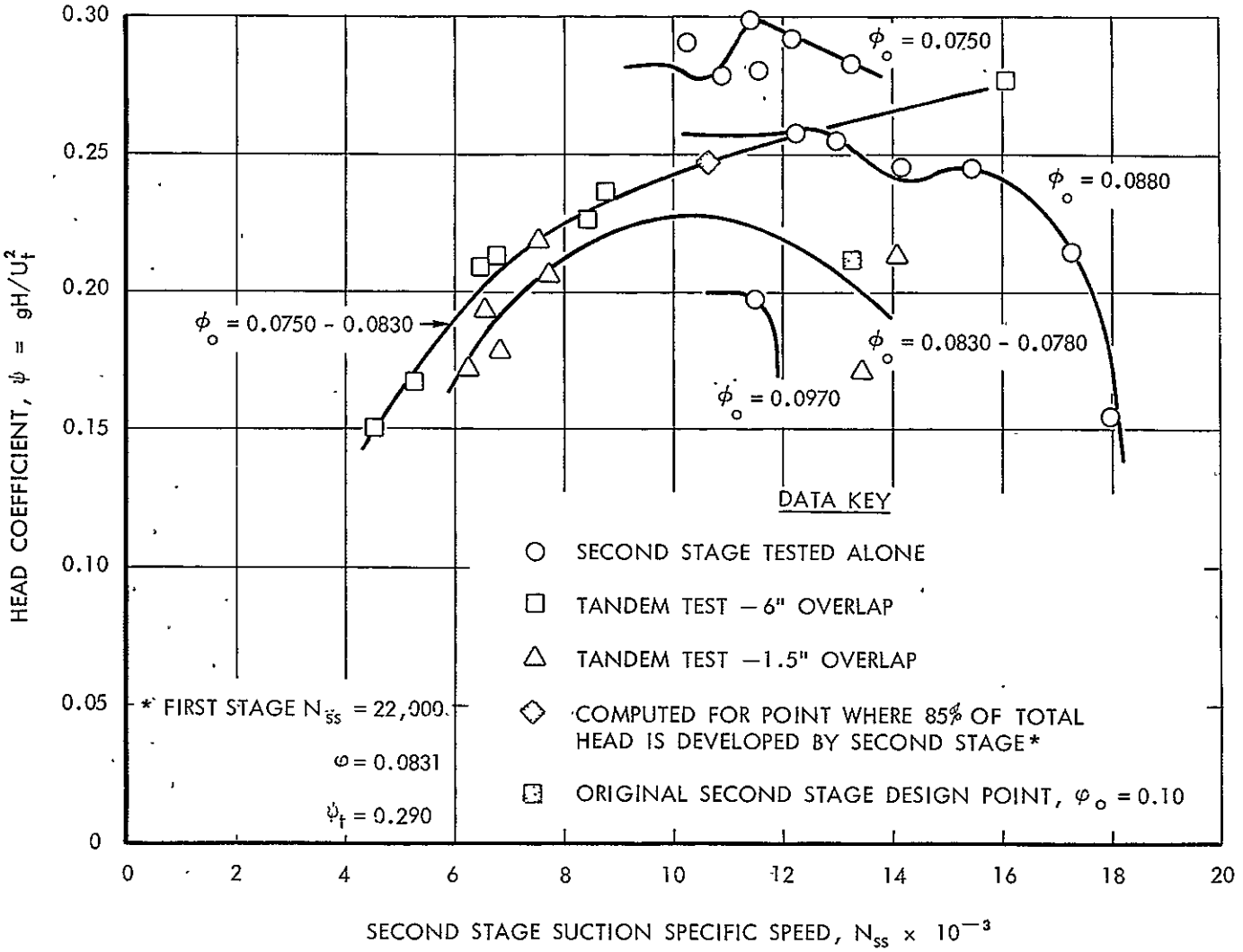

FIGURE 40 - SUMMARY OF PERFORMANCE OF STAGE 2 IN TANDEM AND ISOLATED WITH SIX BLADES AT 55.8° PITCH

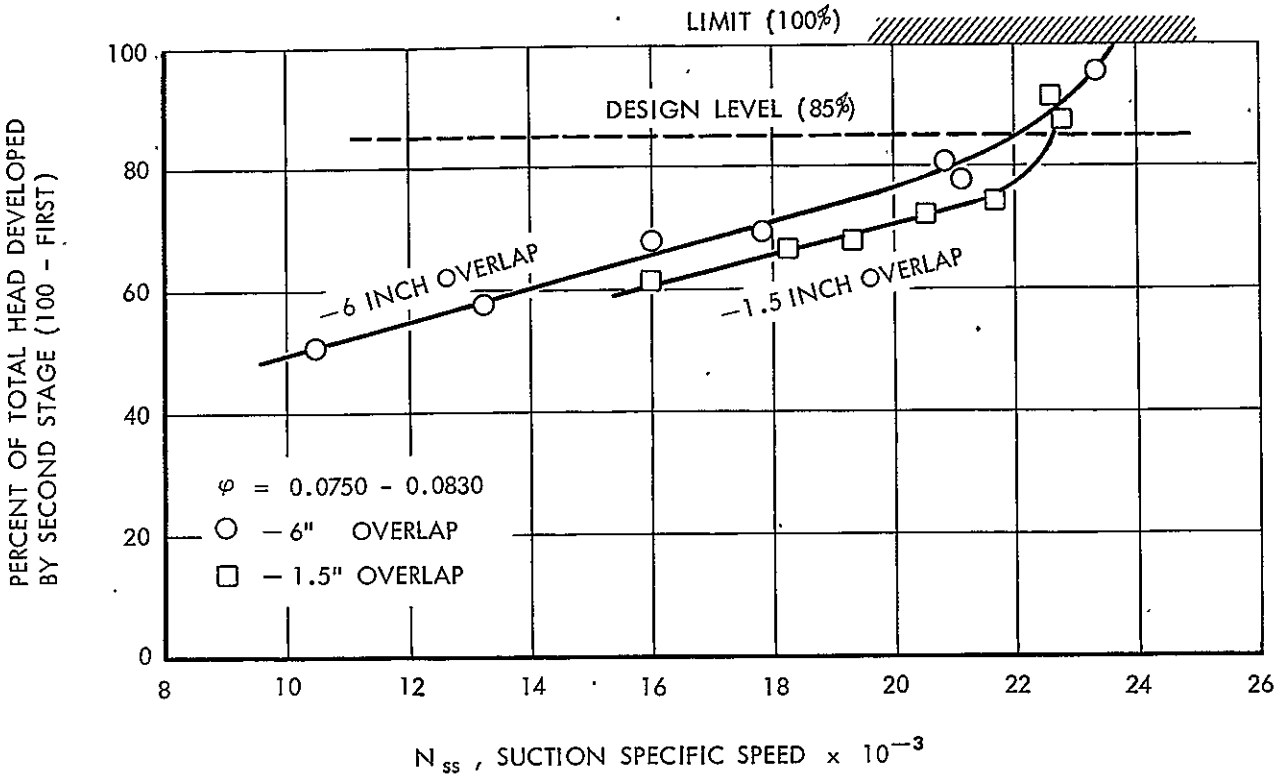

FIGURE 41 - DISTRIBUTION OF TOTAL HEAD RISE BETWEEN STAGE 1 AND STAGE 2 DURING TANDEM TESTS

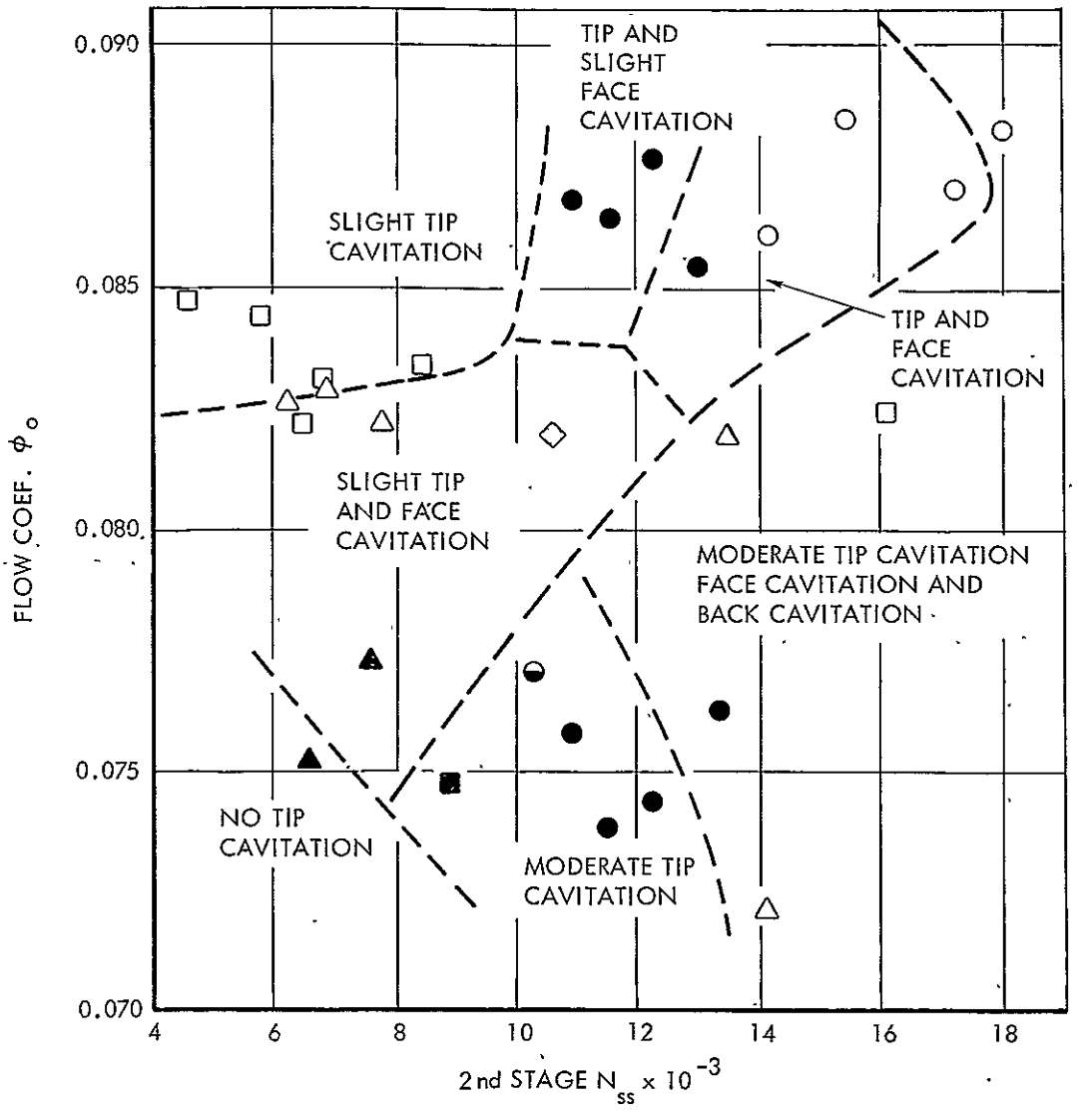

FIGURE 42 - SUMMARY OF SECOND STAGE CAVITATION PATTERNS DURING TANDEM TESTS AND ISOLATED - 6 BLADES AT 55.8° PITCH.

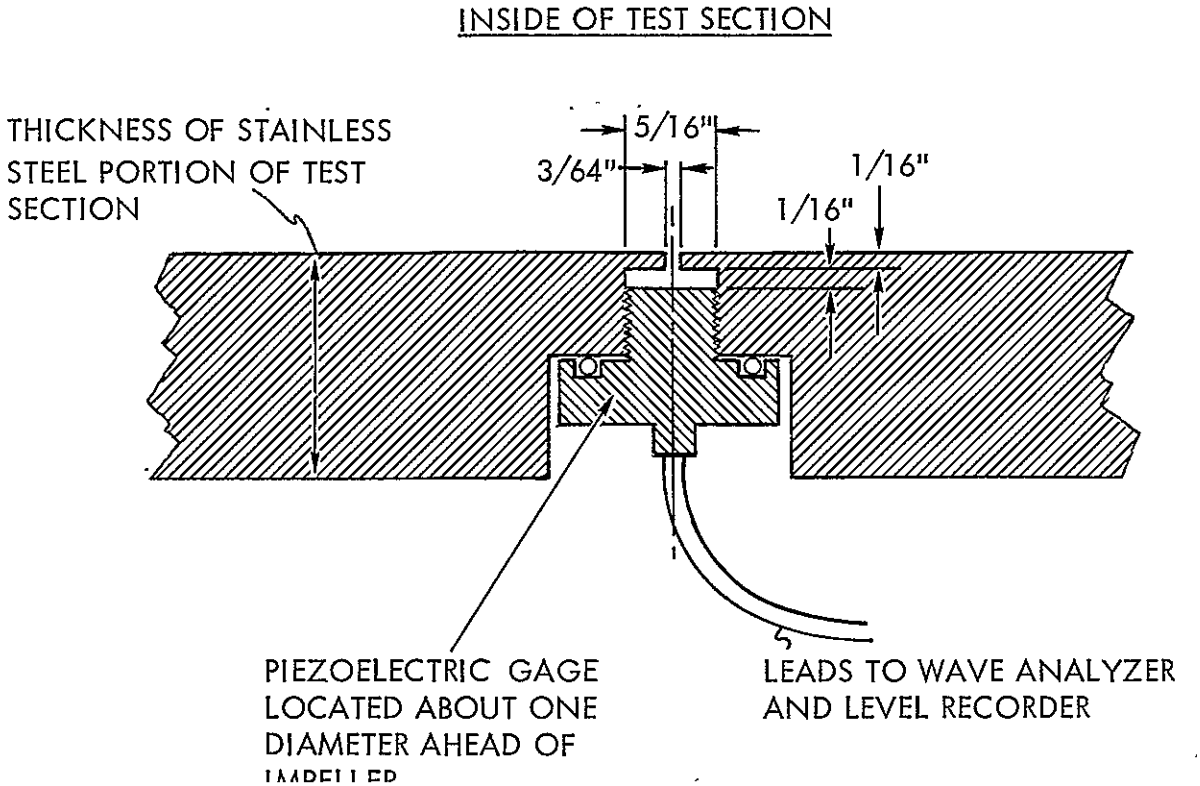

FIGURE 43 - SYSTEM TO MEASURE PRESSURE FLUCTUATIONS
(Natural frequency of system > 10K cps)